

Proximity effects in graphene on monolayers of transition-metal phosphorus trichalcogenides MPX_3

Klaus Zollner* and Jaroslav Fabian

Institute for Theoretical Physics, University of Regensburg, 93040 Regensburg, Germany

We investigate the electronic band structure of graphene on a series of two-dimensional magnetic transition-metal phosphorus trichalcogenide monolayers, MPX_3 with $M=\{\text{Mn,Fe,Ni,Co}\}$ and $X=\{\text{S,Se}\}$, with first-principles calculations. A symmetry-based model Hamiltonian is employed to extract orbital parameters and sublattice resolved proximity-induced exchange couplings ($\lambda_{\text{ex}}^{\text{A}}$ and $\lambda_{\text{ex}}^{\text{B}}$) from the low-energy Dirac bands of the proximitized graphene. Depending on the magnetic phase of the MPX_3 layer (ferromagnetic and three antiferromagnetic ones), completely different Dirac dispersions can be realized with exchange splittings ranging from 0 to 10 meV. Remarkably, not only the magnitude of the exchange couplings depends on the magnetic phase, but also the global sign and the type. Important, one can realize uniform ($\lambda_{\text{ex}}^{\text{A}} \approx \lambda_{\text{ex}}^{\text{B}}$) and staggered ($\lambda_{\text{ex}}^{\text{A}} \approx -\lambda_{\text{ex}}^{\text{B}}$) exchange couplings in graphene. From selected cases, we find that the interlayer distance, as well as a transverse electric field are efficient tuning knobs for the exchange splittings of the Dirac bands. More specifically, decreasing the interlayer distance by only about 10%, a giant 5-fold enhancement of proximity exchange is found, while applying few V/nm of electric field, provides tunability of proximity exchange by tens of percent. We have also studied the dependence on the Hubbard U parameter and find it to be weak. Moreover, we find that the effect of SOC on the proximitized Dirac dispersion is negligible compared to the exchange coupling.

Keywords: spintronics, graphene, heterostructures, proximity effect

I. INTRODUCTION

Monolayer magnets are key ingredients for novel spintronics applications, such as in tunneling magnetoresistance and spin-orbit torque device architectures [1–6]. One step towards next generation devices is to achieve highly spin polarized currents and long-distance transfer of spin information in all two dimensional (2D) van der Waals (vdW) heterostructures without the need of conventional ferromagnets (FM), where, for example, conductivity mismatch occurs at the interface [7–11]. Remarkably, recent experiments have shown that in graphene/CrSBr heterostructures, where CrSBr is a layered antiferromagnet, high spin polarization of the graphene conductivity arises solely due to proximity-induced exchange coupling [12, 13]. Therefore, it is essential to study proximity effects in graphene, since it already intrinsically provides long-distance spin communication [14, 15], but lacks an efficient spin manipulation knob.

Proximity effects in graphene can significantly alter the spin transport. For example, heterostructures with transition-metal dichalcogenides (TMDCs) provide a giant enhancement of the spin-orbit coupling (SOC) in graphene by proximity [16, 17]. Moreover, the proximity SOC can be efficiently tuned by gating and twisting in graphene/TMDC heterostructures [18–24], allowing to tailor, for example, the interconversion between spin and charge currents [23–37] or the spin-relaxation anisotropy [21, 38–43]. Placing graphene on a ferro- or antiferromagnet results in proximity-induced exchange coupling. Par-

ticularly interesting are magnetic semiconductors such as $\text{Cr}_2\text{Ge}_2\text{Te}_6$ [1, 44, 45] or CrI_3 [46–49], providing spin splitting for Dirac electrons but without contributing to transport. Moreover, the proximity-induced exchange coupling can also be tailored by gating and twisting [50, 51], important in, for example, the realization and engineering of topological states in graphene [46, 52, 53].

Unlike ferromagnets, antiferromagnetic monolayers have not yet been systematically investigated for proximity effects in graphene. Transition-metal phosphorus trichalcogenides (MPX_3) are particularly interesting: they are semiconducting, stable in air, and can offer different magnetic configurations [54–75]. In general, MPX_3 monolayers are formed by transition-metal atoms, $M=\{\text{Mn,Fe,Ni,Co}\}$, arranged in a honeycomb lattice and surrounded by octahedrally coordinated chalcogen atoms, $X=\{\text{S,Se}\}$. Each honeycomb hexagon additionally has two vertically-stacked P atoms at the center. Remarkably, the magnetic properties of the MPX_3 crystals can be tuned by gating and straining [61]. In addition, these materials exhibit giant exciton binding energies of several hundred meV [76, 77], even larger than in TMDCs, making them candidates for optospintronics applications. In Ni-based transition-metal phosphorus trichalcogenides, there is even evidence of topological superconductivity [64]. Heterostructures of MnPSe_3 and MoS_2 show a type-II band alignment, important for optics, and a stacking dependent lifting of spin and valley degeneracy in MnPSe_3 [78], potentially interesting for valleytronics applications [79, 80]. Moreover, it has been shown that antiferromagnetic FePS_3 increases the coercive field and Curie temperature of the 2D itinerant ferromagnet Fe_3GeTe_2 [81], while NiPS_3 can be important to tailor interfacial spin-orbit torques [82].

* klaus.zollner@physik.uni-regensburg.de

Graphene on MPX_3 monolayers is expected to exhibit strong proximity exchange, depending on the magnetic configuration, stacking, twisting, and gating. For example, MnPSe_3 is an Ising-type antiferromagnetic semiconductor (out-of-plane and alternating magnetic moments on Mn atoms), with the potential to induce staggered exchange coupling in graphene, as recently demonstrated [52]. In this study, we consider monolayer graphene in proximity to various MPX_3 monolayers, which can be either in the ferromagnetic, antiferromagnetic Néel, antiferromagnetic zigzag, or antiferromagnetic stripy phase. In order to unveil the proximity-induced exchange coupling in graphene, we calculate the low-energy Dirac dispersions of the heterostructures by density functional theory (DFT), and fit them to a symmetry-based model Hamiltonian. The effective model can be used for investigating spin transport, spin dynamics, and topologies of proximitized Dirac electrons in graphene/ MPX_3 structures. Such effective models are transferable due to the short-range character of the proximity effect: if a graphene/ MPX_3 interface is part of a vdW heterostructure, the model Hamiltonian we introduce can be applied directly to it.

Depending on the transition metal $M=\{\text{Mn,Fe,Ni,Co}\}$, the chalcogen atom $X=\{\text{S,Se}\}$, and the magnetic phase, the proximity-induced exchange coupling in graphene can be markedly different. In particular, we find proximity exchange couplings that range from about 0 to 10 meV, varying in sign and type. Most important, one can realize uniform (ferromagnetic) and staggered (antiferromagnetic) proximity exchange in graphene. From the selected case of graphene/ MnPS_3 in the antiferromagnetic Néel phase (ground state), we find that the interlayer distance, as well as a transverse electric field are efficient tuning knobs for the exchange splittings of the Dirac bands. More specifically, decreasing the interlayer distance by only about 10%, a giant 5-fold enhancement of proximity exchange is found, while applying just a few V/nm of electric field can tune proximity exchange by tens of percent. We have also studied the dependence on the Hubbard U parameter and find it to be weak. Moreover, we find that the effect of SOC on the proximitized Dirac dispersion is negligible compared to the exchange coupling. Our findings should be useful for spin transport, spin relaxation, optospintronics applications, as well as for tailoring topological phases of the Dirac electrons in graphene [52, 76, 78].

The paper is organized as follows. In Sec. II, we first discuss our computational methodology and the geometry setup. In Sec. III, we then introduce the symmetry-based model Hamiltonian capturing the proximity-induced exchange coupling in graphene. In Sec. IV, we show and discuss the electronic structure and fit results of the different magnetic phases on the example of the graphene/ MnPS_3 heterostructure. In addition, we report on the effect of the interlayer distance, a transverse electric field, the Hubbard U , and SOC on the proximitized Dirac dispersion. Finally, in Sec. V we

summarize and conclude the paper.

II. COMPUTATIONAL DETAILS AND GEOMETRY

The electronic structure calculations and structural relaxation of graphene on monolayers of the layered magnets MPX_3 are performed by density functional theory (DFT) [83] with `Quantum ESPRESSO` [84]. Self-consistent calculations are carried out with the k -point sampling of $24 \times 24 \times 1$ to get converged results for the proximity exchange splittings. We perform open shell calculations that provide the spin-polarized (magnetic) states of the MPX_3 monolayers. A Hubbard parameter of $U = 4.5$ eV is used for $M=\{\text{Mn,Fe,Co,Ni}\}$ d -orbitals, as in recent calculations [78, 85]. We use an energy cutoff for charge density of 700 Ry and the kinetic energy cutoff for wavefunctions is 70 Ry for the scalar relativistic pseudopotential with the projector augmented wave method [86] with the Perdew-Burke-Ernzerhof exchange correlation functional [87]. When SOC is included, we use the relativistic version of the pseudopotentials. For the relaxation of the heterostructures, we add van der Waals corrections [88–90] and use quasi-Newton algorithm based on trust radius procedure. In order to simulate quasi-2D systems, we add a vacuum of 20 Å to avoid interactions between periodic images in our slab geometry. To determine the interlayer distances, the atoms of graphene are allowed to relax only along z -direction (vertical to the layers) and the atoms of MPX_3 are allowed to move in all directions, until every component of each force is reduced below 10^{-4} [Ry/ a_0], where a_0 is the Bohr radius.

For some of our heterostructures, we cross-check the results with the `WIEN2k` DFT-code [91], using the relaxed structures obtained with `Quantum ESPRESSO`. We use a k -point sampling of $18 \times 18 \times 1$ with the cutoff parameter $RK_{\text{max}} = 4.6$. The muffin-tin radii are $R_M = 2.5$, $R_P = 1.87$ (1.86), $R_X = 1.96$ (2.27), and $R_C = 1.32$ (1.34) for $X = \text{S}$ (Se). Van der Waals corrections and a Hubbard $U = 4.5$ eV are also included [89, 92].

The heterostructures of graphene/ MPX_3 contain a 5×5 supercell of graphene on a 2×2 MPX_3 supercell, resulting in 90 atoms in the unit cell. We consider cases for $M = \{\text{Mn,Fe,Ni,Co}\}$ and $X = \{\text{S,Se}\}$. In Fig. 1(a,b) we show the exact geometry of the heterostructures. The M atoms of the MPX_3 monolayers form a hexagonal lattice. Depending on the M atom, the MPX_3 monolayer can have a different magnetic ground state. We consider all of our MPX_3 substrates to be either in the ferromagnetic, antiferromagnetic Néel, antiferromagnetic zigzag, or antiferromagnetic stripy phase, as shown in Fig. 1(c)-(f), but with magnetizations to be collinear with the z -direction. Note, that structural relaxation was performed only for the ferromagnetic phase. The relaxed geometries are then employed for all other magnetic phases as well. We find that the forces in the other magnetic phases are below 10^{-3} [Ry/ a_0], justifying this approach. In addition, we

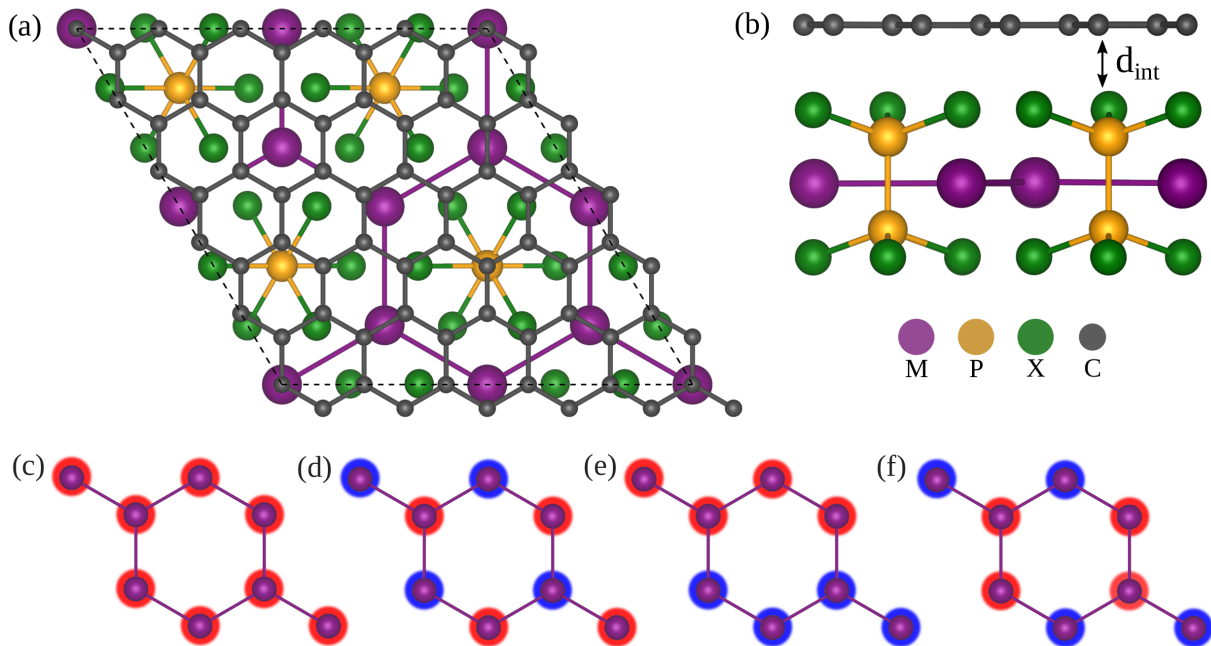


FIG. 1. (a,b) Top and side view of the graphene/MPX₃ heterostructure. Dashed line in (a) defines the heterostructure unit cell and in (b) we define the interlayer distance d_{int} . Different colors correspond to different atom types. Depending on the MPX₃ crystal, the hexagonal M-lattice can show the (c) ferromagnetic, (d) antiferromagnetic Néel, (e) antiferromagnetic zigzag, and (f) antiferromagnetic stripy phase. Red (blue) spheres indicate magnetization of the M atom along z ($-z$) direction.

TABLE I. Investigated crystallographic and magnetic information collected from Refs. [54, 56, 58–66, 93–105], for the considered monolayers used in the graphene/MPX₃ heterostructures. The experimental (exp.) and the employed heterostructure (het.) lattice constants a . The strain for each subsystem, is calculated as $(a_{\text{het}} - a_{\text{exp}})/a_{\text{exp}}$. We also list the Néel temperature T_{N} , the experimentally determined magnetic ground state for each MPX₃, as shown in Figs. 1(c)-(e), and the DFT-relaxed interlayer distance d_{int} between graphene and the MPX₃.

	graphene	MnPSe ₃	MnPS ₃	FePSe ₃	FePS ₃	NiPSe ₃	NiPS ₃	CoPSe ₃	CoPS ₃
a (exp.) [Å]	2.46	6.39	6.08	6.26	5.94	6.13	5.82	6.19	5.90
a (het.) [Å]	2.48 (2.44) ^a	6.20	6.10	6.20	6.10	6.20	6.10	6.20	6.10
strain [%]	0.8 (-0.8)	-2.9	0.3	-1.0	2.7	1.1	4.8	0.2	3.4
T_{N} [K]	-	74	78	119	120	206	154	-	120
ground state	-	Néel	Néel	Zigzag	Zigzag	Zigzag	Zigzag	-	Zigzag
d_{int} [Å]	-	3.457	3.422	3.471	3.448	3.474	3.440	3.488	3.430

^a For graphene/MPSe₃ (graphene/MP₃) structures we stretch (compress) the graphene lattice constant to 2.48 Å (2.44 Å).

consider only geometries with 0° relative twist angle and the stacking as shown in Fig. 1(a)

In Table I we summarize the experimental lattice constants of all considered monolayers, as well as their strained lattice constants used for the heterostructure calculations. We also list the Néel temperature T_{N} , the experimentally determined magnetic ground state for each MPX₃, and the DFT-relaxed interlayer distance d_{int} between graphene and the MPX₃. For example, MnPSe₃ is a semiconductor, with an optical gap of about 2.3 eV [68, 106]. According to experiments, the lattice constant is $a = 6.39$ Å, it has a Néel temperature of $T_{\text{N}} = 74$ K, and the magnetic ground state is the antiferromagnetic Néel one [54], see Fig. 1(d). Due to lattice mismatch with

graphene, we strain the MnPSe₃ layer by about -2.9% to get the mentioned supercell with commensurate lattices. The relaxed interlayer distance with graphene is $d_{\text{int}} = 3.457$ Å.

III. LOW ENERGY MODEL HAMILTONIAN

From our first-principles calculations we obtain the low energy Dirac band structure of the proximitized graphene and extract realistic parameters for an effective Hamiltonian describing the low-energy bands. The goal is to find an effective description for the low-energy physics, which

is relevant for studying transport [23, 24, 26, 45, 107], topology [52, 108], spin relaxation [38, 43, 109, 110], or emergent long-range order [111]. Due to the short-range nature of the proximity effects in van der Waals heterostructures, the effective models are transferable [112–114]. For example, a bilayer-graphene encapsulated from two sides by different materials, can be described by combining the effective models for two proximitized graphene sheets, coupled by bilayer-graphene interlayer couplings [112, 113].

The systems we consider have broken time-reversal symmetry and either C_3 or no symmetry, depending on the magnetic phase of the underlying MPX_3 . The following Hamiltonian, derived from symmetry [115–117], is able to describe the graphene bands in the vicinity of the Dirac points when proximity exchange is present

$$\mathcal{H} = \mathcal{H}_0 + \mathcal{H}_\Delta + \mathcal{H}_{\text{ex}} + E_D, \quad (1)$$

$$\mathcal{H}_0 = - \sum_s f_s(\mathbf{q}) |\Psi_A, s\rangle \langle \Psi_B, s| + h.c. \quad (2)$$

$$\mathcal{H}_\Delta = \Delta \sigma_z \otimes s_0, \quad (3)$$

$$\mathcal{H}_{\text{ex}} = (-\lambda_{\text{ex}}^A \sigma_+ + \lambda_{\text{ex}}^B \sigma_-) \otimes s_z. \quad (4)$$

The orbital structural function we use is $f_s(\mathbf{q}) = t_{1,s} + t_{2,s} e^{i\mathbf{q}\mathbf{R}_2} + t_{3,s} e^{-i\mathbf{q}\mathbf{R}_3}$, where we denote $t_{\alpha,s}$ as the spin ($s = \{\uparrow, \downarrow\}$) and direction ($\alpha = \{1, 2, 3\}$) dependent hopping parameters, along direction $\mathbf{R}_\alpha = a(\cos \frac{2\pi(\alpha-1)}{3}, \sin \frac{2\pi(\alpha-1)}{3})$. The wavevector is $\mathbf{q} = \tau \mathbf{K} + \mathbf{k}$, for the valley index $\tau = \pm 1$ and $\tau \mathbf{K} = \pm(\frac{4\pi}{3a}, 0)$ with the lattice constant a .

This orbital structural function is a generalized case for the orbital Hamiltonian as defined in Ref. [115]. Typically, the standard linearized orbital Hamiltonian is used [110, 115], but with our definition, we can describe cases where the nearest-neighbor hoppings are spin dependent and can be different along different spatial directions. This is necessary, because the magnetic phase of the MPX_3 monolayer substrate determines the symmetry of the system and the dependence of hoppings on spatial directions. Additionally, because the substrate is magnetic, hoppings can be spin dependent.

The Pauli spin matrices are s_j , acting on spin space (\uparrow, \downarrow), and pseudospin matrices are σ_j , acting on sublattice space (C_A, C_B), with $j = \{0, x, y, z\}$ where $j = 0$ denotes the 2×2 unit matrix. For shorter notation, we use $\sigma_\pm = \frac{1}{2}(\sigma_z \pm \sigma_0)$. The staggered potential gap is Δ and the parameters, λ_{ex}^A and λ_{ex}^B , represent the sublattice-resolved proximity-induced exchange couplings. The four basis states are $|\Psi_A, \uparrow\rangle$, $|\Psi_A, \downarrow\rangle$, $|\Psi_B, \uparrow\rangle$, and $|\Psi_B, \downarrow\rangle$. The model Hamiltonian is centered around the Fermi level at zero energy. Since first-principles results capture charge-transfer effects, we also introduce the parameter E_D (termed Dirac point energy) which shifts the Dirac bands.

For each considered heterostructure, we calculate the proximitized low energy Dirac bands in the vicinity of the K point. To extract the fit parameters from the first-principles data, we employ a least-squares routine [118],

taking into account band energies, splittings, and spin expectation values (spin up and spin down).

IV. BAND STRUCTURE AND FIT RESULTS

In the following, we first neglect SOC in the calculations, since we are mainly interested in the proximity-induced exchange couplings. The effects of SOC are discussed at a later point. For our analysis of proximity effects, we consider graphene on the magnetic monolayers MPX_3 , for different magnetic phases, as shown in Fig. 1(c)-(f). Depending on the magnetic phase of the MPX_3 , the system shows either 3-fold symmetry for ferromagnetic and antiferromagnetic Néel phases or lacks all symmetries in the antiferromagnetic zigzag and stripy phases. In the following, we explicitly show and discuss the band structure and model calculations (with fitted parameters) for graphene on MnPS_3 as an exemplary case. In the Supplemental Material we show the band structure and the fitted results for the remaining MPX_3 substrates [119]. Furthermore, for graphene on MnPS_3 in the antiferromagnetic Néel phase (the ground state), we discuss the influence of the interlayer distance, the Hubbard U , and a transverse electric field on the fitted parameters.

A. Ferromagnetic phase

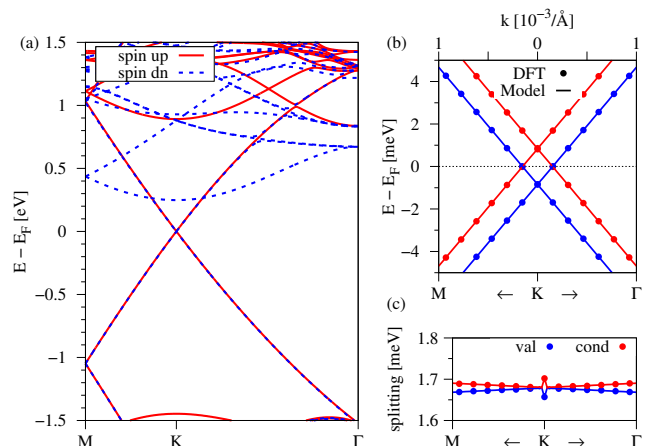


FIG. 2. (a) DFT-calculated band structure of the graphene/ MnPS_3 heterostructure along the high-symmetry path M-K- Γ without SOC, when the MnPS_3 is in the ferromagnetic phase. Red solid (blue dashed) lines correspond to spin up (spin down). (b) Zoom to the DFT-calculated (symbols) low energy Dirac bands near the K point with a fit to the model Hamiltonian (solid line). (c) The splitting of valence and conduction band.

First, we consider the MnPS_3 monolayer to be in the ferromagnetic phase in which the heterostructure has a

3-fold symmetry and our model can be further simplified by setting $t_{1,s} = t_{2,s} = t_{3,s}$ for both spin species s , respectively. In Fig. 2(a) we show the corresponding DFT-calculated band structure of the graphene/MnPS₃ without SOC. We find that the graphene Dirac states are located at the Fermi level and are well preserved. The parabolic spin down band above the Dirac cone originates from the magnetic substrate. In Fig. 2(b), we show a zoom to the low energy Dirac bands near the K point. We find that the model perfectly agrees with the DFT-calculated dispersion by using the parameters summarized in Table II. In this ferromagnetic case, uniform exchange parameters, $\lambda_{\text{ex}}^{\text{A}} \approx \lambda_{\text{ex}}^{\text{B}} \approx -0.8$ meV, are found. The calculated positive and uniform spin polarization on graphene is consistent with this picture, see Supplemental Material [119]. The staggered potential Δ is small (≈ 10 μeV), indicating that nearly no sublattice symmetry breaking is present. The orbital hopping parameters t_s are only slightly different for the two spin species. Using these parameters, not only the dispersion but also the band splittings, of about 1.7 meV, can be perfectly reproduced, see Fig. 2(c).

B. Antiferromagnetic Néel phase

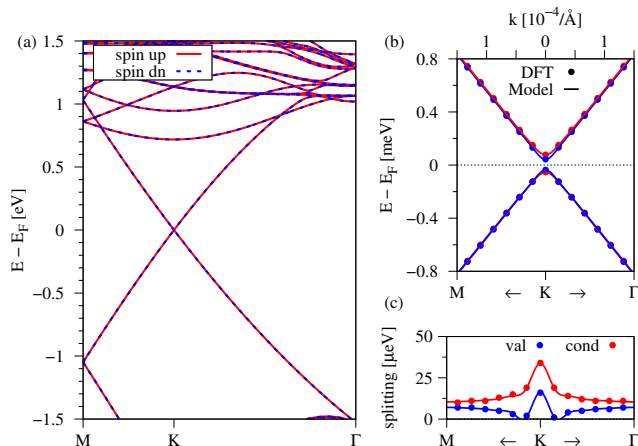


FIG. 3. Same as Fig. 2, but for the MnPS₃ in the antiferromagnetic Néel phase.

Second, we consider the MnPS₃ monolayer to be in the antiferromagnetic Néel phase, which is the ground state for this material. As before, we calculate the dispersion and employ our model Hamiltonian. Again, the heterostructure has a 3-fold symmetry in the antiferromagnetic Néel phase and we can use $t_{1,s} = t_{2,s} = t_{3,s}$ for the fitting procedure. The calculation and fitting results are summarized in Fig. 3. The Dirac bands of graphene are again well preserved and located at the Fermi level. Also the model agrees perfectly with the DFT-calculated dispersion and band splittings, employing the parameters from Table II. Compared to the ferromagnetic phase, band splittings are drastically dimin-

ished in magnitude from about 1.7 meV to 20 μeV . We can understand this by the following argument. In the antiferromagnetic Néel phase, the average proximity exchange on the graphene sublattices is reduced, because Mn atoms have alternating magnetizations. Therefore, the exchange field felt by graphene is strongly diminished. In contrast in the ferromagnetic phase, all Mn atoms have the same magnetization and proximity effects are much stronger. In addition, for the ferromagnetic phase, sublattice resolved proximity exchange parameters had the same sign, while for the antiferromagnetic Néel phase, we find opposite sign, $\lambda_{\text{ex}}^{\text{A}} < 0$ and $\lambda_{\text{ex}}^{\text{B}} > 0$. The calculated spin polarization, being opposite on the graphene sublattices, supports this result of staggered exchange couplings [119]. This is a very important finding, since the magnetic phase decides not only about the magnitude, but also the type of proximity exchange coupling, which can have dramatic consequences for topological phases in proximitized graphene [52].

C. Antiferromagnetic Zigzag phase

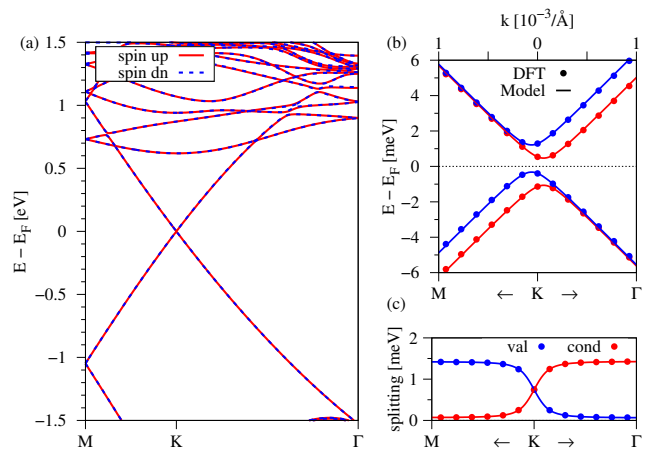


FIG. 4. Same as Fig. 2, but for the MnPS₃ in the antiferromagnetic zigzag phase.

Third, we consider the MnPS₃ monolayer to be in the antiferromagnetic zigzag phase. Now, the heterostructure has no symmetry and nearest-neighbor hopping amplitudes are becoming inequivalent $t_{1,s} \neq t_{2,s} \neq t_{3,s}$. This asymmetry in the hopping amplitudes leads to the shift of the Dirac point in momentum space [120, 121]. Because the system is additionally magnetic, spin up and spin down Dirac points do not need to be shifted equally away from the K point. In the Supplemental Material [119], we explicitly show a 2D-map of the low energy Dirac bands in momentum space, corresponding to Fig. 4(b). Especially in this case we take into account DFT-calculated bands not along a high-symmetry path, but in a small k -space region around the K point, to obtain accurate fitting results. In Fig. 4, we summarize our calculation and fit results for the graphene/MnPS₃

heterostructure when the MnPS_3 is in the antiferromagnetic zigzag phase. The global band structure of the zigzag and the Néel phases are quite similar at first glance. However, proximity-induced exchange coupling in graphene is completely different and the Dirac cones for spin up and spin down are indeed shifted in momentum space, see Fig. 4(b). As a result, band splittings are strongly direction dependent, see Fig. 4(c). However, our model is also capable of describing this situation with parameters summarized in Table II, as can be seen in Fig. 4(b,c). Interestingly, sublattice-resolved proximity exchange parameters of the antiferromagnetic zigzag phase are about 0.4 meV in magnitude, half of the value and opposite in sign compared to the ferromagnetic case, see Table II. Comparing the calculated spin polarizations on graphene in the ferromagnetic and antiferromagnetic zigzag phases [119], the opposite sign of proximity exchange is reasonable. In addition, the staggered potential parameter Δ is drastically enhanced compared to the other phases. Therefore, mainly one sublattice contributes to the spin polarization in the antiferromagnetic zigzag phase, while in the ferromagnetic phase, both sublattices contribute equally.

So far, we have seen all types of sublattice-resolved proximity-induced exchange coupling in graphene, uniform (positive and negative) and staggered, only by changing the magnetic phase of the MnPS_3 substrate.

D. Antiferromagnetic Stripy phase

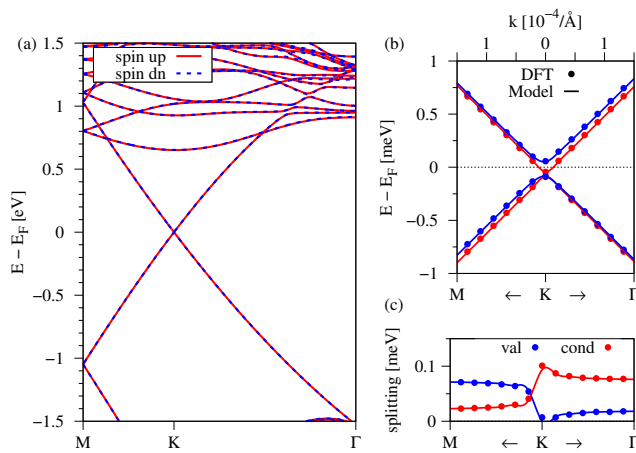


FIG. 5. Same as Fig. 2, when the MnPS_3 is in the antiferromagnetic stripy phase.

Finally, we consider the MnPS_3 monolayer to be in the antiferromagnetic stripy phase. Similar to the zigzag phase, the heterostructure has no symmetry and hopping amplitudes become inequivalent $t_{1,s} \neq t_{2,s} \neq t_{3,s}$. All relevant features of the dispersion are nearly identical to the antiferromagnetic zigzag phase. The main difference is that sublattice resolved proximity exchange

couplings and Dirac band splittings are much smaller in magnitude. Looking at the calculated spin polarization in real space [119], we find a similar picture as for the antiferromagnetic Néel phase, with opposite polarizations on the graphene sublattices. This scenario arises due to the small sublattice symmetry breaking Δ and small but uniform exchange parameters λ_{ex} in combination with slightly asymmetric hoppings.

In order to unveil specific trends on how the proximity-induced exchange depends on the specific material and magnetic phase, we plot in Fig. 6 the average coupling, $\lambda_{\text{ex}} = (\lambda_{\text{ex}}^{\text{A}} + \lambda_{\text{ex}}^{\text{B}})/2$ (listed in Tab. II). We only show the results for the ferromagnetic, antiferromagnetic Néel, and antiferromagnetic zigzag phases, since in the antiferromagnetic stripy phase we do not have data for all material combinations. In addition, the stripy phase is only energetically favorable in the case of CoPSe_3 .

Let us first discuss the dependence in the ferromagnetic phase (black data points). From Fig. 6 it is evident that λ_{ex} increases in magnitude in ascending order of the transition metal (Mn, Fe, Co, Ni), for Se-based MPX_3 materials. In addition, Mn, Fe, and Co provide negative λ_{ex} , while Ni provides positive λ_{ex} . The reason for the increasing magnitude can be seen from the density of states (DOS), see Supplemental Material [119]. Focusing on Se-based materials, the transition metal DOS contribution near the Dirac point continuously increases from Mn to Ni. Since these states from the transition metals provide magnetism and can couple to the Dirac electrons, the proximity exchange increases. In general it also seems that Se-based materials provide stronger proximity exchange compared to S-based ones. Focusing on the two antiferromagnetic phases (red and blue data points), we find that proximity exchange is much more suppressed compared to the ferromagnetic phase. This can be understood from the fact that an antiferromagnetic substrate has alternating magnetizations and therefore the exchange field that graphene can pick-up is diminished. In general, the antiferromagnetic Néel phase provides the smallest proximity exchange in graphene, while the antiferromagnetic zigzag phase can still provide moderate exchange coupling. This may be attributed to the different arrangements of magnetic metal ions below graphene. In the Néel phase, magnetic ions with different magnetization orientations form a regular pattern (considering one metal ion, the three nearest neighbors have opposite magnetizations). In contrast, in the zigzag phase, there are at least small "domains" (zigzag-stripes), where the magnetization is uniform (considering one metal ion, two nearest neighbors have the same magnetization).

E. Distance Study

Proximity exchange coupling is a short range effect and can be strongly enhanced by diminishing the interlayer distance between materials, as experimentally demonstrated for proximity SOC in graphene/TMDC het-

TABLE II. Fit parameters of Hamiltonian \mathcal{H} for the graphene/MPX₃ heterostructures for different magnetic phases (FM = ferromagnetic, AFM = antiferromagnetic) of the MPX₃. Calculations were performed without SOC. We list the hopping parameters $t_{\alpha,s}$, the staggered potential Δ , proximity exchange parameters $\lambda_{\text{ex}}^{\text{A}}$ and $\lambda_{\text{ex}}^{\text{B}}$, the Dirac point energy E_{D} , and the total energy E_{tot} , with respect to the ground state.

MPX ₃	magnetic phase	$t_{1,\uparrow}, t_{2,\uparrow}, t_{3,\uparrow} / t_{1,\downarrow}, t_{2,\downarrow}, t_{3,\downarrow}$ [eV]	Δ [μeV]	$\lambda_{\text{ex}}^{\text{A}}$ [μeV]	$\lambda_{\text{ex}}^{\text{B}}$ [μeV]	E_{D} [meV]	E_{tot} [meV]
MnPS ₃	FM	2.5038/2.5030	19.2	-219.6	-220.1	-0.047	231.4
	AFM Néel	2.5032/2.5032	42.3	-11.4	-13.0	0.029	0
	AFM Zigzag	2.5057,2.5032,2.5008/2.4997,2.5021,2.5046	629.2	469.5	463.1	0.060	91.8
	AFM Stripy	2.5035,2.5034,2.5033/2.5030,2.5032,2.5035	112.3	41.3	43.8	0.007	116.4
	FM ^a	2.5083/2.5070	68.9	-215.0	-232.9	-0.004	164.9
	AFM Néel ^a	2.5088/2.5086	67.7	20.2	-38.5	-0.001	0
MnPS ₃	FM	2.6144/2.6093	13.2	-850.9	-828.5	-0.004	238.8
	AFM Néel	2.6126/2.6126	52.9	-17.0	8.2	0.007	0
	AFM Zigzag	2.6136,2.6116,2.6097/2.6100,2.6120,2.6140	496.6	362.4	383.2	0.073	103.5
	AFM Stripy	2.6123,2.6122,2.6122/2.6120,2.6122,2.6124	32.9	35.1	12.0	-0.041	113.7
	FM ^a	2.6192/2.6109	24.5	-954.3	-1016.3	0.031	212.4
	AFM Néel ^a	2.6173/2.6173	35.4	14.6	-19.2	0.001	0
FePSe ₃	FM	2.5050/2.3475	3261.2	992.2	-5926.5	-8.6	1511.1
	AFM Néel ^b	-	-	-	-	-	1040.1
	AFM Zigzag	2.5054,2.5027,2.5015/2.5003,2.5026,2.5039	289.3	196.4	428.3	-0.001	0
	AFM Stripy	2.5028,2.5028,2.5031/2.4988,2.4997,2.5006	196.7	99.2	-94.1	0.880	275.5
FePS ₃	FM	2.6151/2.5824	364.7	430.8	-786.4	331.5	1735.0
	AFM Néel	2.6110/2.6109	126.9	-14.7	-63.2	550.9	1451.7
	AFM Zigzag	2.5996,2.5936,2.5891/2.6003,2.6019,2.6051	570.7	668.5	458.4	-0.229	0
	AFM Stripy	2.5452,2.5343,2.5470/2.5347,2.5429,2.5446	342.1	-183.9	455.0	-0.034	134.5
NiPSe ₃	FM	2.5036/1.9911	53.7	10764.4	10575.8	85.0	479.0
	AFM Néel	2.4797/2.4795	75.7	-36.0	-0.7	0.018	82.0
	AFM Zigzag	2.4851,2.4814,2.4779/2.4858,2.4883,2.4907	655.3	549.4	609.2	-0.126	0
	AFM Stripy ^b	-	-	-	-	-	535.7
NiPS ₃	FM	2.6130/2.3893	860.3	1538.5	115.1	387.2	291.1
	AFM Néel	2.5732/2.5755	114.6	53.1	-65.9	265.6	37.8
	AFM Zigzag	2.1102,2.1146,2.1169/2.0470,2.0545,2.0610	79.3	144.9	303.6	293.7	0
	AFM Stripy ^b	-	-	-	-	-	341.6
CoPSe ₃	FM	2.4221/2.5022	0.9	-3097.7	-3069.9	364.1	127.8
	AFM Néel	2.4786/2.4797	87.6	-91.7	39.5	363.4	1120.1
	AFM Zigzag	2.4506,2.4461,2.4415/2.4526,2.4509,2.4495	346.8	-12.2	37.4	370.4	1306.7
	AFM Stripy	2.4784,2.4781,2.4769/2.4848,2.4854,2.4847	65.2	55.9	-60.2	362.2	0
CoPS ₃	FM	2.6103/2.5989	43.7	-1337.2	-1261.7	562.7	534.0
	AFM Néel	2.5280/2.5269	115.2	-63.8	25.3	0.103	19.2
	AFM Zigzag	2.4576,2.4494,2.4414/2.5166,2.5237,2.5304	1371.3	1349.9	1442.2	0.067	0
	AFM Stripy ^b	-	-	-	-	-	229.9

^a Calculated with WIEN2k [91].

^b A reasonable fit could not be performed, as can be seen from the DFT-calculated band structure in the Supplemental Material.

erostuctures [107, 122]. In addition, in first-principles calculations, the equilibrium interlayer distance depends on the exchange-correlation functional and the vdW corrections, as for example demonstrated for graphite and hexagonal boron nitride [123].

How does the interlayer distance affect proximity

exchange effects in our bilayers? As an exemplary case we consider MnPS₃ in the antiferromagnetic Néel phase (ground state) and tune the distance d_{int} between graphene and the MnPS₃ monolayer. Especially this structure is interesting, since sublattice resolved proximity exchange parameters have opposite sign, $\lambda_{\text{ex}}^{\text{A}} < 0$

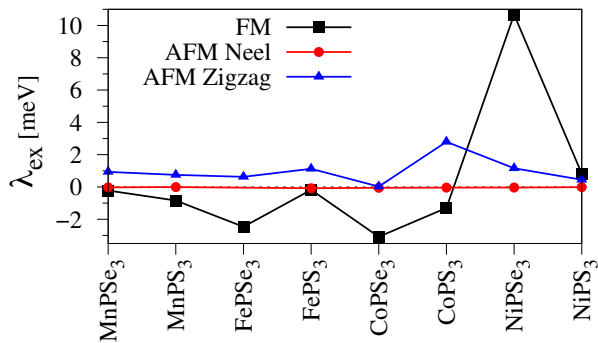


FIG. 6. The average proximity exchange coupling, λ_{ex} , as function of the substrate material and the magnetic phase (FM = ferromagnetic, AFM = antiferromagnetic).

and $\lambda_{\text{ex}}^{\text{B}} > 0$, see Table II, potentially important for the realization of novel topological states [52].

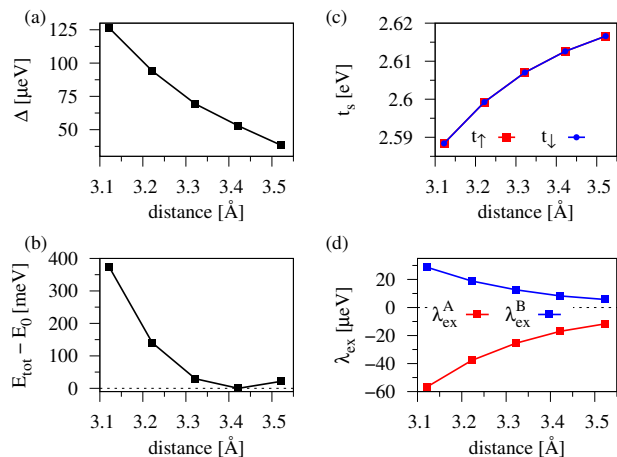


FIG. 7. Interlayer distance dependence of (a) the staggered potential Δ , (b) the total energy E_{tot} , (c) the spin dependent hopping parameters t_{\uparrow} and t_{\downarrow} , and (d) the sublattice resolved proximity exchange parameters $\lambda_{\text{ex}}^{\text{A}}$ and $\lambda_{\text{ex}}^{\text{B}}$ for the graphene/MnPS₃ heterostructure when the MnPS₃ is in the antiferromagnetic Néel phase.

In Fig. 7, we show the evolution of the fit parameters and the total energy as function of the interlayer distance for the graphene/MnPS₃ heterostructure. We notice that the staggered potential Δ increases with decreasing distance, because the sublattice-symmetry breaking in graphene gets stronger. The total energy is minimized for the relaxed interlayer distance given in Table I. The two spin dependent hopping parameters, t_{\uparrow} and t_{\downarrow} , have nearly the same value for this system, as can be seen in Table II, and decrease with decreasing van der Waals gap. The proximity exchange parameters $\lambda_{\text{ex}}^{\text{A}}$ and $\lambda_{\text{ex}}^{\text{B}}$ increase in magnitude with decreasing interlayer distance. We find that by decreasing d_{int} by about 10%, one can achieve a significant 5-fold enhancement of proximity exchange couplings. Important, the sign of both parameters, $\lambda_{\text{ex}}^{\text{A}} < 0$ and $\lambda_{\text{ex}}^{\text{B}} > 0$, is not affected.

In the Supplemental Material [119], we additionally show the evolution of the fit parameters as function of the interlayer distance for the graphene/MnPS₃ heterostructure in the antiferromagnetic Néel phase. There, we even find a crossover from uniform to staggered exchange couplings, when decreasing the interlayer distance. In conclusion, we expect similar behavior for the other material combinations and the different magnetic phases.

F. Hubbard U

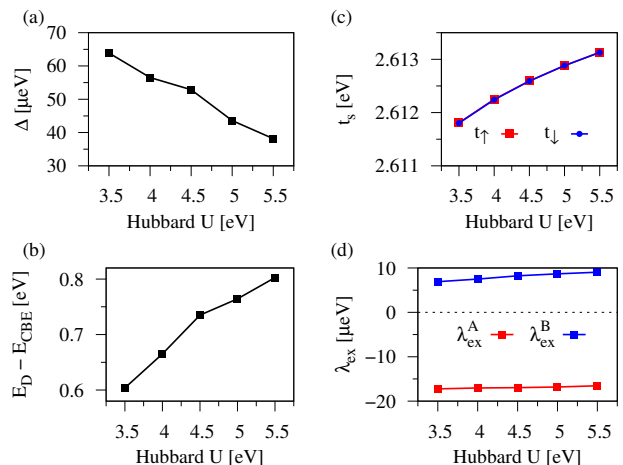


FIG. 8. Hubbard U dependence of (a) the staggered potential Δ , (b) the band offset of the Dirac point, E_{D} , with respect to the MnPS₃ conduction band edge, E_{CBE} , at the K point, (c) the spin dependent hopping parameters t_{\uparrow} and t_{\downarrow} , and (d) the sublattice resolved proximity exchange parameters $\lambda_{\text{ex}}^{\text{A}}$ and $\lambda_{\text{ex}}^{\text{B}}$ for the graphene/MnPS₃ heterostructure when the MnPS₃ is in the antiferromagnetic Néel phase.

The Hubbard U parameter is variable for the DFT calculations. How does the U affect proximity exchange splittings? Again, we consider graphene on MnPS₃ in the antiferromagnetic Néel phase and tune the U parameter between 3.5 to 5.5 eV, which is a typical range of values for d orbitals in strongly correlated materials. The results are summarized in Fig. 8. Overall, the fit parameters Δ , t_{\uparrow} , t_{\downarrow} , $\lambda_{\text{ex}}^{\text{A}}$, and $\lambda_{\text{ex}}^{\text{B}}$, barely change because for the graphene/MnPS₃ heterostructure, the Dirac bands are located at the Fermi level and well isolated from the substrate's bands, see Fig. 3(a). Even though the Hubbard U shifts the Mn d orbital levels in energy and tunes the band offset, the graphene states are nearly unaffected.

However, the effect of the Hubbard U on the fitted parameters can be also quite strong, as we demonstrate in the case of NiPS₃ in the antiferromagnetic zigzag phase (see Supplemental Material [119]). There, we find that proximity exchange couplings can be tuned from about 400 to 700 μeV within our considered range of the U parameter.

G. Transverse Electric Field

In experiment, gating is a tool to control proximity-induced exchange coupling as well as the doping level. How does a transverse electric field affect the Dirac bands in our scenario? Similar to before, we consider graphene on MnPS₃ in the antiferromagnetic Néel phase and apply an electric field across the heterostructure. The results are summarized in Fig. 9. Within our calculated field range of -2 to 3 V/nm, we find that the fitted parameters barely change. Most important, we can strongly tune the band offset of the Dirac point, E_D , with respect to the MnPS₃ conduction band edge, E_{CBE} , at the K point, see Fig. 9(b). For a field of 3 V/nm, we can bring the Dirac point at about 0.25 eV below the conduction band edge of the MnPS₃. In addition, it seems that the closer the Dirac cone gets to the conduction band edge, staggered potential and exchange couplings increase, while the hopping amplitudes decrease. Even though, the proximity exchange couplings are small in value, their relative tunability is giant, since they can be enhanced by about 30% by tuning the field from -2 to 3 V/nm. In general, the tunability should hold also for other magnetic phases, where proximity exchange is stronger.

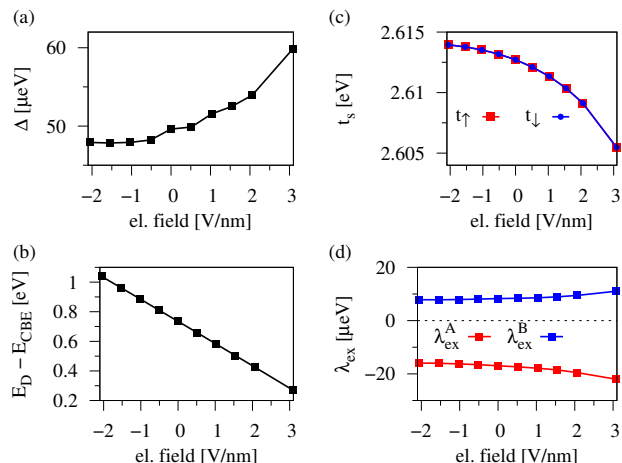


FIG. 9. Transverse electric field dependence of (a) the staggered potential Δ , (b) the band offset of the Dirac point, E_D , with respect to the MnPS₃ conduction band edge, E_{CBE} , at the K point, (c) the spin dependent hopping parameters t_\uparrow and t_\downarrow , and (d) the sublattice resolved proximity exchange parameters λ_{ex}^A and λ_{ex}^B for the graphene/MnPS₃ heterostructure when the MnPS₃ is in the antiferromagnetic Néel phase.

H. Effects of SOC

So far, we have not included SOC in the calculations. Since the number of possible heterostructures in different magnetic phases is too large, we limit ourselves to a few selected cases and check how the inclusion of SOC

influences the low energy graphene Dirac bands. For simplicity, we only consider Mn-based MPX₃ monolayers in the ferromagnetic phase. This should be enough to find out about the magnitude of the proximity-induced SOC, which we can compare to the induced exchange coupling. In addition, when SOC is included, we employ constrained magnetization calculations (forcing the magnetization parallel to z direction), since **Quantum ESPRESSO** implements noncollinear magnetism. Note, that the plane wave and pseudopotential method, implemented in **Quantum ESPRESSO**, does not correctly reproduce the intrinsic SOC values of bare monolayer graphene ($12 \mu\text{eV}$), since the relevant d -orbitals are not present [124, 125]. However, proximity-induced SOC (if present) is captured.

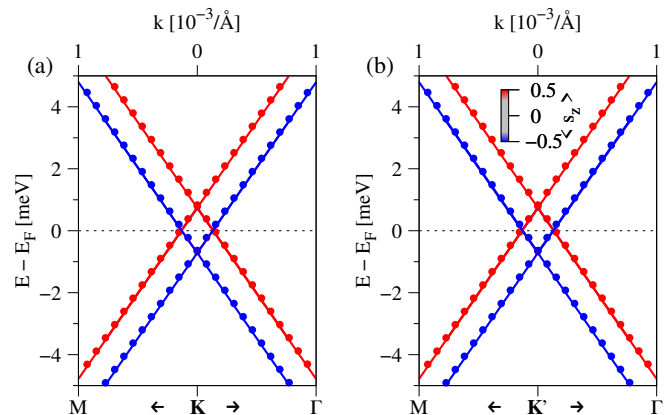


FIG. 10. (a) DFT-calculated low energy Dirac bands near the K point for the graphene/MnPS₃ heterostructure, when MnPS₃ is in the ferromagnetic phase and SOC is included. The symbols are color coded by their s_z spin expectation value. (b) Same as (a) but near the K' point.

In Fig. 10, we show the DFT-calculated low energy bands near the K and K' points of the graphene/MnPS₃ heterostructure, when MnPS₃ is in the ferromagnetic phase and SOC is included. We find that bands near the K and K' valleys are nearly identical and fully s_z polarized, indicating that proximity-induced SOC is negligible compared to the exchange one. Indeed, comparing the calculated low energy bands from Fig. 10 (with SOC) and Fig. 2 (without SOC), we find no marked change by inclusion of SOC. This result is not surprising, because recent calculations have shown that SOC effects are small in bare monolayer MnPS₃ in the antiferromagnetic Néel phase [68]. Therefore, also proximity-induced SOC is small, even though we consider the ferromagnetic phase here. Similar results hold for MnPSe₃ in the ferromagnetic phase (low-energy dispersions with SOC are not shown).

I. Further Discussion

In some cases, band hybridization (anticrossings) additionally affect the Dirac bands, leading to renormalized proximity-induced exchange splittings, as previously shown for graphene/hBN/Co heterostructures [117]. Similar things can happen here, for example in the case of graphene/NiPSe₃ in the ferromagnetic phase, spin down bands originating from the NiPSe₃ are located near the Dirac point energy and hybridize with the spin down Dirac states, see the band structure in the Supplemental Material [119]. As a consequence, the effective proximity exchange parameters are much larger (10 meV) than for any other case we consider here. Also the spin down hopping parameter t_{\downarrow} differs by about 0.5 eV from the spin up one t_{\uparrow} , see Table II. For the graphene/NiPS₃ structure in the antiferromagnetic zigzag phase, the band hybridization is even more pronounced, since NiPS₃ bands from both spin species are present near the Dirac point.

Whenever bands, which originate from the magnetic MPX₃ substrate, are located near the Dirac point energy, band hybridization can occur. As a consequence, the spin splitting of the graphene Dirac states is affected, in addition to the bare proximity-induced exchange coupling. By comparing the band structures and fitted parameters from all of our structures, this happens only in a few cases we consider here. However, from previous studies [117, 126], we know that band offsets can be influenced by the interlayer distance, a transverse electric field, or the Hubbard U . In our exemplary case of MnPS₃ in the antiferromagnetic Néel phase, we have seen that the interlayer distance strongly affects proximity exchange, while the Hubbard U does not, since band hybridization effects are absent (given the large band offset). This behavior can be very different in other heterostructures, especially in cases where band hybridization already occurs.

Does another DFT code give similar results? We additionally employ the full-potential linearized augmented plane wave code WIEN2k [91] and recalculate the dispersion for some of our structures. The fit results are also summarized in Table II. We consider graphene on MnPS₃ and MnPSe₃ in the ferromagnetic and antiferromagnetic Néel phases, respectively. Because of the broken symmetry in the antiferromagnetic zigzag and stripy phases, WIEN2k calculations are computationally too demanding and thus not included in this study. The purpose to employ two different codes is to test the robustness of our predictions (magnitudes and signs of proximity exchange parameters).

Both codes predict the antiferromagnetic Néel phase to be the ground state for MnPSe₃ and MnPS₃, in agreement with experimental data. For both substrates in both magnetic phases, WIEN2k predicts similar proximity exchange splittings as Quantum ESPRESSO. For MnPSe₃, results of the antiferromagnetic Néel phase differ. The different DFT codes predict small exchange parameters, but of different type (WIEN2k predicts staggered ones, while Quantum ESPRESSO predicts uniform ones). For

MnPS₃ in the antiferromagnetic Néel phase, the sublattice resolved proximity exchange parameters are staggered for both codes, but with a global sign change. The results for the ferromagnetic phases coincide for both materials and both codes. Indeed, when proximity exchange is larger than about 100 μeV , both codes essentially agree, as we can see from the ferromagnetic phase results. However, when the proximity effects become rather small (few to tens of μeV), the codes reach their limits in numerical accuracy and discrepancies may arise, as we can see from the antiferromagnetic Néel phase results. We conclude that, whenever exchange parameters are small (few to tens of μeV), a precise prediction of results is computationally very challenging and the extracted parameters should be treated with caution. However, we do not see this as a critical problem, since the magnitudes of the proximity exchange in the different magnetic phases are the same, independent of the DFT code. The proximity effects depend on the hybridization of the orbitals across the interface, and on the energies of the orbitals that take part of the hybridizations. The energetics of higher lying orbitals depends on the code, which is most likely causing the discrepancies.

Finally, we want to comment on the magnetic easy axis of the substrate MPX₃ materials. In our calculations, we have considered only out-of-plane (collinear to z direction) magnetic configurations. Otherwise, the calculations would be computationally very demanding since noncollinear magnetism needs to be treated, which is accompanied by inclusion of SOC. However, for some MPX₃ monolayers, experiments and theory indicate in-plane antiferromagnetism, such as for NiPS₃ [56, 105]. Therefore, one should keep in mind that our presented results of proximity exchange may be different in real samples. With our DFT approach, we can give at most rough predictions and indications. Nevertheless, we find that the class of magnetic MPX₃ monolayers is highly interesting in terms of proximity effects, as different types and magnitudes of exchange coupling can be induced in graphene. We also hope that future experiments can confirm at least some of our findings and that the potential of these materials will be recognized for future spintronics applications.

V. SUMMARY

In this work, we have considered heterostructures of graphene and the magnetic transition-metal phosphorus trichalcogenides MPX₃. From first-principles calculations, we have extracted the proximitized Dirac bands of graphene, which we fitted to a model Hamiltonian, including orbital and proximity exchange parameters. We found that, depending on the magnetic phase of the MPX₃ substrate layer, the metal atom $M=\{\text{Mn,Fe,Ni,Co}\}$, and the chalcogen atom $X=\{\text{S,Se}\}$, very different proximity-induced exchange couplings can be realized in graphene. Not only that the exchange split-

tings range from about 0 to 10 meV, also the sign and type of the exchange couplings differ from case to case. We demonstrated, that the MPX_3 family of magnetic monolayers are a platform to induce uniform ($\lambda_{\text{ex}}^{\text{A}} \approx \lambda_{\text{ex}}^{\text{B}}$), as well as staggered ($\lambda_{\text{ex}}^{\text{A}} \approx -\lambda_{\text{ex}}^{\text{B}}$) exchange couplings in graphene, leading to very different spin polarizations. In addition, decreasing the interlayer distance between graphene and the substrate is a very efficient tool to enhance proximity-induced exchange couplings. An applied transverse electric field can potentially result in a similar tunability, but was not observed in our exemplary case. The Hubbard U , which is a parameter in the DFT calculation, can have a huge impact on Dirac band splittings, since the U determines the band alignment and to some

extent the coupling of the monolayers. Finally, we found that for Mn-based materials in the ferromagnetic phase, the proximity-induced SOC is negligible compared to the exchange parameters.

ACKNOWLEDGMENTS

This work was funded by the Deutsche Forschungsgemeinschaft (DFG, German Research Foundation) SFB 1277 (Project No. 314695032), SPP 2244 (Project No. 443416183), and the European Union Horizon 2020 Research and Innovation Program under contract number 881603 (Graphene Flagship).

-
- [1] Klaus Zollner, Marko D. Petrović, Kapildeb Dolui, Petr Plecháč, Branislav K. Nikolić, and Jaroslav Fabian, “Scattering-induced and highly tunable by gate damping-like spin-orbit torque in graphene doubly proximitized by two-dimensional magnet $\text{Cr}_2\text{Ge}_2\text{Te}_6$ and monolayer WS_2 ,” *Phys. Rev. Research* **2**, 043057 (2020).
 - [2] Kapildeb Dolui, Marko D Petrovic, Klaus Zollner, Petr Plechac, Jaroslav Fabian, and Branislav K Nikolic, “Proximity spin-orbit torque on a two-dimensional magnet within van der Waals heterostructure: current-driven antiferromagnet-to-ferromagnet reversible nonequilibrium phase transition in bilayer CrI_3 ,” *Nano letters* **20**, 2288–2295 (2020).
 - [3] Tiancheng Song, Xinghan Cai, Matisse Wei-Yuan Tu, Xiaou Zhang, Bevin Huang, Nathan P. Wilson, Kyle L. Seyler, Lin Zhu, Takashi Taniguchi, Kenji Watanabe, Michael A. McGuire, David H. Cobden, Di Xiao, Wang Yao, and Xiaodong Xu, “Giant tunneling magnetoresistance in spin-filter van der Waals heterostructures,” *Science* **360**, 1214 (2018).
 - [4] Mohammed Alghamdi, Mark Lohmann, Junxue Li, Palani R Jothi, Qiming Shao, Mohammed Aldosary, Tang Su, Boniface P. T. Fokwa, and Jing Shi, “Highly Efficient Spin-Orbit Torque and Switching of Layered Ferromagnet Fe_3GeTe_2 ,” *Nano Lett.* **19**, 4400 (2019).
 - [5] Vaibhav Ostwal, Tingting Shen, and Joerg Appenzeller, “Efficient spin-orbit torque switching of the semi-conducting van der Waals ferromagnet $\text{Cr}_2\text{Ge}_2\text{Te}_6$,” *Advanced Materials* **32**, 1906021 (2020).
 - [6] Bing Zhao, Roselle Ngaloy, Anamul Md Hoque, Bogdan Karpiak, Dmitrii Khokhriakov, and Saroj P Dash, “Van der Waals magnet based spin-valve devices at room temperature,” *arXiv:2107.00310* (2021).
 - [7] Wei Han, K. Pi, K. M. McCreary, Yan Li, Jared J. I. Wong, A. G. Swartz, and R. K. Kawakami, “Tunneling spin injection into single layer graphene,” *Phys. Rev. Lett.* **105**, 167202 (2010).
 - [8] G. Schmidt, D. Ferrand, L. W. Molenkamp, A. T. Filip, and B. J. van Wees, “Fundamental obstacle for electrical spin injection from a ferromagnetic metal into a diffusive semiconductor,” *Phys. Rev. B* **62**, R4790–R4793 (2000).
 - [9] E. I. Rashba, “Theory of electrical spin injection: Tunnel contacts as a solution of the conductivity mismatch problem,” *Phys. Rev. B* **62**, R16267–R16270 (2000).
 - [10] Wei Han, Roland K Kawakami, Martin Gmitra, and Jaroslav Fabian, “Graphene spintronics,” *Nat. Nanotechnol.* **9**, 794 (2014).
 - [11] A. Fert and H. Jaffres, “Conditions for efficient spin injection from a ferromagnetic metal into a semiconductor,” *Phys. Rev. B* **64**, 184420 (2001).
 - [12] Talieh S. Ghiasi, Alexey A. Kaverzin, Avalon H. Dismukes, Dennis K. de Wal, Xavier Roy, and Bart J. van Wees, “Electrical and thermal generation of spin currents by magnetic bilayer graphene,” *Nature Nanotechnology* **16**, 788–794 (2021).
 - [13] Alexey A Kaverzin, Talieh S Ghiasi, Avalon H Dismukes, Xavier Roy, and Bart J van Wees, “Towards fully two-dimensional spintronic devices,” *arXiv:2202.09972* (2022).
 - [14] Dmitrii Khokhriakov, Shehrin Sayed, Anamul Md Hoque, Bogdan Karpiak, Bing Zhao, Supriyo Datta, and Saroj P Dash, “Multifunctional spin logic gates in graphene spin circuits,” *arXiv:2108.12259* (2021).
 - [15] Dmitrii Khokhriakov, Bogdan Karpiak, Anamul Md. Hoque, and Saroj P. Dash, “Two-dimensional spintronic circuit architectures on large scale graphene,” *Carbon* **161**, 892–899 (2020).
 - [16] Martin Gmitra and Jaroslav Fabian, “Graphene on transition-metal dichalcogenides: A platform for proximity spin-orbit physics and optospintronics,” *Phys. Rev. B* **92**, 155403 (2015).
 - [17] Martin Gmitra, Denis Kochan, Petra Högl, and Jaroslav Fabian, “Trivial and inverted Dirac bands and the emergence of quantum spin Hall states in graphene on transition-metal dichalcogenides,” *Phys. Rev. B* **93**, 155104 (2016).
 - [18] Yang Li and Mikito Koshino, “Twist-angle dependence of the proximity spin-orbit coupling in graphene on transition-metal dichalcogenides,” *Phys. Rev. B* **99**, 075438 (2019).
 - [19] Alessandro David, Péter Rakyta, Andor Kormányos, and Guido Burkard, “Induced spin-orbit coupling in twisted graphene-transition metal dichalcogenide heterobilayers: Twistronics meets spintronics,” *Phys. Rev. B* **100**, 085412 (2019).
 - [20] Thomas Naimier, Klaus Zollner, Martin Gmitra, and Jaroslav Fabian, “Twist-angle dependent proximity induced spin-orbit coupling in graphene/transition metal

- dichalcogenide heterostructures,” *Physical Review B* **104**, 195156 (2021).
- [21] Armando Pezo, Zeila Zanolli, Nils Wittemeier, Pablo Ordejón, Adalberto Fazzio, Stephan Roche, and Jose H Garcia, “Manipulation of spin transport in graphene/transition metal dichalcogenide heterobilayers upon twisting,” *2D Materials* **9**, 015008 (2021).
- [22] Csaba G. Péterfalvi, Alessandro David, Péter Rakyta, Guido Burkard, and Andor Kormányos, “Quantum interference tuning of spin-orbit coupling in twisted van der waals trilayers,” arXiv:2111.02781 (2021), 10.48550/ARXIV.2111.02781.
- [23] Alessandro Veneri, David TS Perkins, Csaba G Péterfalvi, and Aires Ferreira, “Twist-angle controlled collinear edelstein effect in van der waals heterostructures,” arXiv:2205.08804 (2022).
- [24] Seungjun Lee, D. J. P. de Sousa, Young-Kyun Kwon, Fernando de Juan, Zhendong Chi, Félix Casanova, and Tony Low, “Charge-to-spin conversion in twisted graphene/wse₂ heterostructures,” arXiv:2206.09478 (2022).
- [25] L Antonio Benitez, Williams Savero Torres, Juan F Sierra, Matias Timmermans, Jose H Garcia, Stephan Roche, Marius V Costache, and Sergio O Valenzuela, “Tunable room-temperature spin galvanic and spin Hall effects in van der Waals heterostructures,” *Nat. Mater.* **19**, 170 (2020).
- [26] Manuel Offidani, Mirco Milletari, Roberto Raimondi, and Aires Ferreira, “Optimal charge-to-spin conversion in graphene on transition-metal dichalcogenides,” *Phys. Rev. Lett.* **119**, 196801 (2017).
- [27] Talieh S Ghiasi, Alexey A Kaverzin, Patrick J Blah, and Bart J van Wees, “Charge-to-Spin Conversion by the Rashba–Edelstein Effect in Two-Dimensional van der Waals Heterostructures up to Room Temperature,” *Nano Lett.* **19**, 5959 (2019).
- [28] Dmitrii Khokhriakov, Anamul Md. Hoque, Bogdan Karpiak, and Saroj P. Dash, “Gate-tunable spin-galvanic effect in graphene-topological insulator van der waals heterostructures at room temperature,” *Nature Communications* **11** (2020), 10.1038/s41467-020-17481-1.
- [29] Franz Herling, C. K. Safeer, Josep Ingla-Aynés, Nerea Ontoso, Luis E. Hueso, and Félix Casanova, “Gate tunability of highly efficient spin-to-charge conversion by spin hall effect in graphene proximitized with wse₂,” *APL Materials* **8**, 071103 (2020).
- [30] C K Safeer, Franz Herling, Won Young Choi, Nerea Ontoso, Josep Ingla-Aynés, Luis E Hueso, and Felix Casanova, “Reliability of spin-to-charge conversion measurements in graphene-based lateral spin valves,” *2D Materials* **9**, 015024 (2021).
- [31] Carmen Monaco, Aires Ferreira, and Roberto Raimondi, “Spin hall and inverse spin galvanic effects in graphene with strong interfacial spin-orbit coupling: A quasi-classical green’s function approach,” *Phys. Research* **3**, 033137 (2021).
- [32] Aires Ferreira, “Theory of spin-charge-coupled transport in proximitized graphene: an SO(5) algebraic approach,” *Journal of Physics: Materials* **4**, 045006 (2021).
- [33] Mirco Milletari, Manuel Offidani, Aires Ferreira, and Roberto Raimondi, “Covariant conservation laws and the spin hall effect in dirac-rashba systems,” *Physical review letters* **119**, 246801 (2017).
- [34] A Dyrdał, J Barnaś, and VK Dugaev, “Current-induced spin polarization in graphene due to rashba spin-orbit interaction,” *Physical Review B* **89**, 075422 (2014).
- [35] Jose H Garcia, Aron W Cummings, and Stephan Roche, “Spin hall effect and weak antilocalization in graphene/transition metal dichalcogenide heterostructures,” *Nano letters* **17**, 5078–5083 (2017).
- [36] Anamul Md Hoque, Dmitrii Khokhriakov, Klaus Zollner, Bing Zhao, Bogdan Karpiak, Jaroslav Fabian, and Saroj P Dash, “All-electrical creation and control of spin-galvanic signal in graphene and molybdenum ditelluride heterostructures at room temperature,” *Communications Physics* **4**, 124 (2021).
- [37] Regina Galceran, Bo Tian, Junzhu Li, Frédéric Bonell, Matthieu Jamet, Céline Vergnaud, Alain Marty, Jose H. García, Juan F. Sierra, Marius V. Costache, Stephan Roche, Sergio O. Valenzuela, Aurélien Manchon, Xixiang Zhang, and Udo Schwingenschlögl, “Control of spin-charge conversion in van der waals heterostructures,” *APL Materials* **9**, 100901 (2021).
- [38] Aron W. Cummings, Jose H. Garcia, Jaroslav Fabian, and Stephan Roche, “Giant spin lifetime anisotropy in graphene induced by proximity effects,” *Phys. Rev. Lett.* **119**, 206601 (2017).
- [39] Talieh S. Ghiasi, Josep Ingla-Aynés, Alexey A. Kaverzin, and Bart J. Van Wees, “Large Proximity-Induced Spin Lifetime Anisotropy in Transition-Metal Dichalcogenide/Graphene Heterostructures,” *Nano Lett.* **17**, 7528 (2017).
- [40] Simon Zihlmann, Aron W. Cummings, Jose H. Garcia, Máté Kedves, Kenji Watanabe, Takashi Taniguchi, Christian Schönenberger, and Péter Makk, “Large spin relaxation anisotropy and valley-zeeman spin-orbit coupling in wse₂/graphene/h-bn heterostructures,” *Phys. Rev. B* **97**, 075434 (2018).
- [41] Johannes Christian Leutenantsmeyer, Josep Ingla-Aynés, Jaroslav Fabian, and Bart J. van Wees, “Observation of Spin-Valley-Coupling-Induced Large Spin-Lifetime Anisotropy in Bilayer Graphene,” *Phys. Rev. Lett.* **121**, 127702 (2018).
- [42] S. Omar, B. N. Madhushankar, and B. J. van Wees, “Large spin-relaxation anisotropy in bilayer-graphene/ws₂ heterostructures,” *Phys. Rev. B* **100**, 155415 (2019).
- [43] Manuel Offidani and Aires Ferreira, “Microscopic theory of spin relaxation anisotropy in graphene with proximity-induced spin-orbit coupling,” *Phys. Rev. B* **98**, 245408 (2018).
- [44] Jiayong Zhang, Bao Zhao, Yugui Yao, and Zhongqin Yang, “Robust quantum anomalous hall effect in graphene-based van der waals heterostructures,” *Phys. Rev. B* **92**, 165418 (2015).
- [45] Bogdan Karpiak, Aron W. Cummings, Klaus Zollner, Marc Vila, Dmitrii Khokhriakov, Anamul Md Hoque, André Dankert, Peter Svedlindh, Jaroslav Fabian, Stephan Roche, and Saroj P. Dash, “Magnetic proximity in a van der Waals heterostructure of magnetic insulator and graphene,” *2D Mater.* **7**, 015026 (2019).
- [46] Jiayong Zhang, Bao Zhao, Tong Zhou, Yang Xue, Chunlan Ma, and Zhongqin Yang, “Strong magnetization and Chern insulators in compressed graphene/CrI₃ van der Waals heterostructures,” *Phys. Rev. B* **97**, 085401 (2018).

- [47] M Umar Farooq and Jisang Hong, “Switchable valley splitting by external electric field effect in graphene/crI 3 heterostructures,” *npj 2D Materials and Applications* **3**, 3 (2019).
- [48] C. Cardoso, D. Soriano, N. A. García-Martínez, and J. Fernández-Rossier, “Van der waals spin valves,” *Phys. Rev. Lett.* **121**, 067701 (2018).
- [49] Kyle L. Seyler, Ding Zhong, Bevin Huang, Xiayu Linpeng, Nathan P. Wilson, Takashi Taniguchi, Kenji Watanabe, Wang Yao, Di Xiao, Michael A. McGuire, Kai-Mei C. Fu, and Xiaodong Xu, “Valley Manipulation by Optically Tuning the Magnetic Proximity Effect in WSe 2 /CrI 3 Heterostructures,” *Nano Lett.* **18**, 3823 (2018).
- [50] Klaus Zollner and Jaroslav Fabian, “Engineering proximity exchange by twisting: Reversal of ferromagnetic and emergence of antiferromagnetic dirac bands in Graphene/cr₂ge₂te₆,” *Phys. Rev. Lett.* **128**, 106401 (2022).
- [51] Shiming Yan, Shengmei Qi, Dunhui Wang, and Wenbo Mi, “Novel electronic structures and magnetic properties in twisted two-dimensional graphene/janus 2h–vsete heterostructures,” *Physica E: Low-dimensional Systems and Nanostructures* **134**, 114854 (2021).
- [52] Petra Högl, Tobias Frank, Klaus Zollner, Denis Kochan, Martin Gmitra, and Jaroslav Fabian, “Quantum anomalous hall effects in graphene from proximity-induced uniform and staggered spin-orbit and exchange coupling,” *Phys. Rev. Lett.* **124**, 136403 (2020).
- [53] Marc Vila, Jose H. Garcia, and Stephan Roche, “Valley-polarized quantum anomalous hall phase in bilayer graphene with layer-dependent proximity effects,” *Phys. Rev. B* **104**, L161113 (2021).
- [54] A Wiedenmann, J. Rossat-Mignod, A Louisy, R Brec, and J Rouxel, “Neutron diffraction study of the layered compounds MnPSe₃ and FePSe₃,” *Solid State Commun.* **40**, 1067 (1981).
- [55] Maria Ramos, Felix Carrascoso, Riccardo Frisenda, Patricia Gant, Samuel Mañas-Valero, Dorye L Esteras, José J Baldoví, Eugenio Coronado, Andres Castellanos-Gomez, and M Reyes Calvo, “Ultra-broad spectral photo-response in feps3 air-stable devices,” *npj 2D Materials and Applications* **5**, 19 (2021).
- [56] D. Lançon, R. A. Ewings, T. Guidi, F. Formisano, and A. R. Wildes, “Magnetic exchange parameters and anisotropy of the quasi-two-dimensional antiferromagnet nips₃,” *Phys. Rev. B* **98**, 134414 (2018).
- [57] Haoyong Lu, Wei Wang, Yun Liu, Limin Chen, Qiyun Xie, Handi Yin, Guofeng Cheng, and Liang He, “Exfoliation, lattice vibration and air stability characterization of antiferromagnetic van der waals nips₃ nanosheets,” *Applied Surface Science* **504**, 144405 (2020).
- [58] Nikhil Sivadas, Matthew W. Daniels, Robert H. Swendsen, Satoshi Okamoto, and Di Xiao, “Magnetic ground state of semiconducting transition-metal trichalcogenide monolayers,” *Phys. Rev. B* **91**, 235425 (2015).
- [59] G. Le Flem, R. Brec, G. Ouvard, A. Louisy, and P. Segransan, “Magnetic interactions in the layer compounds mpx₃ (m = mn, fe, ni; x = s, se),” *Journal of Physics and Chemistry of Solids* **43**, 455 – 461 (1982).
- [60] Jae-Ung Lee, Sungmin Lee, Ji Hoon Ryoo, Soonmin Kang, Tae Yun Kim, Pilkwang Kim, Cheol-Hwan Park, Je-Geun Park, and Hyeonsik Cheong, “Ising-Type Magnetic Ordering in Atomically Thin FePS₃,” *Nano Lett.* **16**, 7433–7438 (2016).
- [61] Bheema Lingam Chittari, Dongkyu Lee, Nepal Banerjee, Allan H. MacDonald, Euyheon Hwang, and Jeil Jung, “Carrier- and strain-tunable intrinsic magnetism in two-dimensional MAX₃ transition metal chalcogenides,” *Phys. Rev. B* **101**, 085415 (2020).
- [62] Bheema Lingam Chittari, Youngju Park, Dongkyu Lee, Moonsup Han, Allan H. MacDonald, Euyheon Hwang, and Jeil Jung, “Electronic and magnetic properties of single-layer mPX₃ metal phosphorous trichalcogenides,” *Phys. Rev. B* **94**, 184428 (2016).
- [63] P. A. Joy and S. Vasudevan, “Magnetism in the layered transition-metal thiophosphates mps₃ (m=mn, fe, and ni),” *Phys. Rev. B* **46**, 5425–5433 (1992).
- [64] Yinxiang Li, Xianxin Wu, Yuhao Gu, Congcong Le, Shengshan Qin, Ronny Thomale, and Jiangping Hu, “Topological superconductivity in ni-based transition metal trichalcogenides,” *Phys. Rev. B* **100**, 214513 (2019).
- [65] W. Klिंगen, G. Eulenberger, and H. Hahn, “Über Hexathio- und Hexaselenohypodiphosphate vom Typ M 2 II P₂X₆,” *Naturwissenschaften* **55**, 229–230 (1968).
- [66] Qi Pei, Xiaocha Wang, Jijun Zou, and Wenbo Mi, “Tunable electronic structure and magnetic coupling in strained two-dimensional semiconductor MnPSe₃,” *Front. Phys.* **13**, 137105 (2018).
- [67] Xiao Li, Ting Cao, Qian Niu, Junren Shi, and Ji Feng, “Coupling the valley degree of freedom to antiferromagnetic order,” *Proceedings of the National Academy of Sciences* **110**, 3738–3742 (2013).
- [68] Juntao Yang, Yong Zhou, Qilin Guo, Yuriy Dedkov, and Elena Voloshina, “Electronic, magnetic and optical properties of mpx₃ (x= s, se) monolayers with and without chalcogen defects: a first-principles study,” *RSC Advances* **10**, 851–864 (2020).
- [69] Muhammad Nauman, Do Hoon Kiem, Sungmin Lee, Suhan Son, Je-Geun Park, Woun Kang, Myung Joon Han, and Younjung Jo, “Complete mapping of magnetic anisotropy for prototype ising van der waals FePS₃,” *2D Materials* **8**, 035011 (2021).
- [70] Carmine Autieri, Giuseppe Cuono, Canio Noce, Milosz Rybak, Kamila M Kotur, Clio Efthimia Agrapidis, Krzysztof Wohlfeld, and Magdalena Birowska, “Limited ferromagnetic interactions in monolayers of mps₃ (m= mn and ni),” *The Journal of Physical Chemistry C* **126**, 6791–6802 (2022).
- [71] Adam K Budniak, Szymon J Zelewski, Magdalena Birowska, Tomasz Woźniak, Tatyana Bendikova, Yaron Kauffmann, Yaron Amouyal, Robert Kudrawiec, and Efrat Lifshitz, “Spectroscopy and structural investigation of iron phosphorus trisulfide—feps₃,” *Advanced Optical Materials* **10**, 2102489 (2022).
- [72] Rabindra Basnet, K Kotur, M Rybak, Cory Stephenson, Samuel Bishop, C Autieri, M Birowska, and Jin Hu, “Controlling magnetic exchange and anisotropy by non-magnetic ligand substitution in layered mpx₃ (m= ni, mn; x= s, se),” *arXiv:2205.04585* (2022).
- [73] Rutuparna Samal, Gopal Sanyal, Brahmananda Chakraborty, and Chandra Sekhar Rout, “Two-dimensional transition metal phosphorous trichalcogenides (mpx₃): a review on emerging trends, current state and future perspectives,” *Journal of Materials*

- Chemistry A **9**, 2560–2591 (2021).
- [74] S Calder, AV Haglund, Alexander I Kolesnikov, and David Mandrus, “Magnetic exchange interactions in the van der waals layered antiferromagnet mnps_3 ,” *Physical Review B* **103**, 024414 (2021).
- [75] Thuc T Mai, Kevin F Garrity, Amber McCreary, Joshua Argo, Jeffrey R Simpson, Vicky Doan-Nguyen, Rolando Valdés Aguilar, and Angela R Hight Walker, “Magnon-phonon hybridization in 2d antiferromagnet mnpse_3 ,” *Science advances* **7**, eabj3106 (2021).
- [76] Magdalena Birowska, Paulo E. Faria Junior, Jaroslav Fabian, and Jens Kunstmann, “Large exciton binding energies in mnpse_3 as a case study of a van der waals layered magnet,” *Phys. Rev. B* **103**, L121108 (2021).
- [77] Florian Dirnberger, Rezlind Bushati, Biswajit Datta, Ajesh Kumar, Allan H. MacDonald, Edoardo Baldini, and Vinod M. Menon, “Observation of spin-correlated exciton-polaritons in a van der waals magnet,” *arXiv:2203.06129* (2022).
- [78] Qi Pei, Yan Song, Xiaocha Wang, Jijun Zou, and Wenbo Mi, “Superior Electronic Structure in Two-Dimensional $\text{MnPSe}_3/\text{MoS}_2$ van der Waals Heterostructures,” *Sci. Rep.* **7**, 9504 (2017).
- [79] John R. Schaibley, Hongyi Yu, Genevieve Clark, Pasqual Rivera, Jason S. Ross, Kyle L. Seyler, Wang Yao, and Xiaodong Xu, “Valleytronics in 2D materials,” *Nat. Rev. Mater.* **1**, 16055 (2016).
- [80] Steven A Vitale, Daniel Nezich, Joseph O Varghese, Philip Kim, Nuh Gedik, Pablo Jarillo-Herrero, Di Xiao, and Mordechai Rothschild, “Valleytronics: Opportunities, challenges, and paths forward,” *Small* **14**, 1801483 (2018).
- [81] Luman Zhang, Xinyu Huang, Hongwei Dai, Mingshan Wang, Hui Cheng, Lei Tong, Zheng Li, Xiaotao Han, Xia Wang, Lei Ye, and Junbo Han, “Proximity-coupling-induced significant enhancement of coercive field and curie temperature in 2d van der waals heterostructures,” *Advanced Materials* **32**, 2002032 (2020).
- [82] C. F. Schippers, H. J. M. Swagten, and M. H. D. Guimarães, “Large interfacial spin-orbit torques in layered antiferromagnetic insulator NiPs_3 /ferromagnet bilayers,” *Phys. Rev. Materials* **4**, 084007 (2020).
- [83] P. Hohenberg and W. Kohn, “Inhomogeneous electron gas,” *Phys. Rev.* **136**, B864 (1964).
- [84] Paolo Giannozzi and et al., “Quantum espresso: a modular and open-source software project for quantum simulations of materials,” *J. Phys.: Cond. Mat.* **21**, 395502 (2009).
- [85] Qi Pei, Xiaocha Wang, Jijun Zou, and Wenbo Mi, “Efficient band structure modulations in two-dimensional $\text{MnPSe}_3/\text{CrSiTe}_3$ van der Waals heterostructures,” *Nanotechnology* **29**, 214001 (2018).
- [86] G. Kresse and D. Joubert, “From ultrasoft pseudopotentials to the projector augmented-wave method,” *Phys. Rev. B* **59**, 1758 (1999).
- [87] John P. Perdew, Kieron Burke, and Matthias Ernzerhof, “Generalized gradient approximation made simple,” *Phys. Rev. Lett.* **77**, 3865 (1996).
- [88] Stefan Grimme, “Semiempirical gga-type density functional constructed with a long-range dispersion correction,” *J. Comput. Chem.* **27**, 1787 (2006).
- [89] Stefan Grimme, Jens Antony, Stephan Ehrlich, and Helge Krieg, “A consistent and accurate ab initio parametrization of density functional dispersion correction (DFT-D) for the 94 elements H-Pu,” *J. Chem. Phys.* **132**, 154104 (2010).
- [90] Vincenzo Barone, Maurizio Casarin, Daniel Forrer, Michele Pavone, Mauro Sambi, and Andrea Vittadini, “Role and effective treatment of dispersive forces in materials: Polyethylene and graphite crystals as test cases,” *J. Comput. Chem.* **30**, 934 (2009).
- [91] P. Blaha, K. Schwarz, G. K. H. Madsen, D. Kvasnicka, and J. Luitz, *WIEN2K, An Augmented Plane Wave + Local Orbitals Program for Calculating Crystal Properties* (Prof. Dr. Karlheinz Schwarz, Vienna University of Technology, Institute of Materials Chemistry, 2001).
- [92] V. I. Anisimov, I. V. Solovyev, M. A. Korotin, M. T. Czyżyk, and G. A. Sawatzky, “Density-functional theory and nio photoemission spectra,” *Phys. Rev. B* **48**, 16929–16934 (1993).
- [93] Y. Baskin and L. Meyer, “Lattice constants of graphite at low temperatures,” *Phys. Rev.* **100**, 544 (1955).
- [94] Yuhao Gu, Qiang Zhang, Congcong Le, Yinxiang Li, Tao Xiang, and Jiangping Hu, “Ni-based transition metal trichalcogenide monolayer: A strongly correlated quadruple-layer graphene,” *Phys. Rev. B* **100**, 165405 (2019).
- [95] AR Wildes, B Roesli, B Lebech, and KW Godfrey, “Spin waves and the critical behaviour of the magnetization in mnpse_3 ,” *Journal of Physics: Condensed Matter* **10**, 6417 (1998).
- [96] Ko Kurosawa, Shozo Saito, and Yasuo Yamaguchi, “Neutron diffraction study on mnpse_3 and fepse_3 ,” *Journal of the Physical Society of Japan* **52**, 3919–3926 (1983).
- [97] D. Lançon, H. C. Walker, E. Ressouche, B. Ouladdiaf, K. C. Rule, G. J. McIntyre, T. J. Hicks, H. M. Rønnow, and A. R. Wildes, “Magnetic structure and magnon dynamics of the quasi-two-dimensional antiferromagnet fepse_3 ,” *Phys. Rev. B* **94**, 214407 (2016).
- [98] Michael A. Susner, Marius Chyasnachyus, Michael A. McGuire, Panchapakesan Ganesh, and Petro Maksymovych, “Metal thio- and selenophosphates as multifunctional van der waals layered materials,” *Advanced Materials* **29**, 1602852 (2017).
- [99] Fengmei Wang, Tofik A. Shifa, Peng Yu, Peng He, Yang Liu, Feng Wang, Zhenxing Wang, Xueying Zhan, Xiaodong Lou, Fan Xia, and Jun He, “New frontiers on van der waals layered metal phosphorous trichalcogenides,” *Advanced Functional Materials* **28**, 1802151 (2018).
- [100] Raymond Brec, “Review on structural and chemical properties of transition metal phosphorous trisulfides mps_3 ,” *Solid State Ionics* **22**, 3 – 30 (1986).
- [101] G. Ouvrard, R. Brec, and J. Rouxel, “Structural determination of some mps_3 layered phases ($m = \text{mn, fe, co, ni}$ and cd),” *Materials Research Bulletin* **20**, 1181 – 1189 (1985).
- [102] Radhika Rani Rao and A.K. Raychaudhuri, “Magnetic studies of a mixed antiferromagnetic system fel-xnixps_3 ,” *Journal of Physics and Chemistry of Solids* **53**, 577 – 583 (1992).
- [103] A R Wildes, V Simonet, E Ressouche, R Ballou, and G J McIntyre, “The magnetic properties and structure of the quasi-two-dimensional antiferromagnet CoPS_3 ,” *Journal of Physics: Condensed Matter* **29**, 455801 (2017).
- [104] Qi Zhang, Kyle Hwangbo, Chong Wang, Qianni Jiang, Jiun-Haw Chu, Haidan Wen, Di Xiao, and Xiaodong

- Xu, “Observation of giant optical linear dichroism in a zigzag antiferromagnet feps3,” *Nano Letters* **21**, 6938–6945 (2021).
- [105] Thomas Olsen, “Magnetic anisotropy and exchange interactions of two-dimensional FePS₃, NiPS₃ and MnPS₃ from first principles calculations,” *Journal of Physics D: Applied Physics* **54**, 314001 (2021).
- [106] V. Grasso and L. Silipigni, “Optical absorption and reflectivity study of the layered mnpse₃ seleniophosphate,” *J. Opt. Soc. Am. B* **16**, 132 (1999).
- [107] Bálint Fülöp, Albin Márffy, Simon Zihlmann, Martin Gmitra, Endre Tóvári, Bálint Szentpéteri, Máté Kedves, Kenji Watanabe, Takashi Taniguchi, Jaroslav Fabian, *et al.*, “Boosting proximity spin-orbit coupling in graphene/wse₂ heterostructures via hydrostatic pressure,” *npj 2D Materials and Applications* **5**, 82 (2021).
- [108] Tobias Frank, Petra Högl, Martin Gmitra, Denis Kochan, and Jaroslav Fabian, “Protected pseudohelical edge states in F_2 -trivial proximitized graphene,” *Phys. Rev. Lett.* **120**, 156402 (2018).
- [109] Klaus Zollner, Aron W. Cummings, Stephan Roche, and Jaroslav Fabian, “Graphene on two-dimensional hexagonal bn, aln, and gan: Electronic, spin-orbit, and spin relaxation properties,” *Phys. Rev. B* **103**, 075129 (2021).
- [110] Klaus Zollner, Martin Gmitra, and Jaroslav Fabian, “Heterostructures of graphene and hBN: Electronic, spin-orbit, and spin relaxation properties from first principles,” *Phys. Rev. B* **99**, 125151 (2019).
- [111] Jiang-Xiazi Lin, Ya-Hui Zhang, Erin Morissette, Zhi Wang, Song Liu, Daniel Rhodes, K. Watanabe, T. Taniguchi, James Hone, and J. I. A. Li, “Spin-orbit driven ferromagnetism at half moire filling in magic-angle twisted bilayer graphene,” *Science* **375**, 437–441 (2022).
- [112] Klaus Zollner, Martin Gmitra, and Jaroslav Fabian, “Swapping exchange and spin-orbit coupling in 2d van der waals heterostructures,” *Phys. Rev. Lett.* **125**, 196402 (2020).
- [113] Klaus Zollner and Jaroslav Fabian, “Bilayer graphene encapsulated within monolayers of ws₂ or cr₂ge₂te₆: Tunable proximity spin-orbit or exchange coupling,” *Phys. Rev. B* **104**, 075126 (2021).
- [114] Klaus Zollner, Martin Gmitra, and Jaroslav Fabian, “Proximity spin-orbit and exchange coupling in aba and abc trilayer graphene van der waals heterostructures,” *Phys. Rev. B* **105**, 115126 (2022).
- [115] Denis Kochan, Susanne Irmer, and Jaroslav Fabian, “Model spin-orbit coupling hamiltonians for graphene systems,” *Phys. Rev. B* **95**, 165415 (2017).
- [116] Võ Tien Phong, Niels R Walet, and Francisco Guinea, “Effective interactions in a graphene layer induced by the proximity to a ferromagnet,” *2D Mater.* **5**, 014004 (2017).
- [117] Klaus Zollner, Martin Gmitra, Tobias Frank, and Jaroslav Fabian, “Theory of proximity-induced exchange coupling in graphene on hbn/(co, ni),” *Phys. Rev. B* **94**, 155441 (2016).
- [118] Matthew Neville, Till Stensitzki, Daniel B. Allen, and Antonino Ingargiola, “LMFIT: Non-Linear Least-Square Minimization and Curve-Fitting for Python,” (2014).
- [119] See Supplemental Material, where we show band structures, density of states, and fit results for the remaining graphene/MPX₃ heterostructures. For the MnPS₃ case we also show the calculated spin polarizations on graphene.
- [120] Vitor M. Pereira, A. H. Castro Neto, and N. M R Peres, “Tight-binding approach to uniaxial strain in graphene,” *Phys. Rev. B* **80**, 045401 (2009).
- [121] B. Wunsch, F. Guinea, and F. Sols, “Dirac-point engineering and topological phase transitions in honeycomb optical lattices,” *New J. Phys.* **10**, 103027 (2008).
- [122] Bálint Fülöp, Albin Márffy, Endre Tóvári, Máté Kedves, Simon Zihlmann, David Indolese, Zoltán Kovács-Krausz, Kenji Watanabe, Takashi Taniguchi, Christian Schönenberger, *et al.*, “New method of transport measurements on van der waals heterostructures under pressure,” *Journal of Applied Physics* **130**, 064303 (2021).
- [123] Gabriella Graziano, Jiří Klimeš, Felix Fernandez-Alonso, and Angelos Michaelides, “Improved description of soft layered materials with van der waals density functional theory,” *Journal of Physics: Condensed Matter* **24**, 424216 (2012).
- [124] M. Gmitra, S. Konschuh, C. Ertler, C. Ambrosch-Draxl, and J. Fabian, “Band-structure topologies of graphene: Spin-orbit coupling effects from first principles,” *Phys. Rev. B* **80**, 235431 (2009).
- [125] Sergej Konschuh, Martin Gmitra, and Jaroslav Fabian, “Tight-binding theory of the spin-orbit coupling in graphene,” *Phys. Rev. B* **82**, 245412 (2010).
- [126] Klaus Zollner and Jaroslav Fabian, “Single and bilayer graphene on the topological insulator bi₂se₃: Electronic and spin-orbit properties from first principles,” *Phys. Rev. B* **100**, 165141 (2019).

Supplemental Material: Proximity effects in graphene on monolayers of transition-metal phosphorus trichalcogenides MPX_3

Klaus Zollner^{1,*} and Jaroslav Fabian¹

¹*Institute for Theoretical Physics, University of Regensburg, 93040 Regensburg, Germany*

In the Supplemental Material we show the band structures, density of states, and fit results for the remaining heterostructures not shown in the main text. More specifically we show additional results for graphene on $MnPS_3$, $NiPS_3$, $FePS_3$, $CoPS_3$, $MnPSe_3$, $NiPSe_3$, $FePSe_3$, and $CoPSe_3$, where each MPX_3 monolayer can be in the ferromagnetic, the antiferromagnetic Néel, the antiferromagnetic zigzag, and the antiferromagnetic stripy phase.

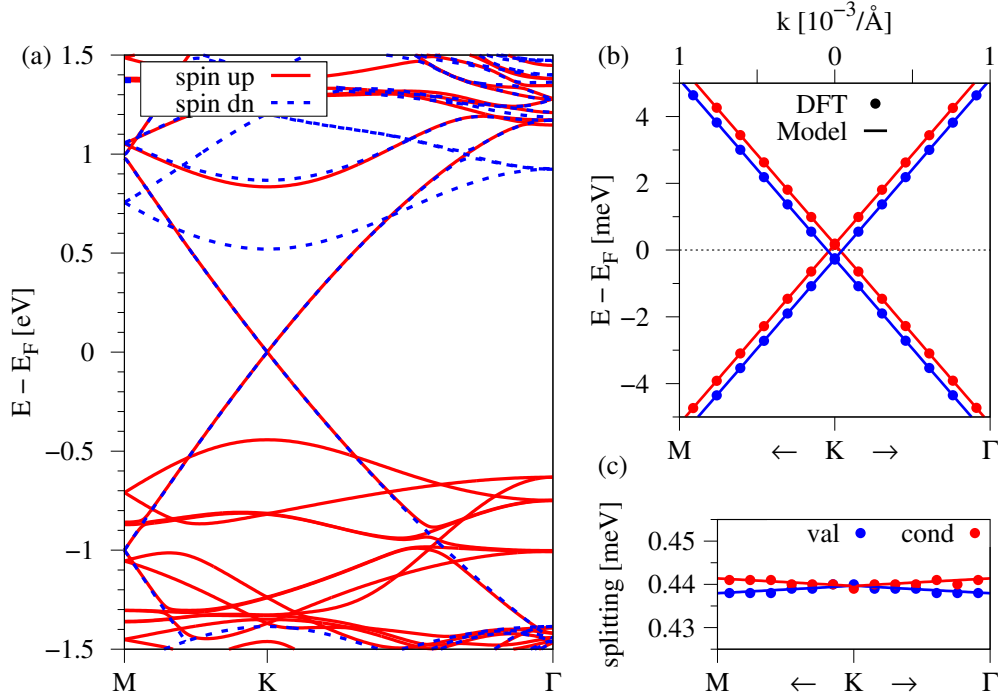


FIG. S1. (a) DFT-calculated band structure of the **graphene/ $MnPSe_3$** heterostructure along the high-symmetry path M-K- Γ without SOC, when the $MnPSe_3$ is in the **ferromagnetic phase**. Red solid (blue dashed) lines correspond to spin up (spin down). (b) Zoom to the DFT-calculated (symbols) low energy Dirac bands near the K point with a fit to the model Hamiltonian (solid line). (c) The splitting of valence and conduction band.

* klaus.zollner@physik.uni-regensburg.de

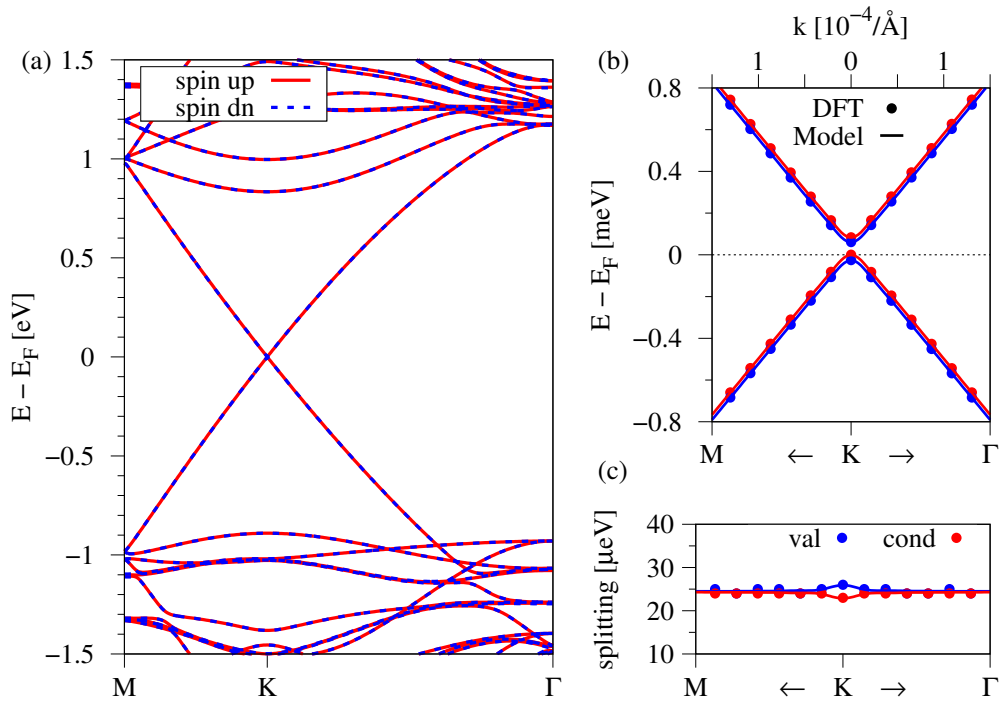


FIG. S2. (a) DFT-calculated band structure of the [graphene/MnPSe₃](#) heterostructure along the high-symmetry path M-K- Γ without SOC, when the MnPSe₃ is in the [antiferromagnetic Néel phase](#). Red solid (blue dashed) lines correspond to spin up (spin down). (b) Zoom to the DFT-calculated (symbols) low energy Dirac bands near the K point with a fit to the model Hamiltonian (solid line). (c) The splitting of valence and conduction band.

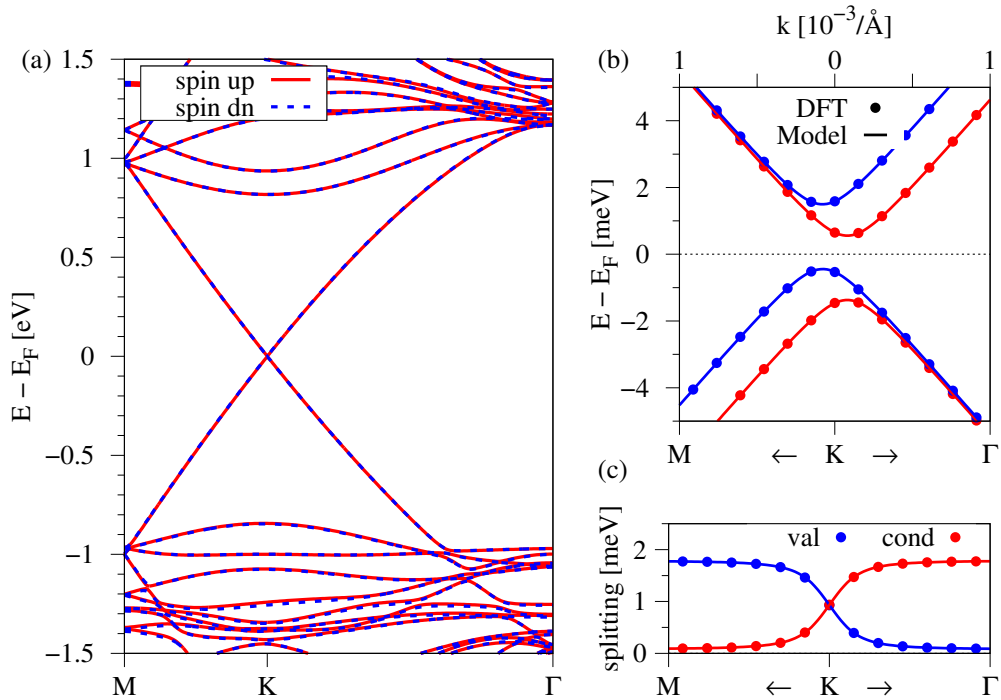


FIG. S3. (a) DFT-calculated band structure of the [graphene/MnPSe₃](#) heterostructure along the high-symmetry path M-K- Γ without SOC, when the MnPSe₃ is in the [antiferromagnetic zigzag phase](#). Red solid (blue dashed) lines correspond to spin up (spin down). (b) Zoom to the DFT-calculated (symbols) low energy Dirac bands near the K point with a fit to the model Hamiltonian (solid line). (c) The splitting of valence and conduction band.

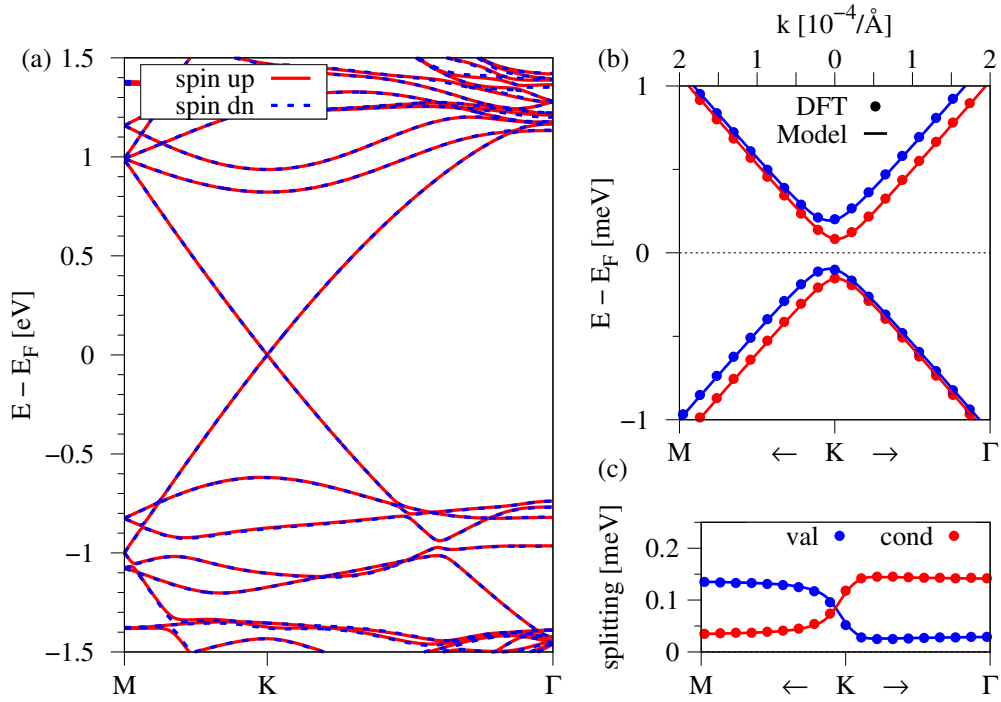


FIG. S4. (a) DFT-calculated band structure of the **graphene/MnPSe₃** heterostructure along the high-symmetry path M-K- Γ without SOC, when the MnPSe₃ is in the **antiferromagnetic stripy phase**. Red solid (blue dashed) lines correspond to spin up (spin down). (b) Zoom to the DFT-calculated (symbols) low energy Dirac bands near the K point with a fit to the model Hamiltonian (solid line). (c) The splitting of valence and conduction band.

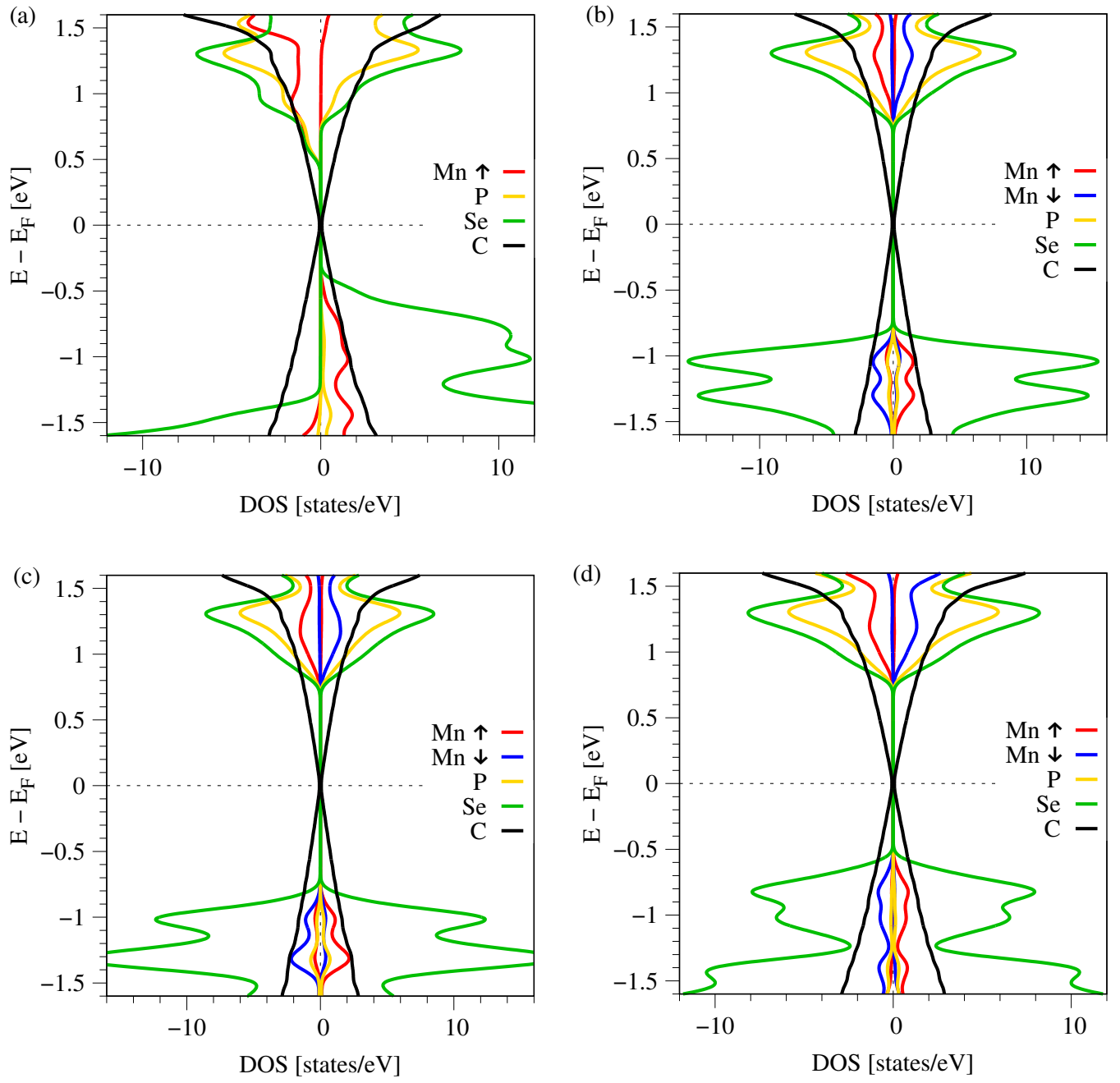


FIG. S5. Spin and atom resolved Density of States (DOS) for graphene on MnPSe_3 when MnPSe_3 is in the (a) ferromagnetic, (b) antiferromagnetic Néel, (c) antiferromagnetic zigzag, or (d) antiferromagnetic stripy phase.

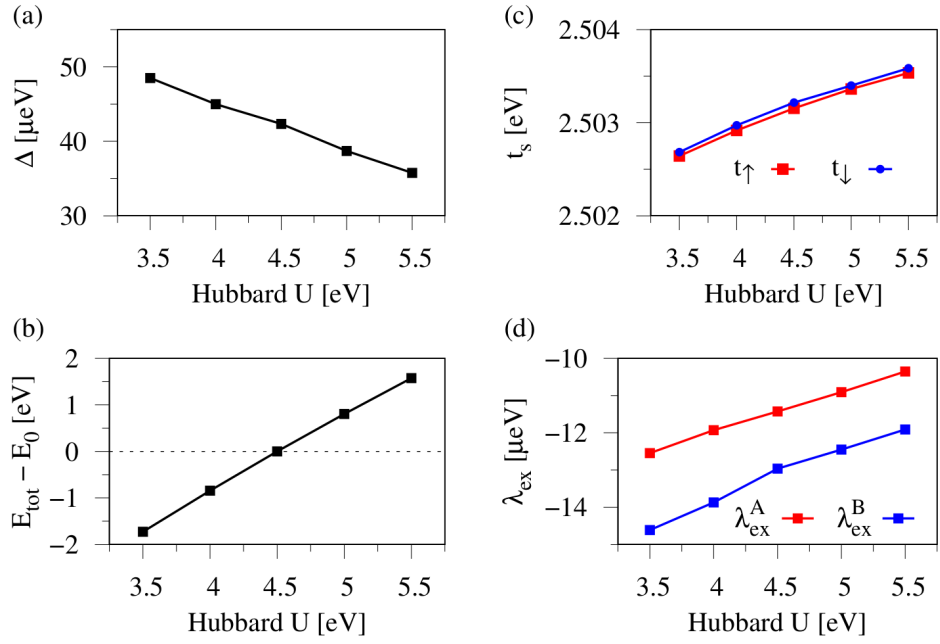


FIG. S6. Hubbard U dependence of (a) the staggered potential Δ , (b) the total energy E_{tot} , (c) the spin dependent hopping parameters t_{\uparrow} and t_{\downarrow} , and (d) the sublattice resolved proximity exchange parameters λ_{ex}^A and λ_{ex}^B for the **graphene/MnPSe₃** heterostructure when the MnPSe₃ is in the **antiferromagnetic Néel phase**.

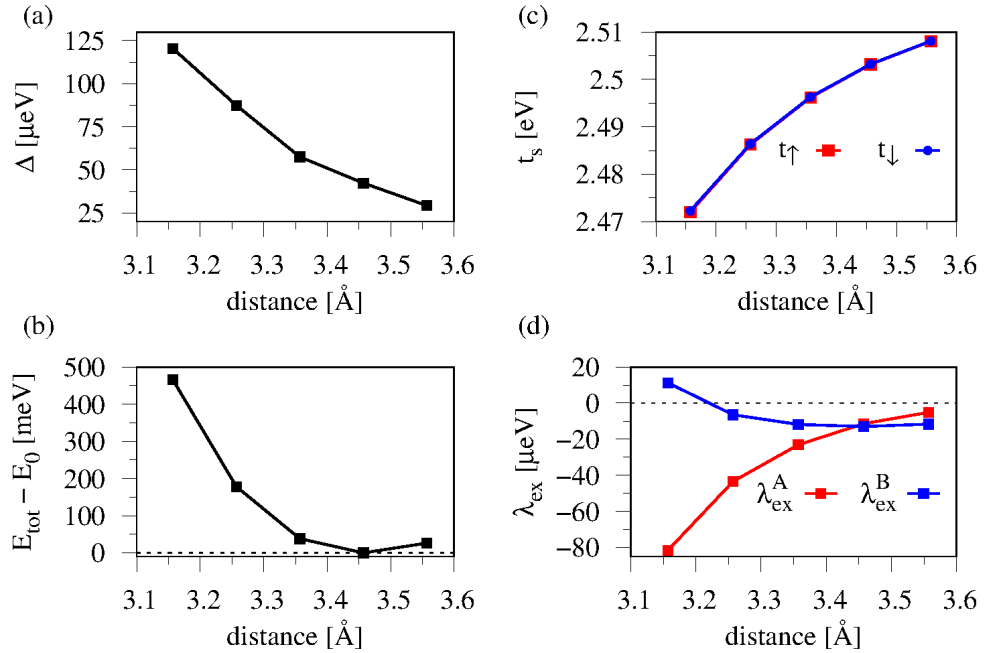


FIG. S7. Interlayer distance dependence of (a) the staggered potential Δ , (b) the total energy E_{tot} , (c) the spin dependent hopping parameters t_{\uparrow} and t_{\downarrow} , and (d) the sublattice resolved proximity exchange parameters λ_{ex}^A and λ_{ex}^B for the **graphene/MnPSe₃** heterostructure when the MnPSe₃ is in the **antiferromagnetic Néel phase**.

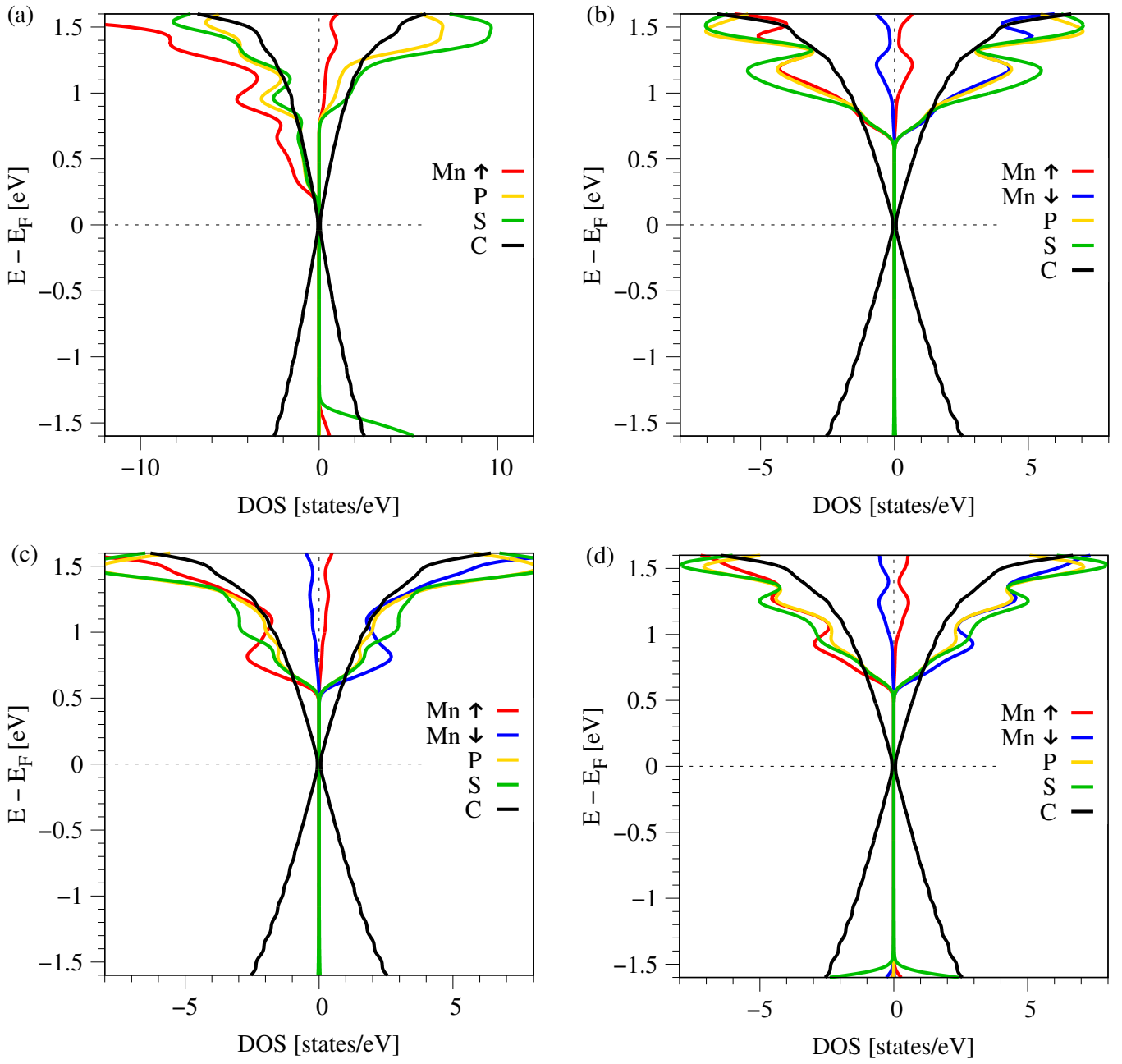


FIG. S8. Spin and atom resolved Density of States (DOS) for graphene on MnPS₃ when MnPS₃ is in the (a) ferromagnetic, (b) antiferromagnetic Néel, (c) antiferromagnetic zigzag, or (d) antiferromagnetic stripy phase.

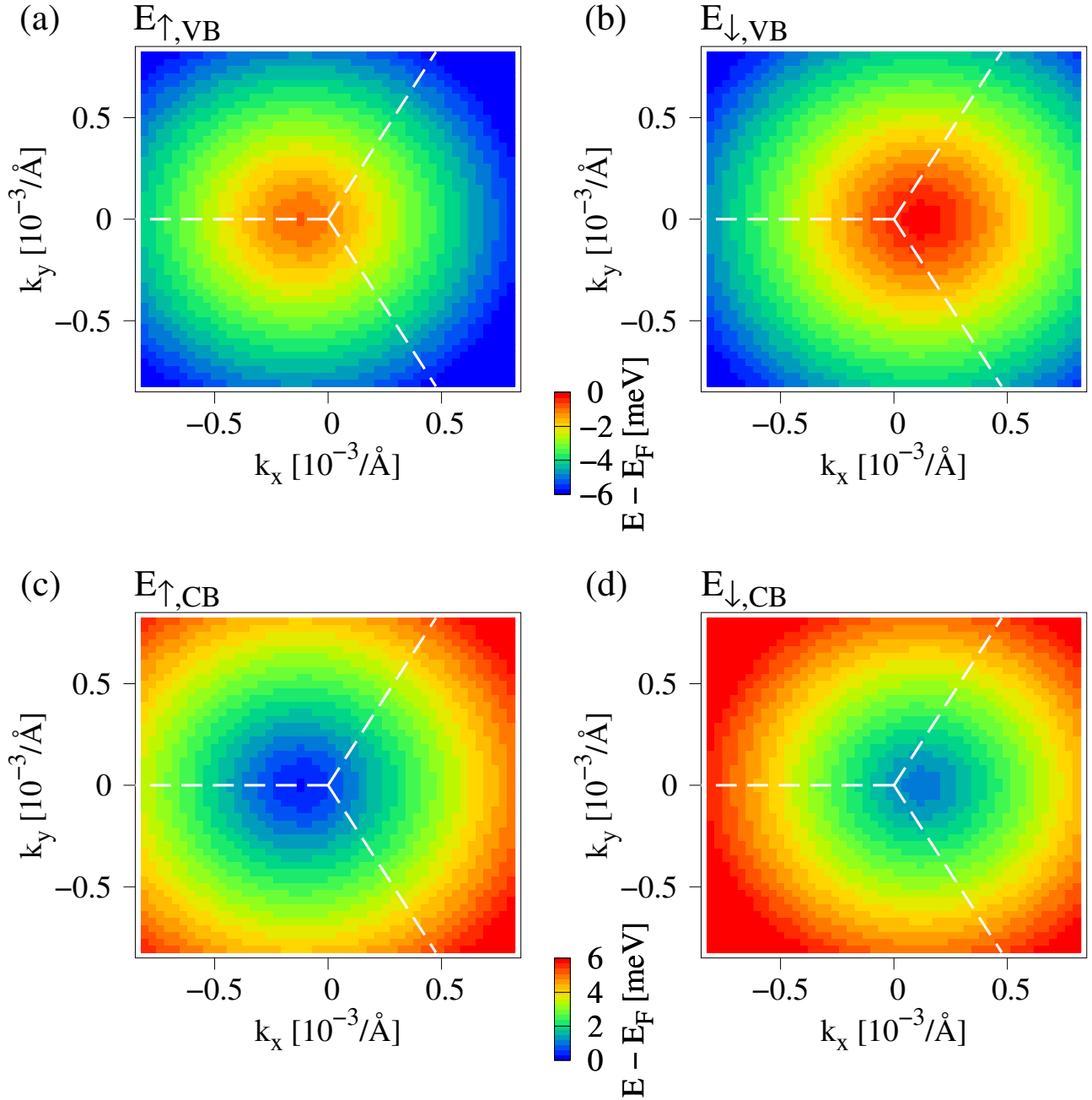


FIG. S9. 2D-map of the DFT-calculated low energy Dirac bands of the **graphene/MnPS₃** heterostructure without SOC, when the MnPS₃ is in the **antiferromagnetic zigzag phase**. (a,b) The valence band energies for spin up $E_{\uparrow,VB}$ and down $E_{\downarrow,VB}$. (c,d) Same as (a,b) but for the conduction band. The dashed white lines mark the edges of the Brillouin zone with the K point at the center.

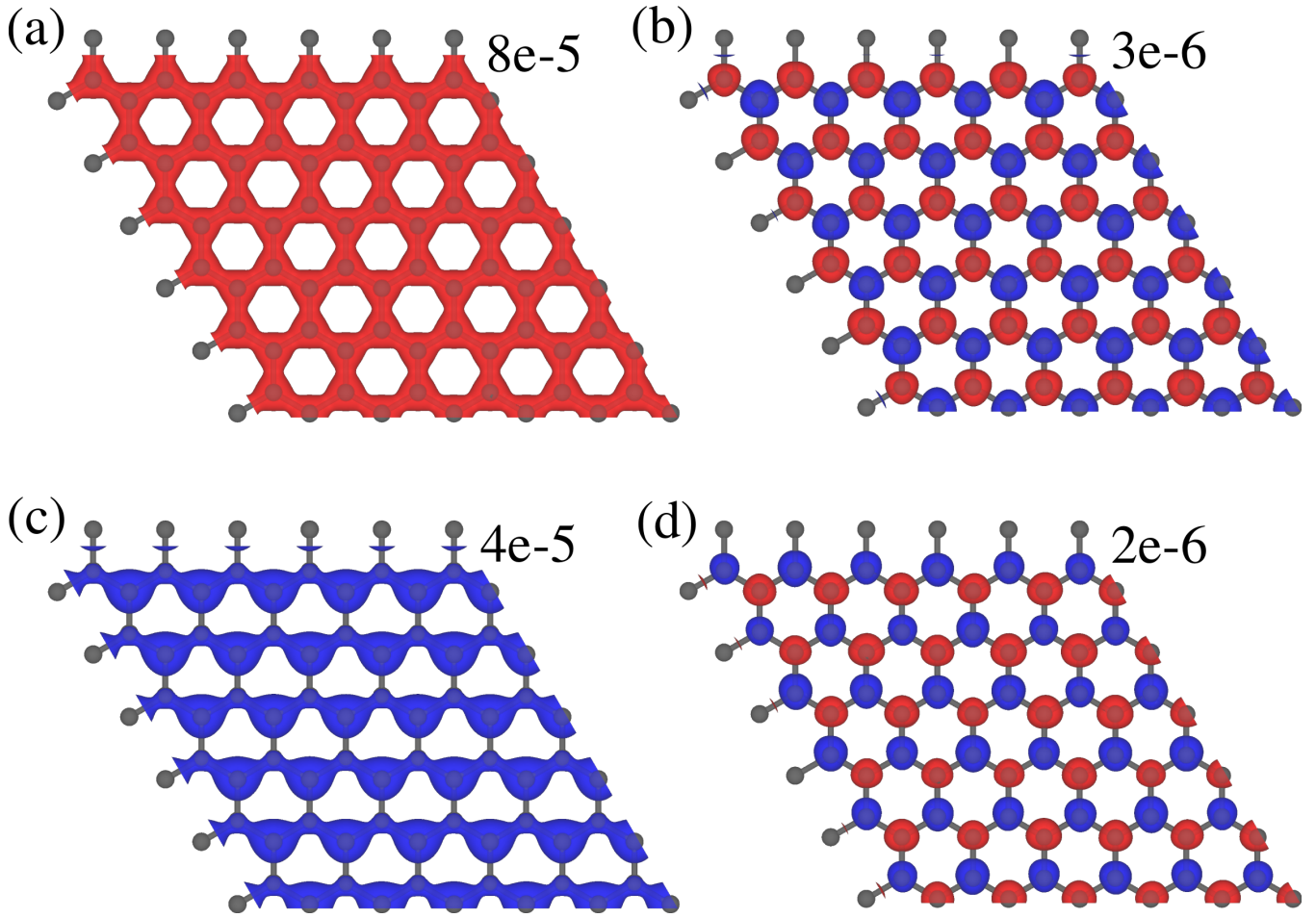


FIG. S10. Calculated spin polarizations, $\Delta\rho = \rho_{\uparrow} - \rho_{\downarrow}$, for **graphene on MnPS₃** when MnPS₃ is in the (a) ferromagnetic, (b) antiferromagnetic Néel, (c) antiferromagnetic zigzag, or (d) antiferromagnetic stripy phase. For better visualization of the spin polarizations on graphene, we have deleted the MnPS₃ substrate in the figures. The spin densities $\rho_{\uparrow/\downarrow}(\mathbf{r}) = \sum_{n,\mathbf{k}} |\phi_{n,\uparrow/\downarrow}^{\mathbf{k}}(\mathbf{r})|^2$ are sums over eigenstates with the corresponding spin. Here, we take into account Dirac states in the energy window of -6 to -4 meV below the Fermi level. The color red (blue) corresponds to $\Delta\rho > 0$ ($\Delta\rho < 0$). The isosurfaces correspond to isovalues, in units \AA^{-3} , as indicated next to each subfigure.

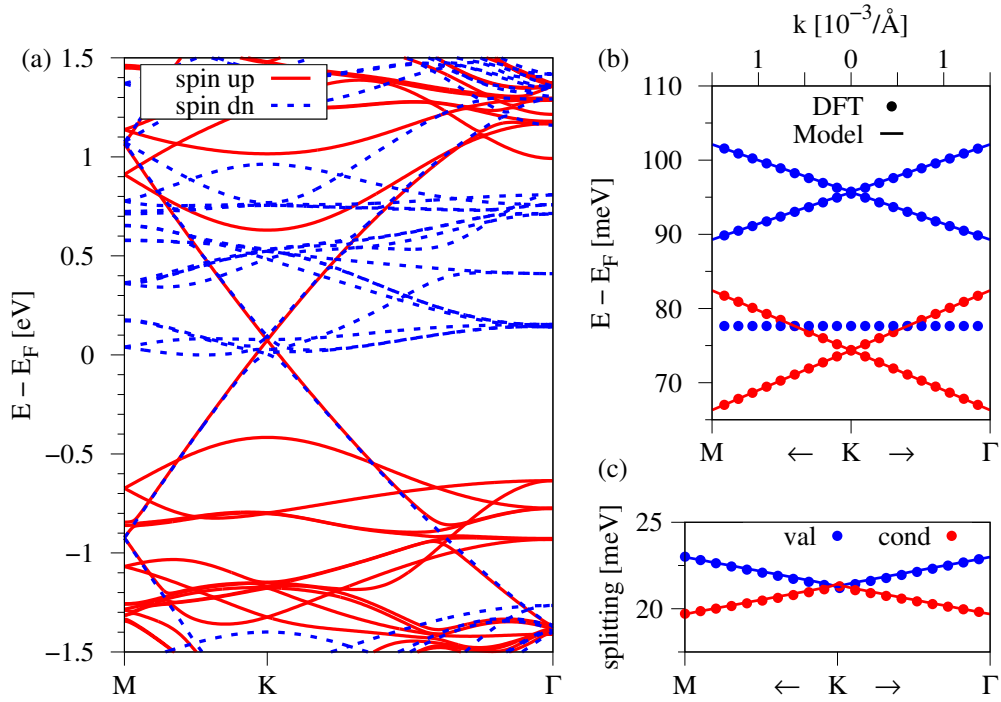


FIG. S11. (a) DFT-calculated band structure of the **graphene/NiPSe₃** heterostructure along the high-symmetry path M-K- Γ without SOC, when the NiPSe₃ is in the **ferromagnetic phase**. Red solid (blue dashed) lines correspond to spin up (spin down). (b) Zoom to the DFT-calculated (symbols) low energy Dirac bands near the K point with a fit to the model Hamiltonian (solid line). (c) The splitting of valence and conduction band.

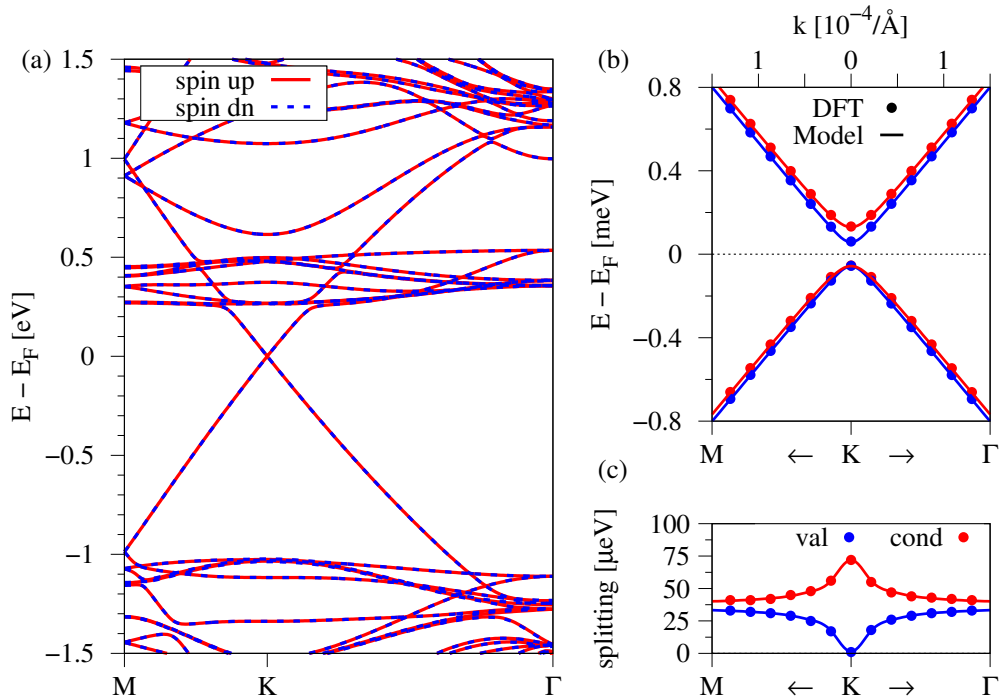


FIG. S12. (a) DFT-calculated band structure of the **graphene/NiPSe₃** heterostructure along the high-symmetry path M-K- Γ without SOC, when the NiPSe₃ is in the **antiferromagnetic Néel phase**. Red solid (blue dashed) lines correspond to spin up (spin down). (b) Zoom to the DFT-calculated (symbols) low energy Dirac bands near the K point with a fit to the model Hamiltonian (solid line). (c) The splitting of valence and conduction band.

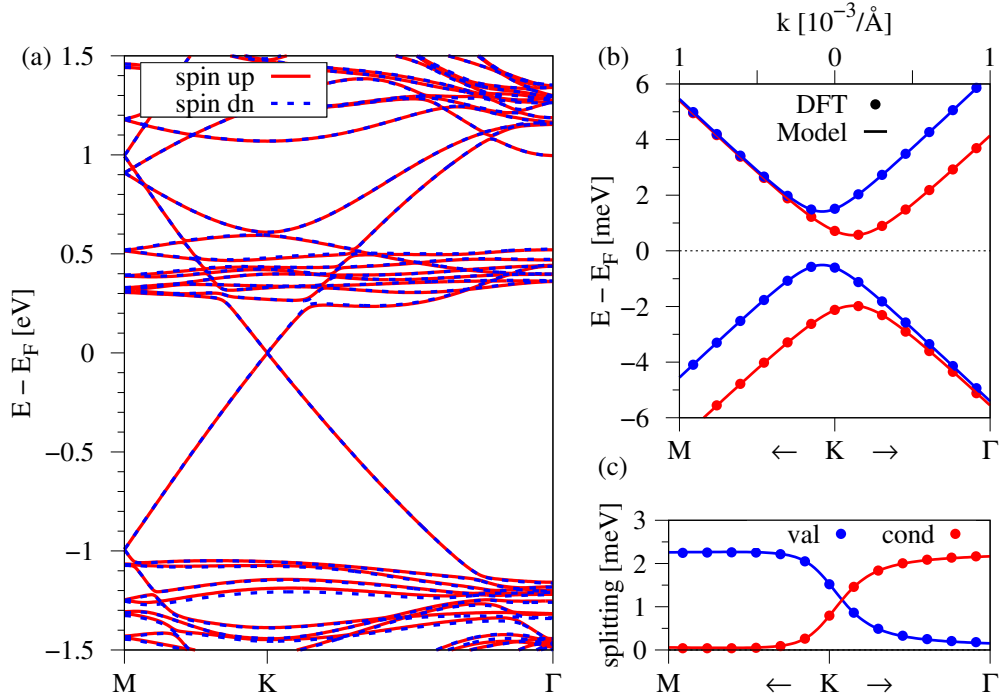


FIG. S13. (a) DFT-calculated band structure of the [graphene/NiPSe₃](#) heterostructure along the high-symmetry path M-K- Γ without SOC, when the NiPSe₃ is in the [antiferromagnetic zigzag phase](#). Red solid (blue dashed) lines correspond to spin up (spin down). (b) Zoom to the DFT-calculated (symbols) low energy Dirac bands near the K point with a fit to the model Hamiltonian (solid line). (c) The splitting of valence and conduction band.

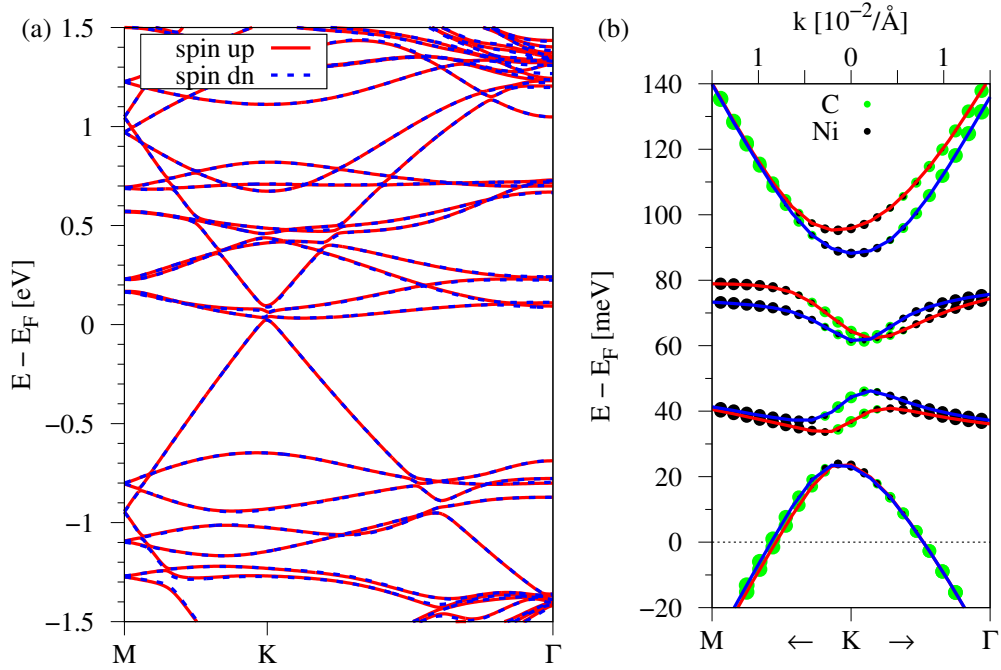


FIG. S14. (a) DFT-calculated band structure of the [graphene/NiPSe₃](#) heterostructure along the high-symmetry path M-K- Γ without SOC, when the NiPSe₃ is in the [antiferromagnetic stripy phase](#). Red solid (blue dashed) lines correspond to spin up (spin down). (b) Zoom to the DFT-calculated low energy Dirac bands near the K point (red and blue solid lines for spin up and down). The green and black spheres represent the projections onto C and Ni states. This emphasizes that the graphene Dirac states are strongly hybridized with Ni states from the NiPSe₃ and we cannot apply our model fit properly.

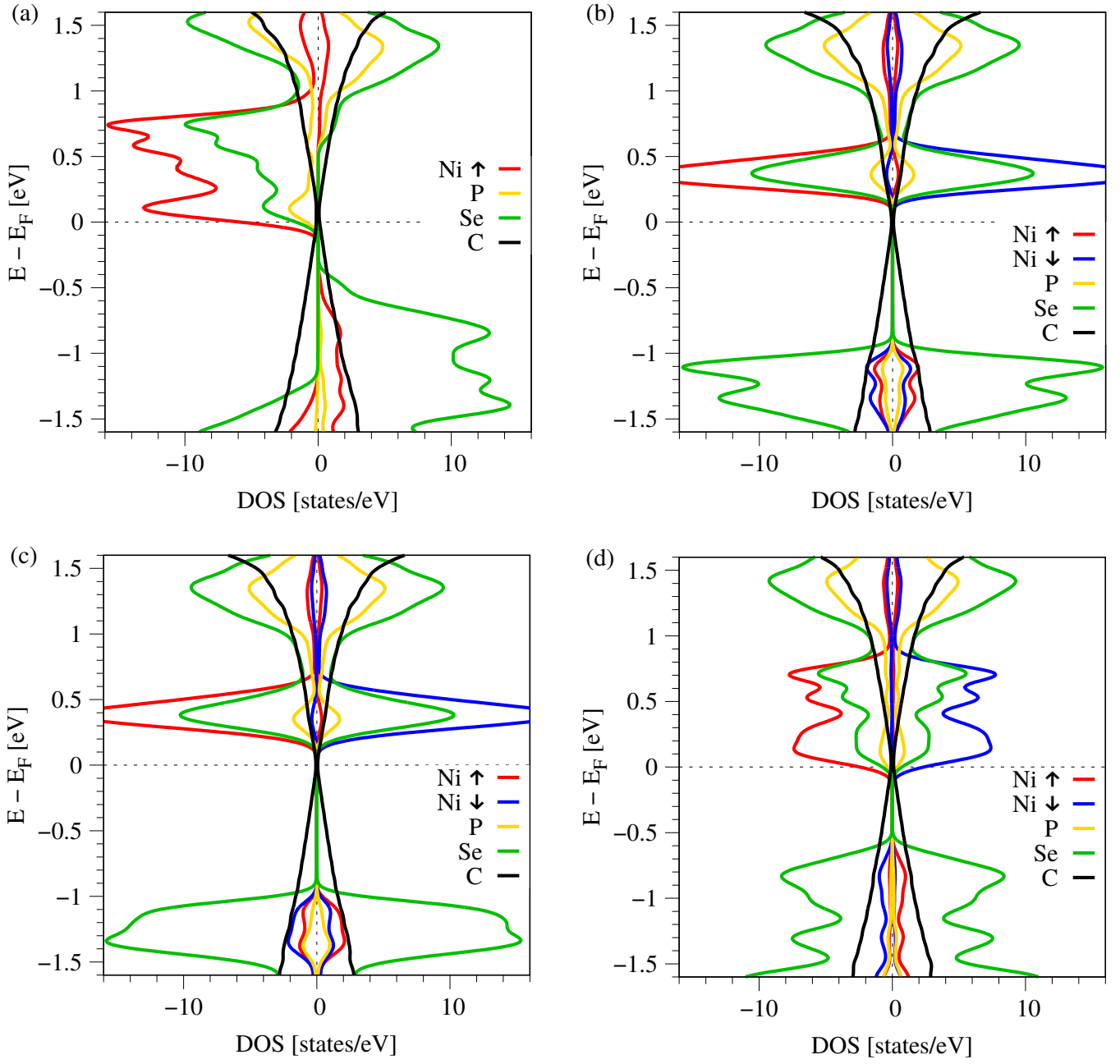


FIG. S15. Spin and atom resolved Density of States (DOS) for graphene on NiPSe₃ when NiPSe₃ is in the (a) ferromagnetic, (b) antiferromagnetic Néel, (c) antiferromagnetic zigzag, or (d) antiferromagnetic stripy phase.

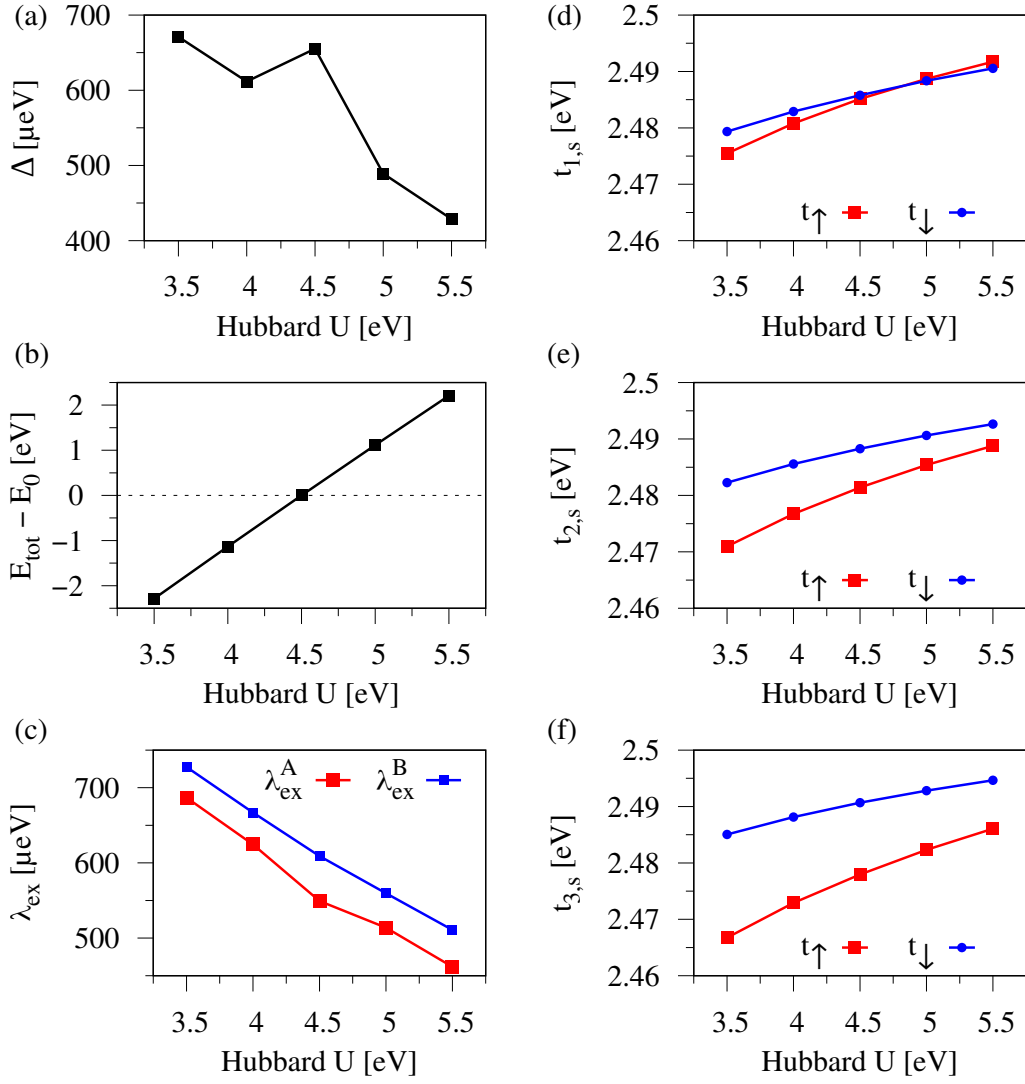


FIG. S16. Hubbard U dependence of (a) the staggered potential Δ , (b) the total energy E_{tot} , (c) the sublattice resolved proximity exchange parameters λ_{ex}^A and λ_{ex}^B , and (d-f) the spin and direction dependent hopping parameters $t_{\alpha,\uparrow}$ and $t_{\alpha,\downarrow}$, for the graphene/NiPSe₃ heterostructure when the NiPSe₃ is in the antiferromagnetic zigzag phase.

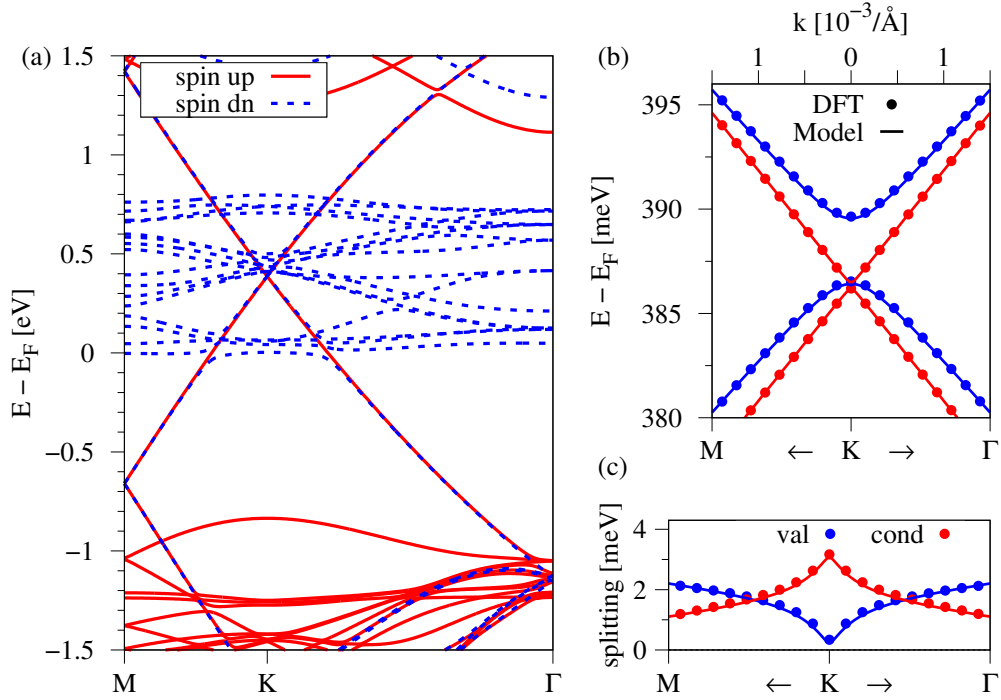


FIG. S17. (a) DFT-calculated band structure of the **graphene/NiPS₃** heterostructure along the high-symmetry path M-K- Γ without SOC, when the NiPS₃ is in the **ferromagnetic phase**. Red solid (blue dashed) lines correspond to spin up (spin down). (b) Zoom to the DFT-calculated (symbols) low energy Dirac bands near the K point with a fit to the model Hamiltonian (solid line). (c) The splitting of valence and conduction band.

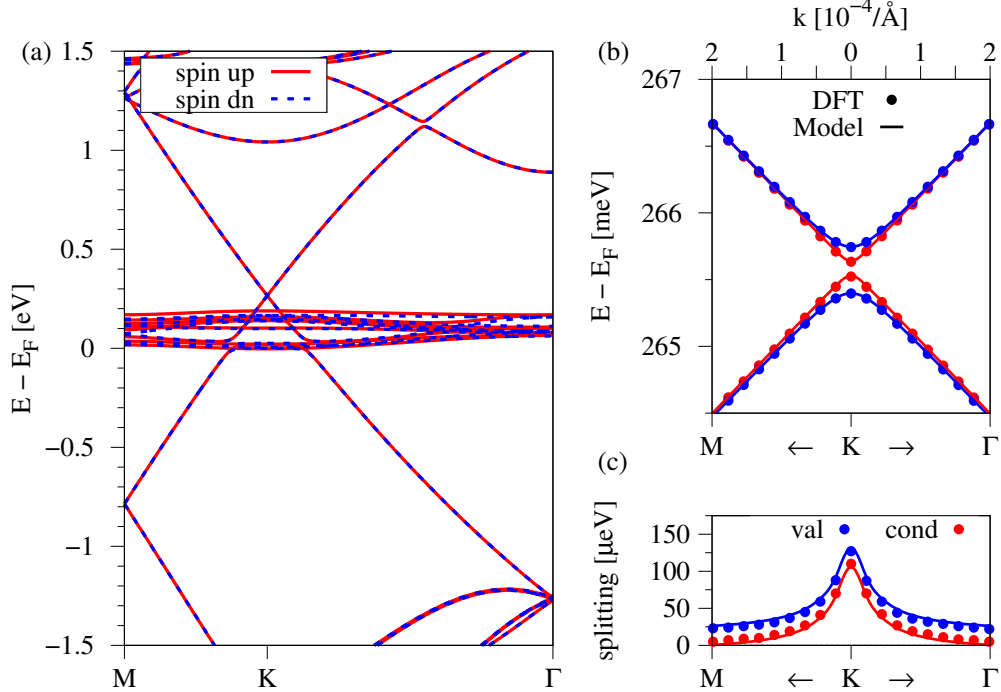


FIG. S18. (a) DFT-calculated band structure of the **graphene/NiPS₃** heterostructure along the high-symmetry path M-K- Γ without SOC, when the NiPS₃ is in the **antiferromagnetic Néel phase**. Red solid (blue dashed) lines correspond to spin up (spin down). (b) Zoom to the DFT-calculated (symbols) low energy Dirac bands near the K point with a fit to the model Hamiltonian (solid line). (c) The splitting of valence and conduction band.

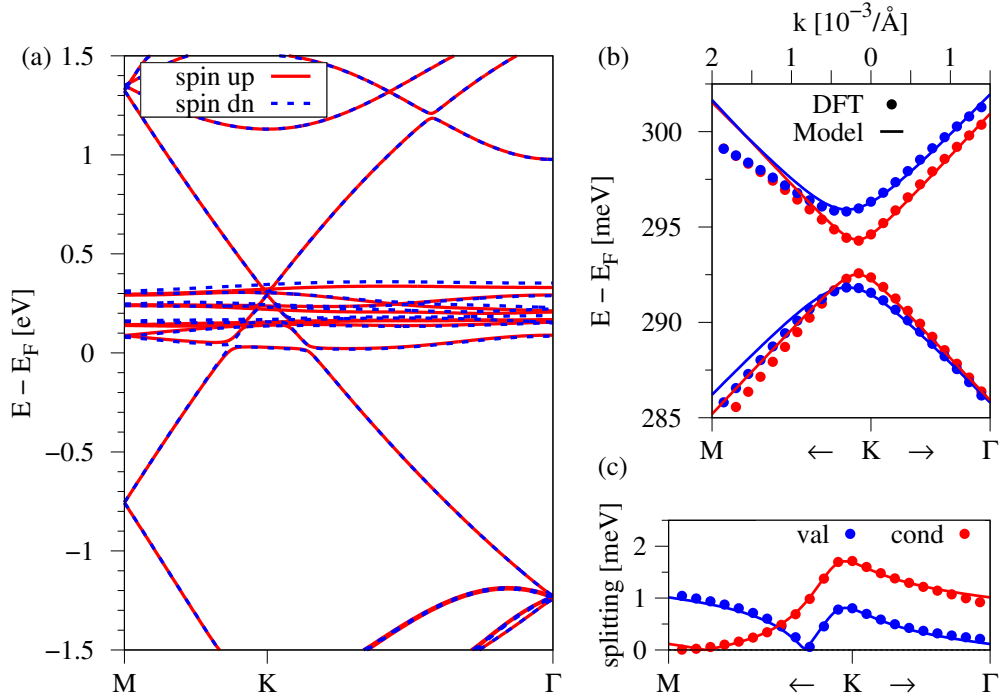


FIG. S19. (a) DFT-calculated band structure of the **graphene/NiPS₃** heterostructure along the high-symmetry path M-K- Γ without SOC, when the NiPS₃ is in the **antiferromagnetic zigzag phase**. Red solid (blue dashed) lines correspond to spin up (spin down). (b) Zoom to the DFT-calculated (symbols) low energy Dirac bands near the K point with a fit to the model Hamiltonian (solid line). (c) The splitting of valence and conduction band.

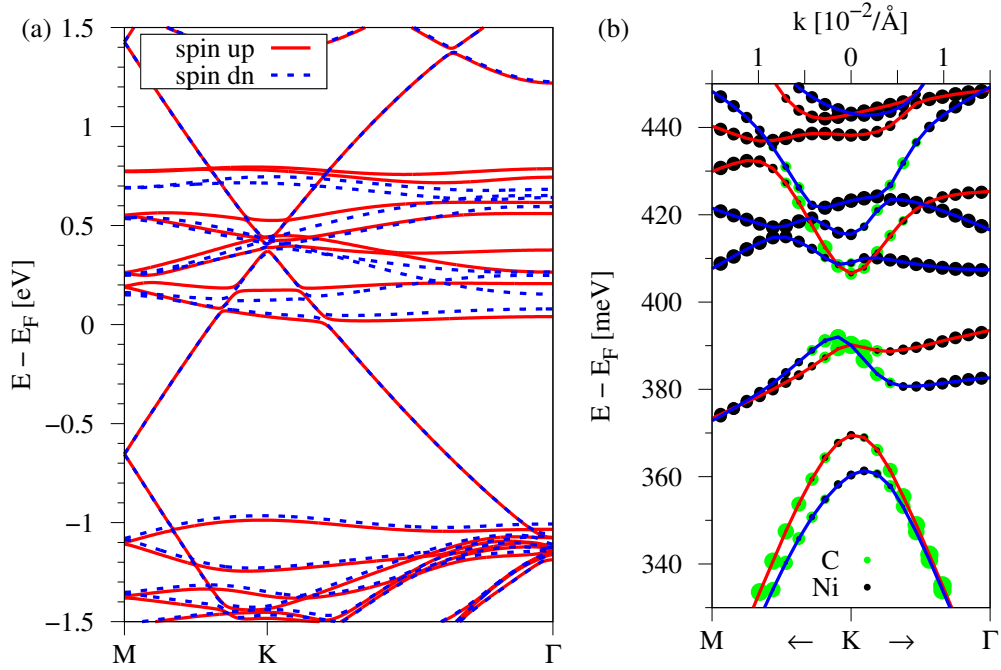


FIG. S20. (a) DFT-calculated band structure of the **graphene/NiPS₃** heterostructure along the high-symmetry path M-K- Γ without SOC, when the NiPS₃ is in the **antiferromagnetic stripy phase**. Red solid (blue dashed) lines correspond to spin up (spin down). (b) Zoom to the DFT-calculated low energy Dirac bands near the K point (red and blue solid lines for spin up and down). The green and black spheres represent the projections onto C and Ni states. This emphasizes that the graphene Dirac states are strongly hybridized with Ni states from the NiPS₃ and we cannot apply our model fit properly.

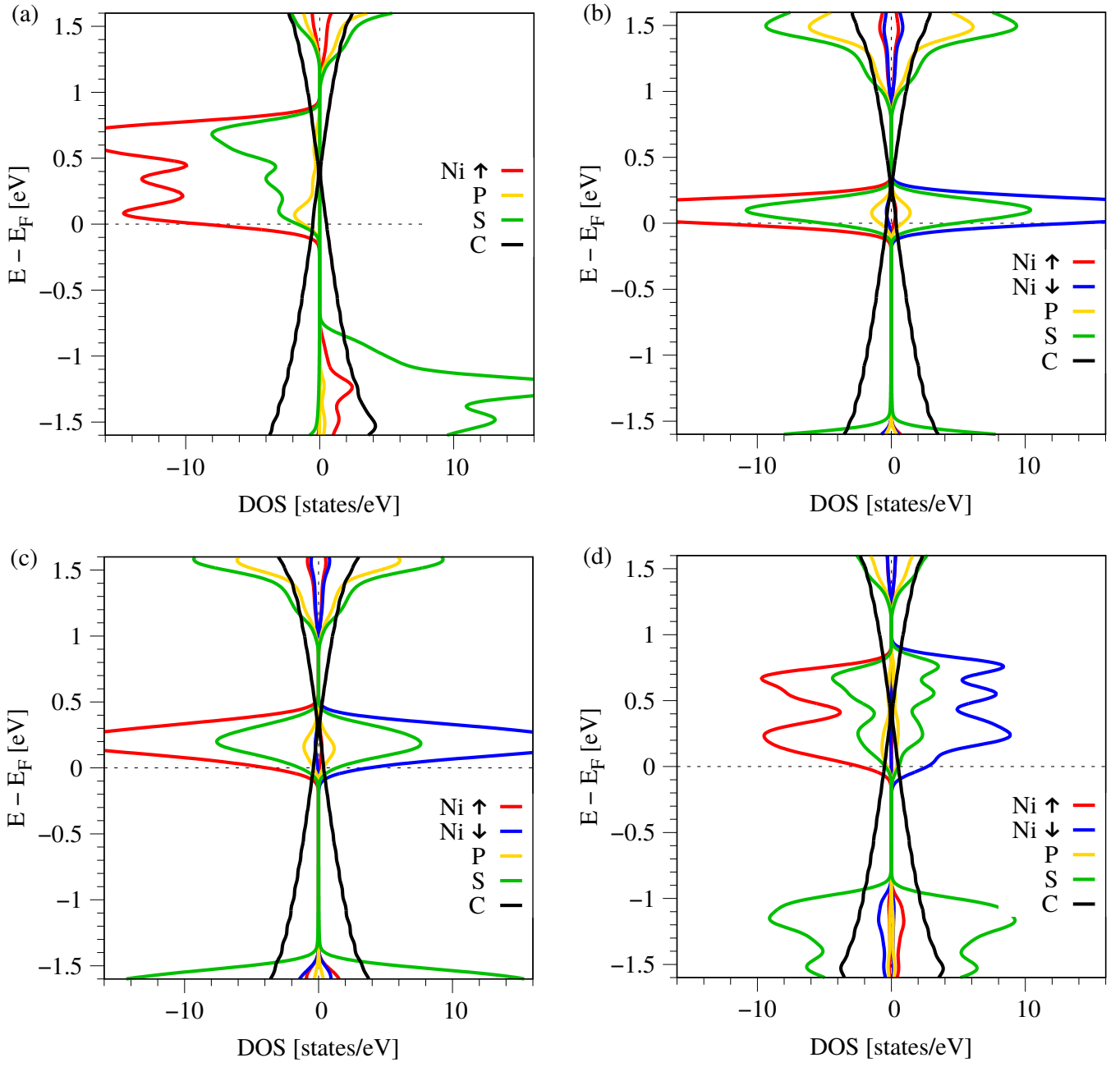


FIG. S21. Spin and atom resolved Density of States (DOS) for graphene on NiPS₃ when NiPS₃ is in the (a) ferromagnetic, (b) antiferromagnetic Néel, (c) antiferromagnetic zigzag, or (d) antiferromagnetic stripy phase.

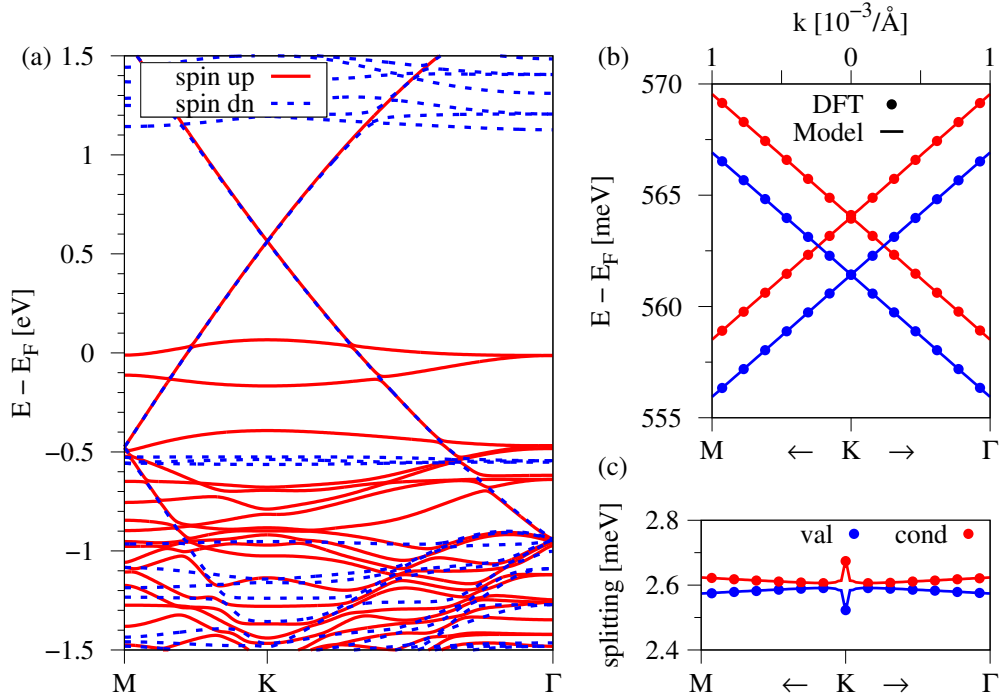


FIG. S22. (a) DFT-calculated band structure of the **graphene/CoPS₃** heterostructure along the high-symmetry path M-K- Γ without SOC, when the CoPS₃ is in the **ferromagnetic phase**. Red solid (blue dashed) lines correspond to spin up (spin down). (b) Zoom to the DFT-calculated (symbols) low energy Dirac bands near the K point with a fit to the model Hamiltonian (solid line). (c) The splitting of valence and conduction band.

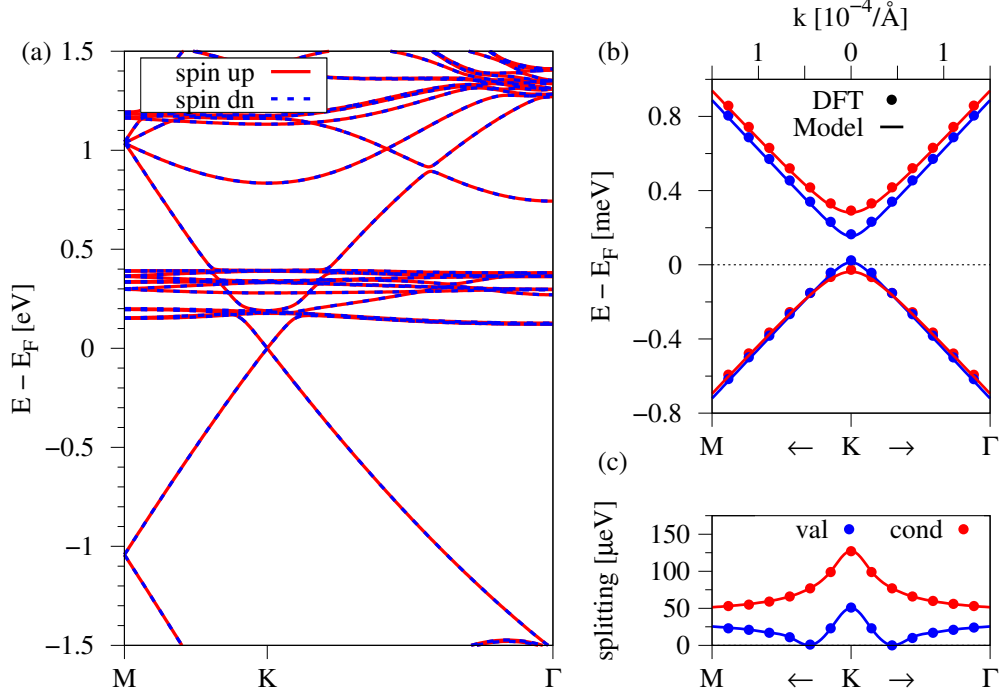


FIG. S23. (a) DFT-calculated band structure of the **graphene/CoPS₃** heterostructure along the high-symmetry path M-K- Γ without SOC, when the CoPS₃ is in the **antiferromagnetic Néel phase**. Red solid (blue dashed) lines correspond to spin up (spin down). (b) Zoom to the DFT-calculated (symbols) low energy Dirac bands near the K point with a fit to the model Hamiltonian (solid line). (c) The splitting of valence and conduction band.

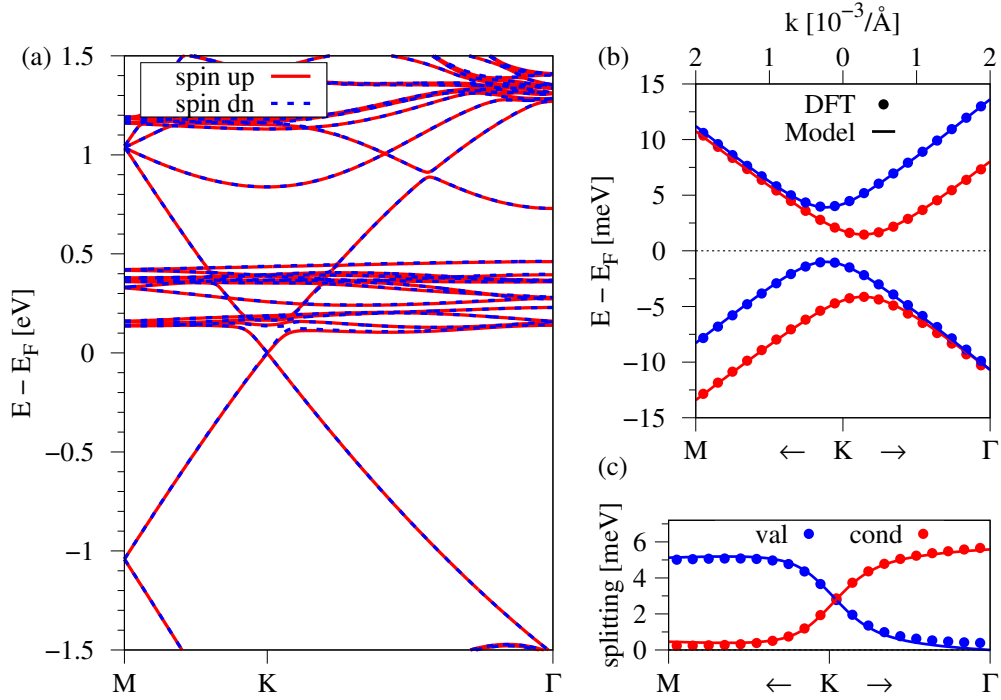


FIG. S24. (a) DFT-calculated band structure of the **graphene/CoPS₃** heterostructure along the high-symmetry path M-K- Γ without SOC, when the CoPS₃ is in the **antiferromagnetic zigzag phase**. Red solid (blue dashed) lines correspond to spin up (spin down). (b) Zoom to the DFT-calculated (symbols) low energy Dirac bands near the K point with a fit to the model Hamiltonian (solid line). (c) The splitting of valence and conduction band.

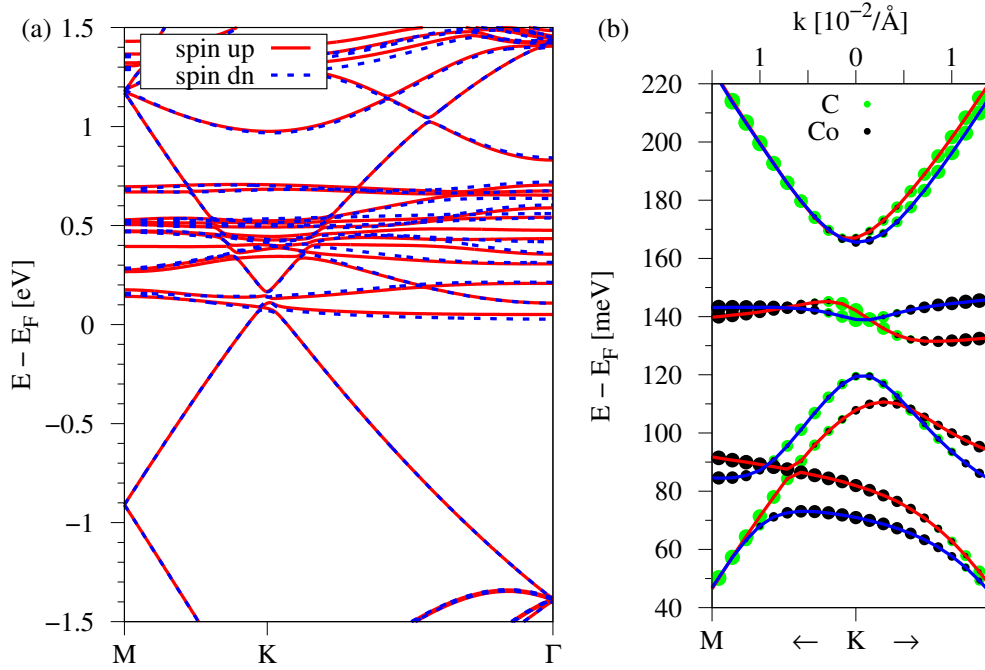


FIG. S25. (a) DFT-calculated band structure of the **graphene/CoPS₃** heterostructure along the high-symmetry path M-K- Γ without SOC, when the CoPS₃ is in the **antiferromagnetic stripy phase**. Red solid (blue dashed) lines correspond to spin up (spin down). (b) Zoom to the DFT-calculated low energy Dirac bands near the K point (red and blue solid lines for spin up and down). The green and black spheres represent the projections onto C and Co states. This emphasizes that the graphene Dirac states are strongly hybridized with Co states from the CoPS₃ and we cannot apply our model fit properly.

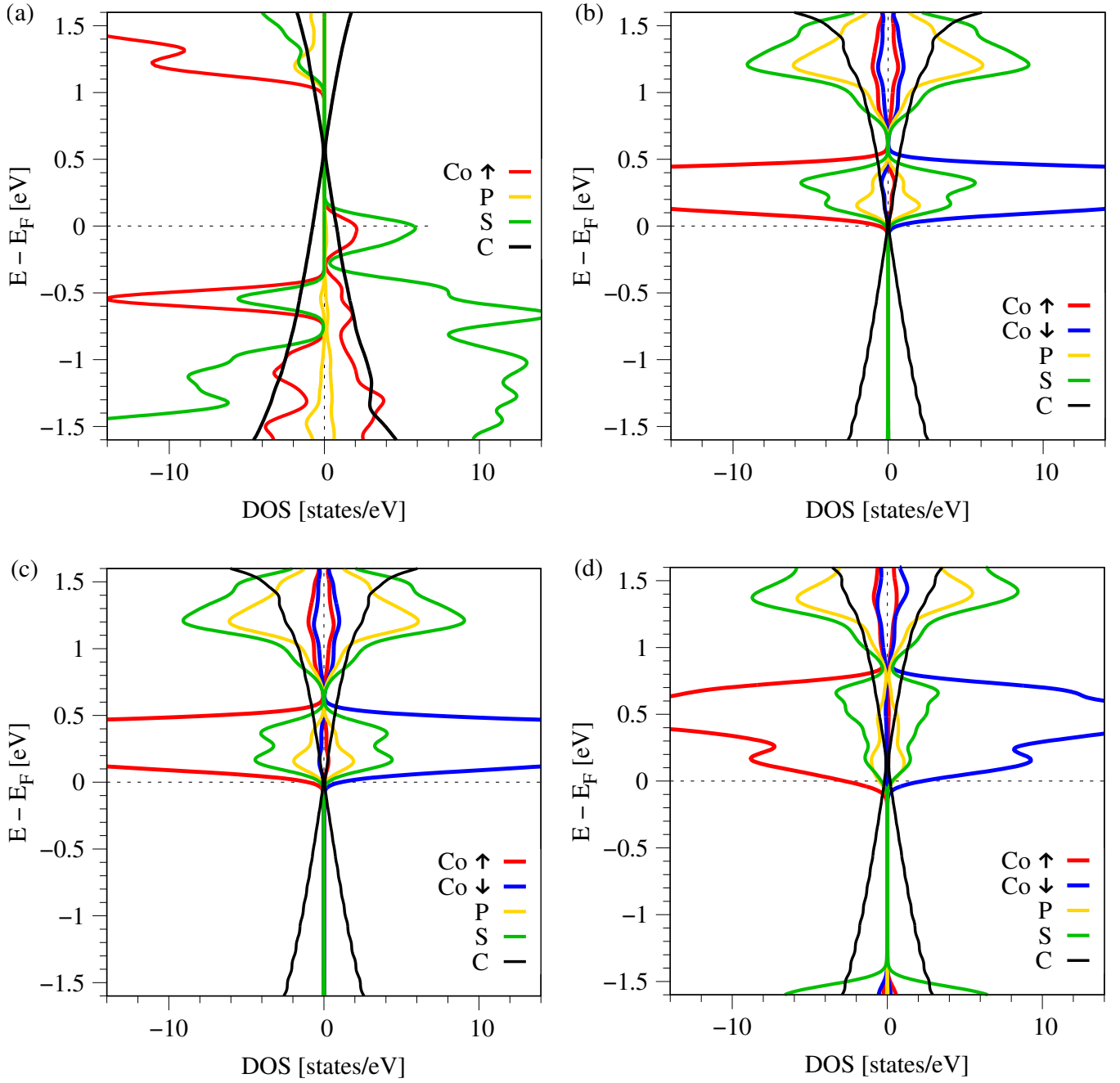


FIG. S26. Spin and atom resolved Density of States (DOS) for graphene on CoPS₃ when CoPS₃ is in the (a) ferromagnetic, (b) antiferromagnetic Néel, (c) antiferromagnetic zigzag, or (d) antiferromagnetic stripy phase.

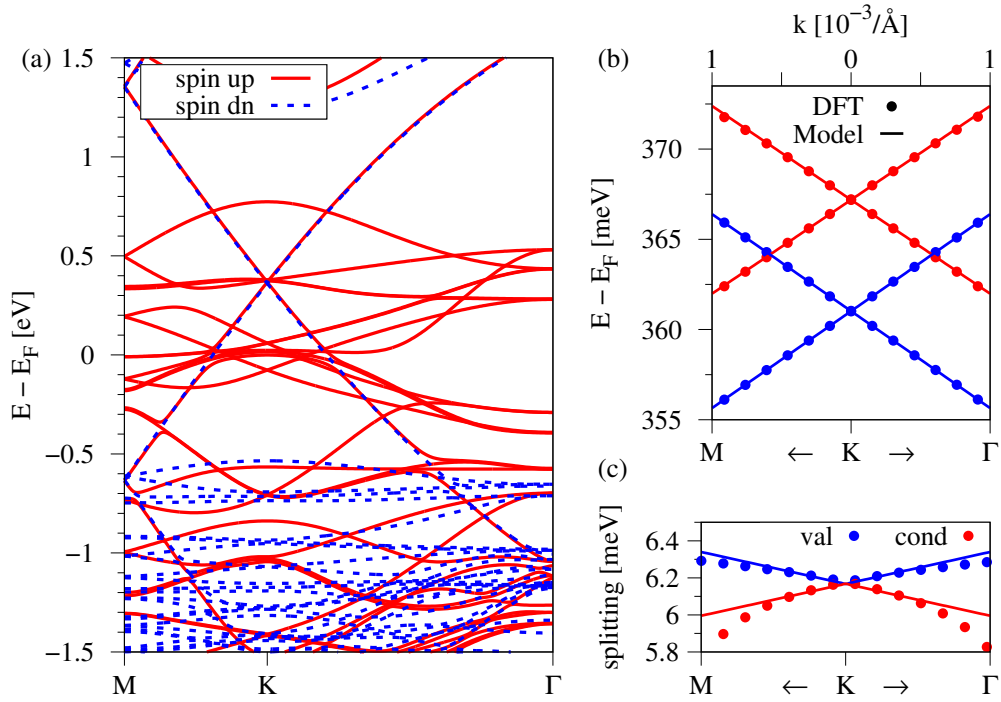


FIG. S27. (a) DFT-calculated band structure of the **graphene/CoPSe₃** heterostructure along the high-symmetry path M-K- Γ without SOC, when the CoPSe₃ is in the **ferromagnetic phase**. Red solid (blue dashed) lines correspond to spin up (spin down). (b) Zoom to the DFT-calculated (symbols) low energy Dirac bands near the K point with a fit to the model Hamiltonian (solid line). (c) The splitting of valence and conduction band.

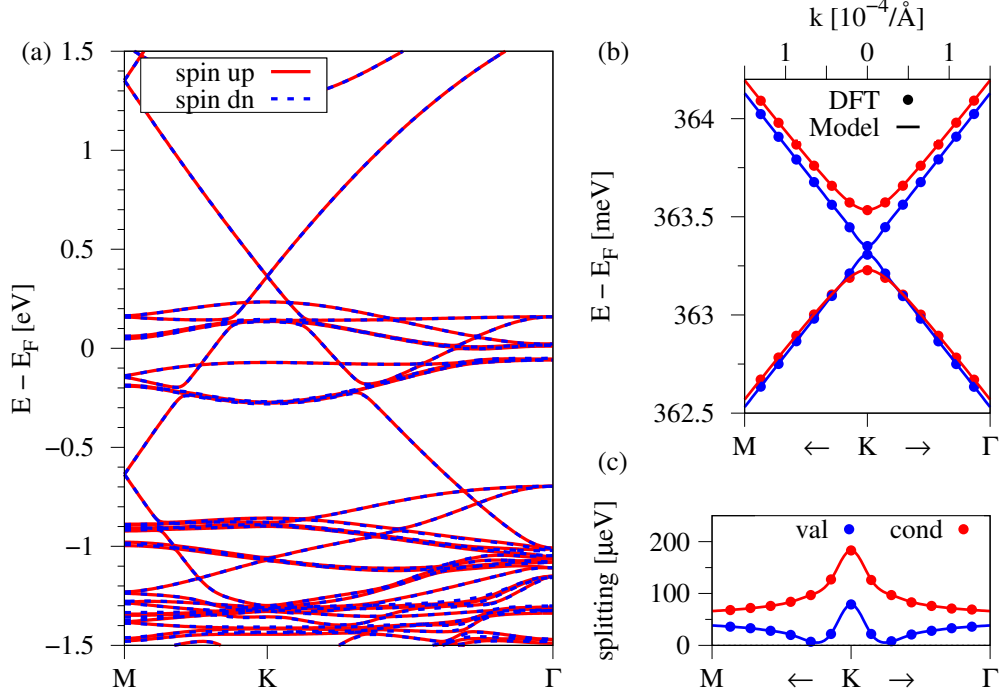


FIG. S28. (a) DFT-calculated band structure of the **graphene/CoPSe₃** heterostructure along the high-symmetry path M-K- Γ without SOC, when the CoPSe₃ is in the **antiferromagnetic Néel phase**. Red solid (blue dashed) lines correspond to spin up (spin down). (b) Zoom to the DFT-calculated (symbols) low energy Dirac bands near the K point with a fit to the model Hamiltonian (solid line). (c) The splitting of valence and conduction band.

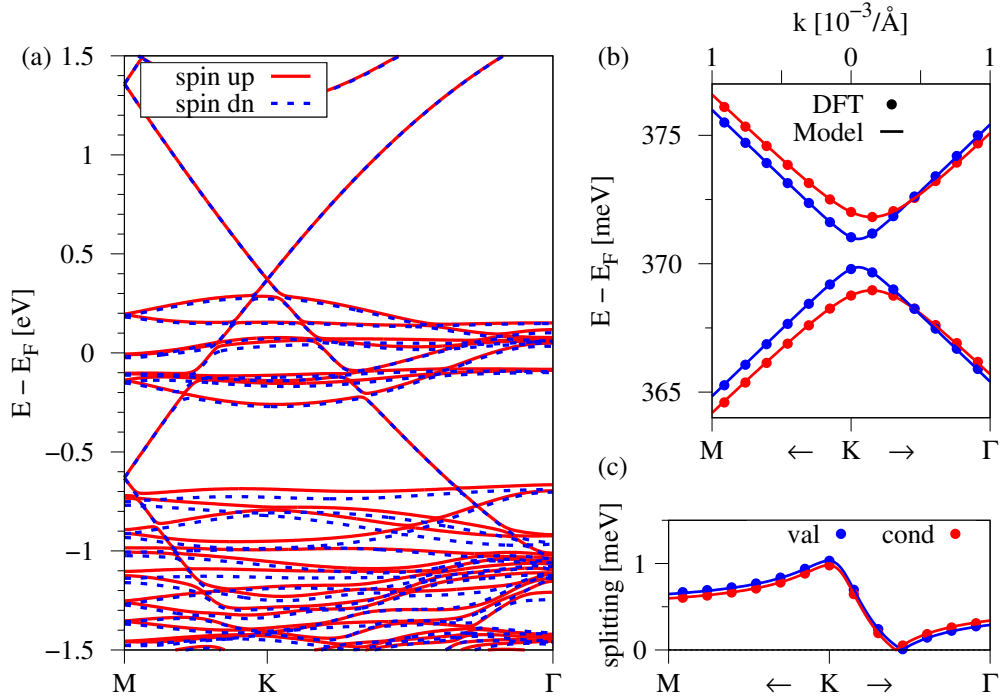


FIG. S29. (a) DFT-calculated band structure of the [graphene/CoPSe₃](#) heterostructure along the high-symmetry path M-K- Γ without SOC, when the CoPSe₃ is in the [antiferromagnetic zigzag phase](#). Red solid (blue dashed) lines correspond to spin up (spin down). (b) Zoom to the DFT-calculated (symbols) low energy Dirac bands near the K point with a fit to the model Hamiltonian (solid line). (c) The splitting of valence and conduction band.

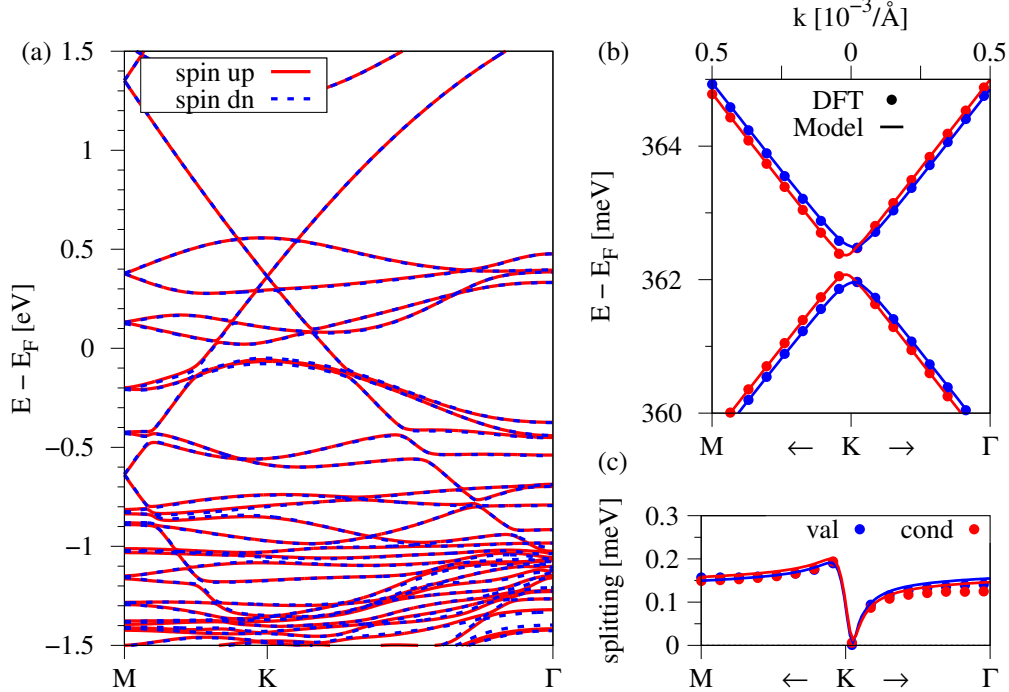


FIG. S30. (a) DFT-calculated band structure of the [graphene/CoPSe₃](#) heterostructure along the high-symmetry path M-K- Γ without SOC, when the CoPSe₃ is in the [antiferromagnetic stripy phase](#). Red solid (blue dashed) lines correspond to spin up (spin down). (b) Zoom to the DFT-calculated (symbols) low energy Dirac bands near the K point with a fit to the model Hamiltonian (solid line). (c) The splitting of valence and conduction band.

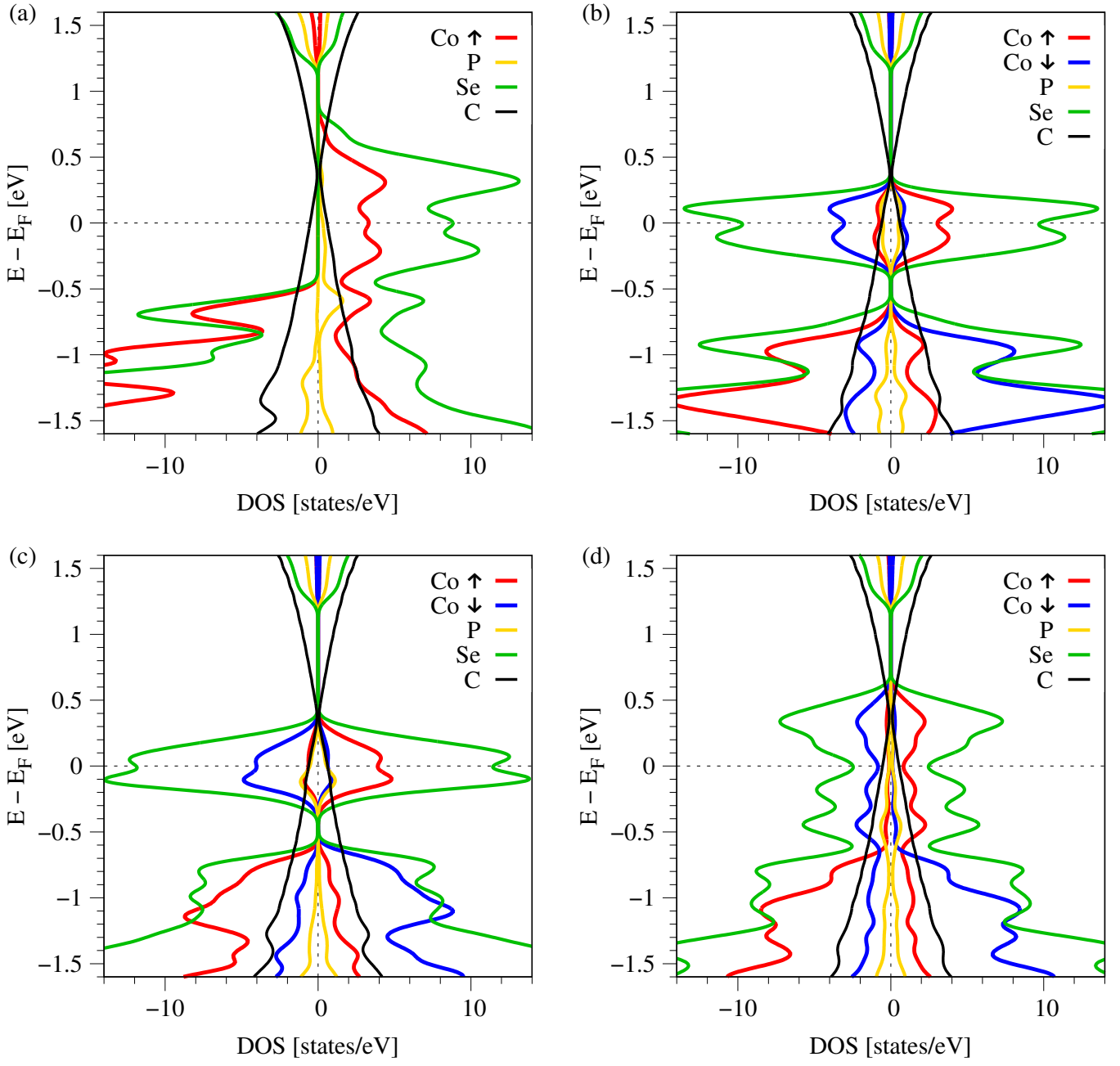


FIG. S31. Spin and atom resolved Density of States (DOS) for graphene on CoPSe_3 when CoPSe_3 is in the (a) ferromagnetic, (b) antiferromagnetic Néel, (c) antiferromagnetic zigzag, or (d) antiferromagnetic stripy phase.

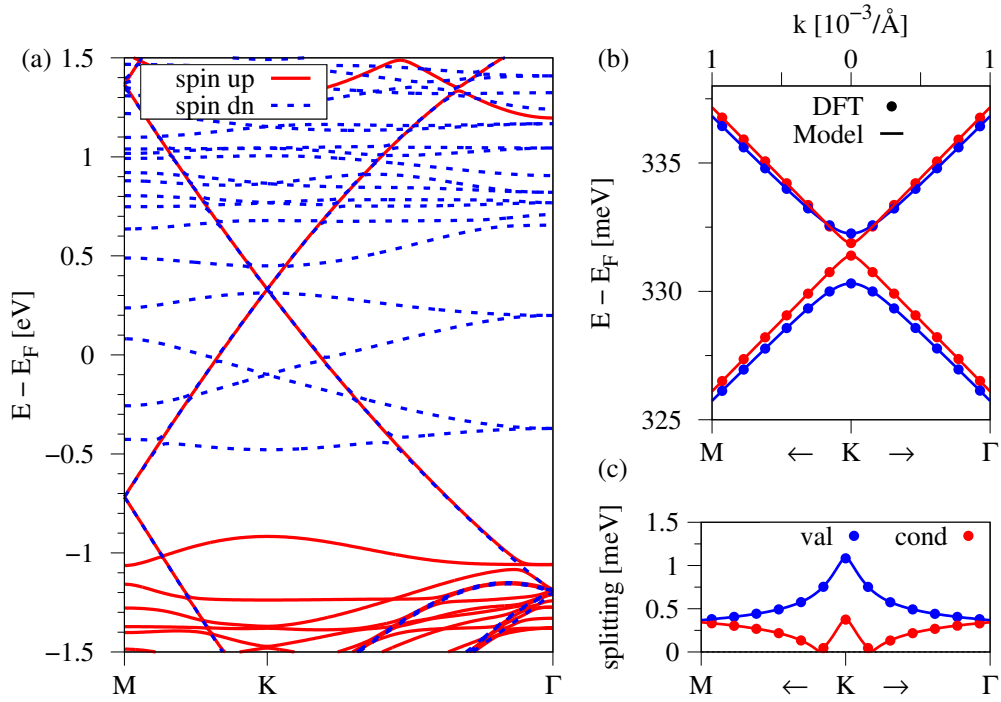


FIG. S32. (a) DFT-calculated band structure of the **graphene/FePS₃** heterostructure along the high-symmetry path M-K- Γ without SOC, when the FePS₃ is in the **ferromagnetic phase**. Red solid (blue dashed) lines correspond to spin up (spin down). (b) Zoom to the DFT-calculated (symbols) low energy Dirac bands near the K point with a fit to the model Hamiltonian (solid line). (c) The splitting of valence and conduction band.

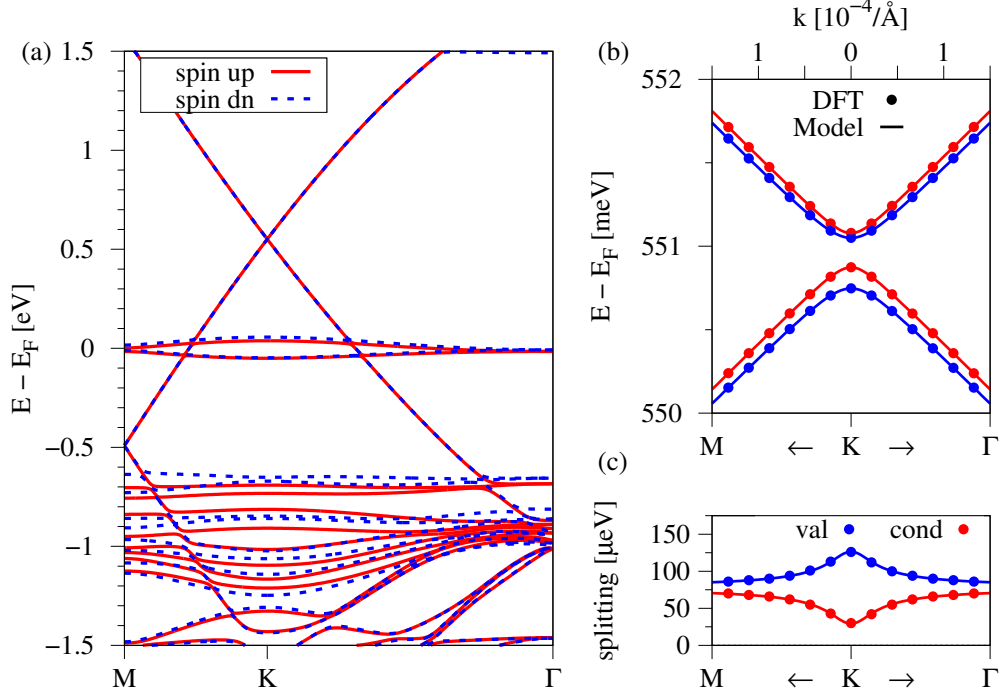


FIG. S33. (a) DFT-calculated band structure of the **graphene/FePS₃** heterostructure along the high-symmetry path M-K- Γ without SOC, when the FePS₃ is in the **antiferromagnetic Néel phase**. Red solid (blue dashed) lines correspond to spin up (spin down). (b) Zoom to the DFT-calculated (symbols) low energy Dirac bands near the K point with a fit to the model Hamiltonian (solid line). (c) The splitting of valence and conduction band.

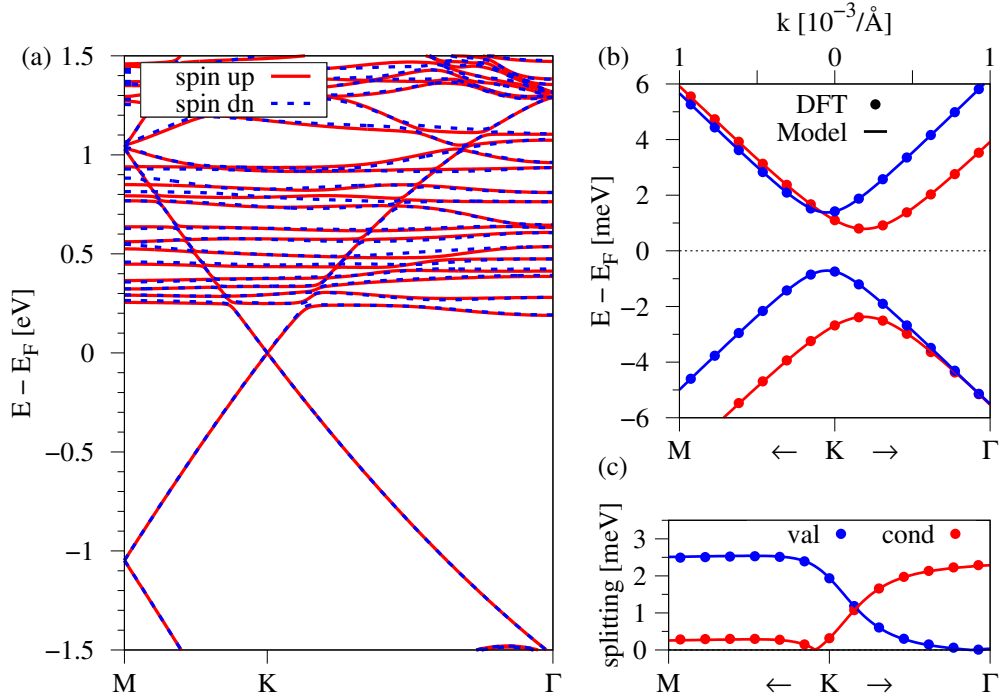


FIG. S34. (a) DFT-calculated band structure of the **graphene/FePS₃** heterostructure along the high-symmetry path M-K- Γ without SOC, when the FePS₃ is in the **antiferromagnetic zigzag phase**. Red solid (blue dashed) lines correspond to spin up (spin down). (b) Zoom to the DFT-calculated (symbols) low energy Dirac bands near the K point with a fit to the model Hamiltonian (solid line). (c) The splitting of valence and conduction band.

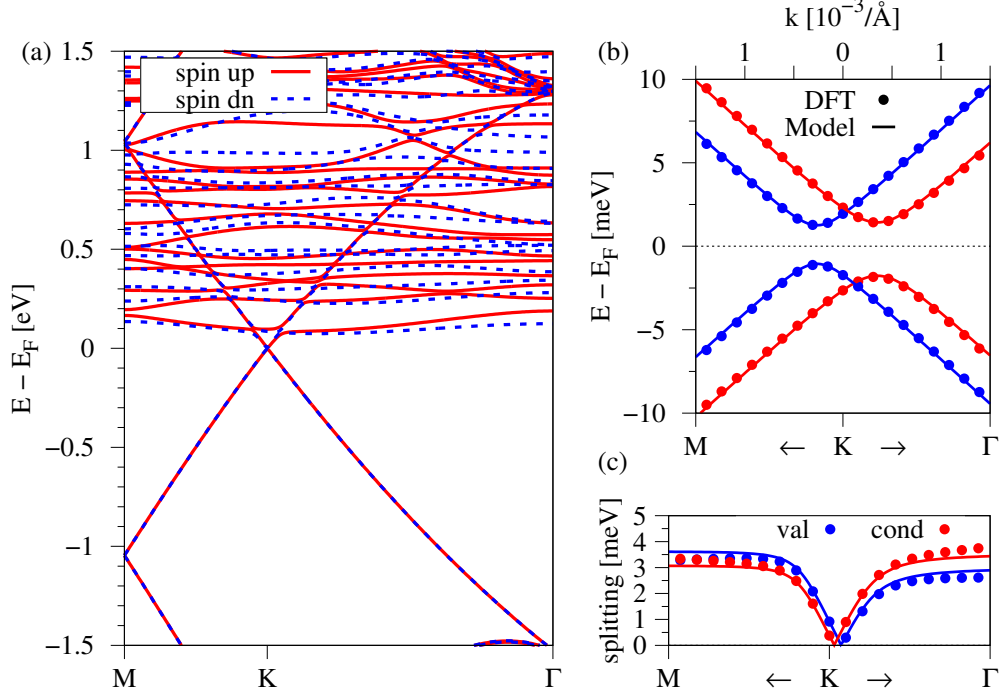


FIG. S35. (a) DFT-calculated band structure of the **graphene/FePS₃** heterostructure along the high-symmetry path M-K- Γ without SOC, when the FePS₃ is in the **antiferromagnetic stripy phase**. Red solid (blue dashed) lines correspond to spin up (spin down). (b) Zoom to the DFT-calculated (symbols) low energy Dirac bands near the K point with a fit to the model Hamiltonian (solid line). (c) The splitting of valence and conduction band.

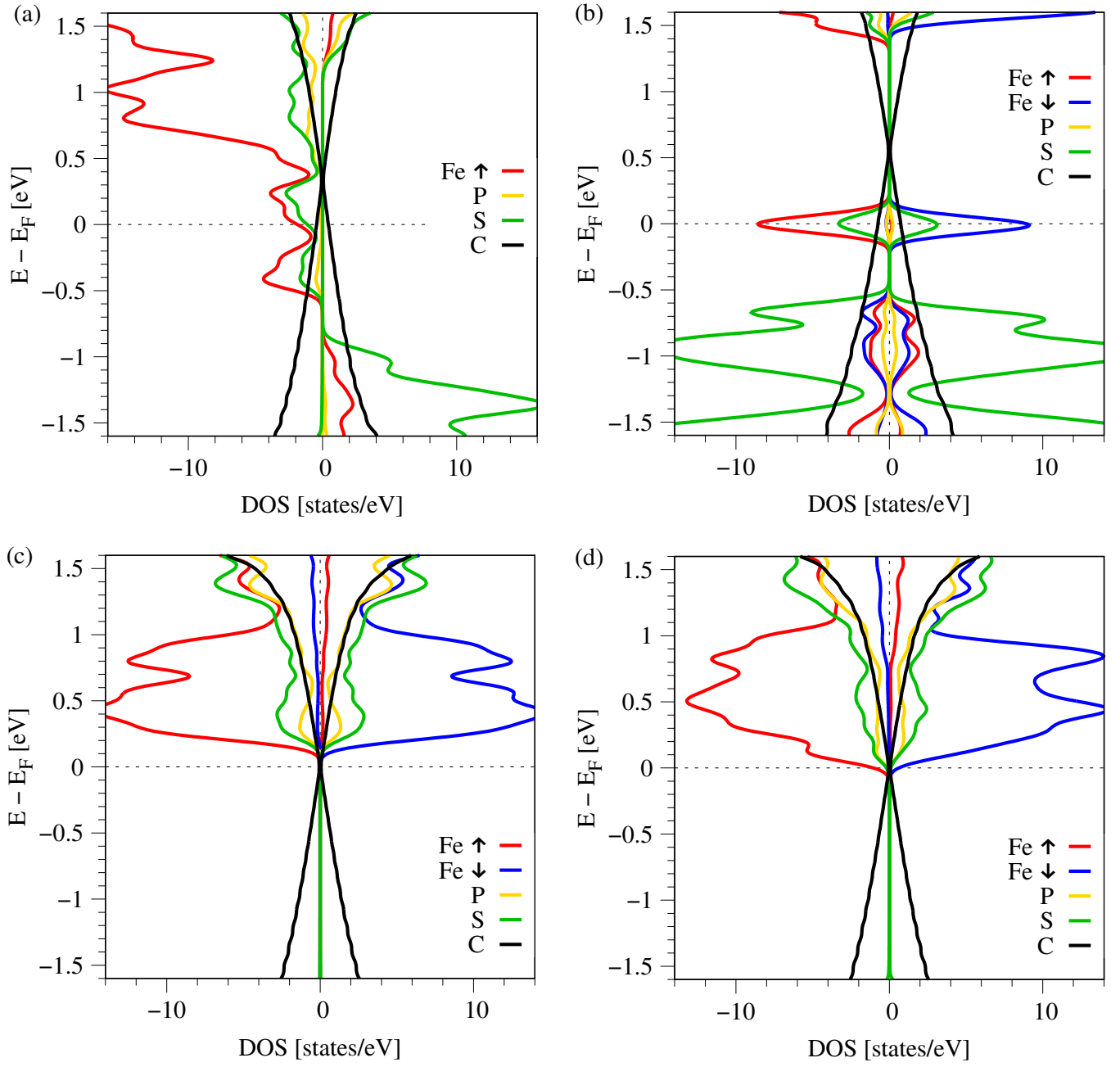


FIG. S36. Spin and atom resolved Density of States (DOS) for graphene on FePS_3 when FePS_3 is in the (a) ferromagnetic, (b) antiferromagnetic Néel, (c) antiferromagnetic zigzag, or (d) antiferromagnetic stripy phase.

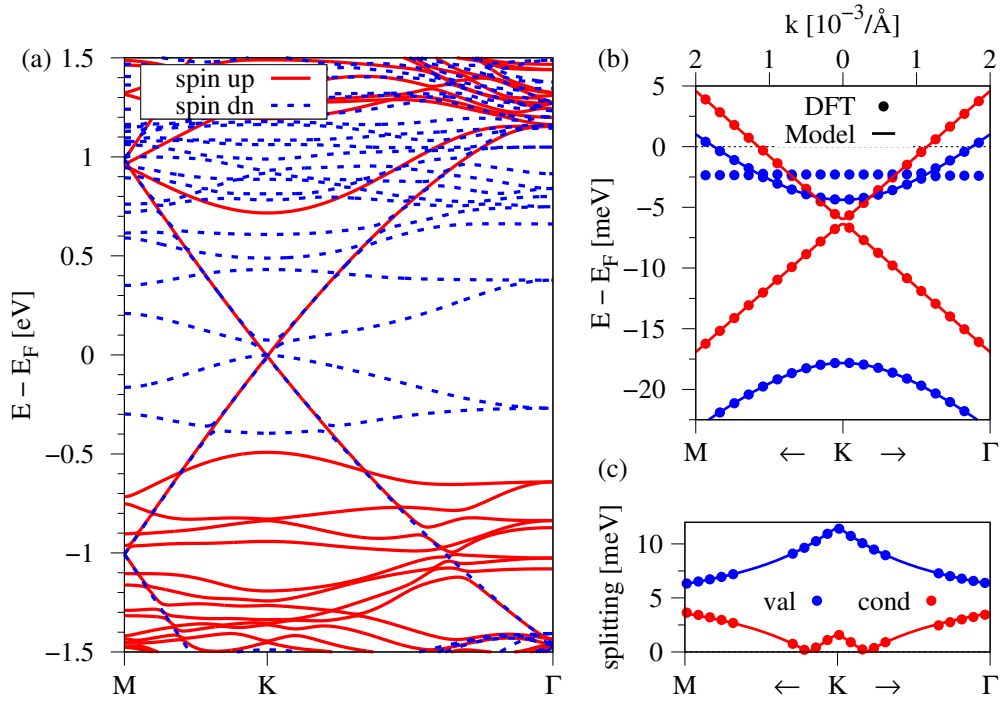


FIG. S37. (a) DFT-calculated band structure of the **graphene/FePSe₃** heterostructure along the high-symmetry path M-K- Γ without SOC, when the FePSe₃ is in the **ferromagnetic phase**. Red solid (blue dashed) lines correspond to spin up (spin down). (b) Zoom to the DFT-calculated (symbols) low energy Dirac bands near the K point with a fit to the model Hamiltonian (solid line). (c) The splitting of valence and conduction band.

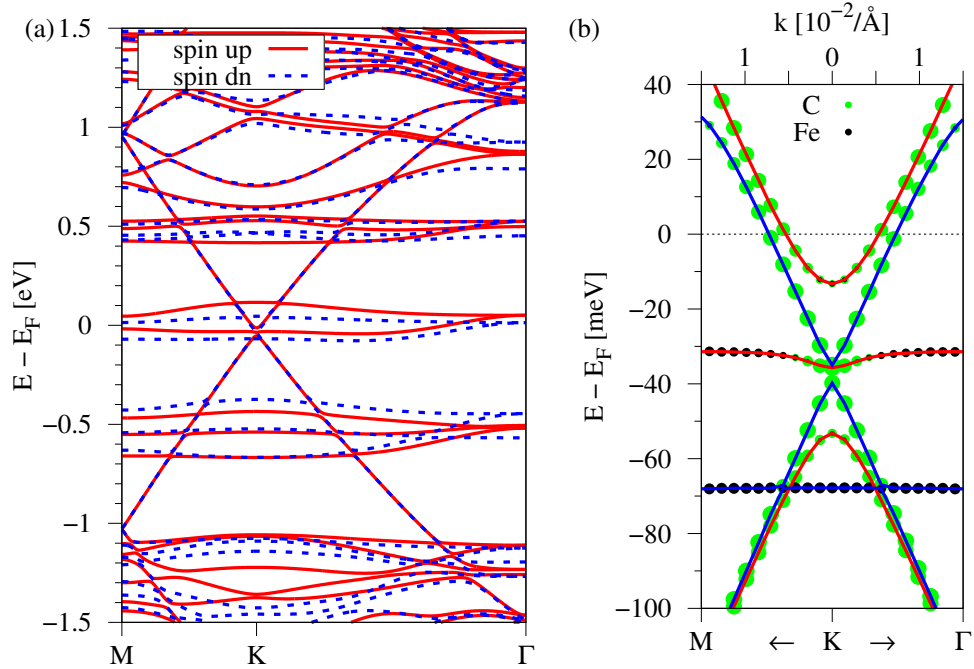


FIG. S38. (a) DFT-calculated band structure of the **graphene/FePSe₃** heterostructure along the high-symmetry path M-K- Γ without SOC, when the FePSe₃ is in the **antiferromagnetic Néel phase**. Red solid (blue dashed) lines correspond to spin up (spin down). (b) Zoom to the DFT-calculated (symbols) low energy Dirac bands near the K point with a fit to the model Hamiltonian (solid line). (c) The splitting of valence and conduction band.

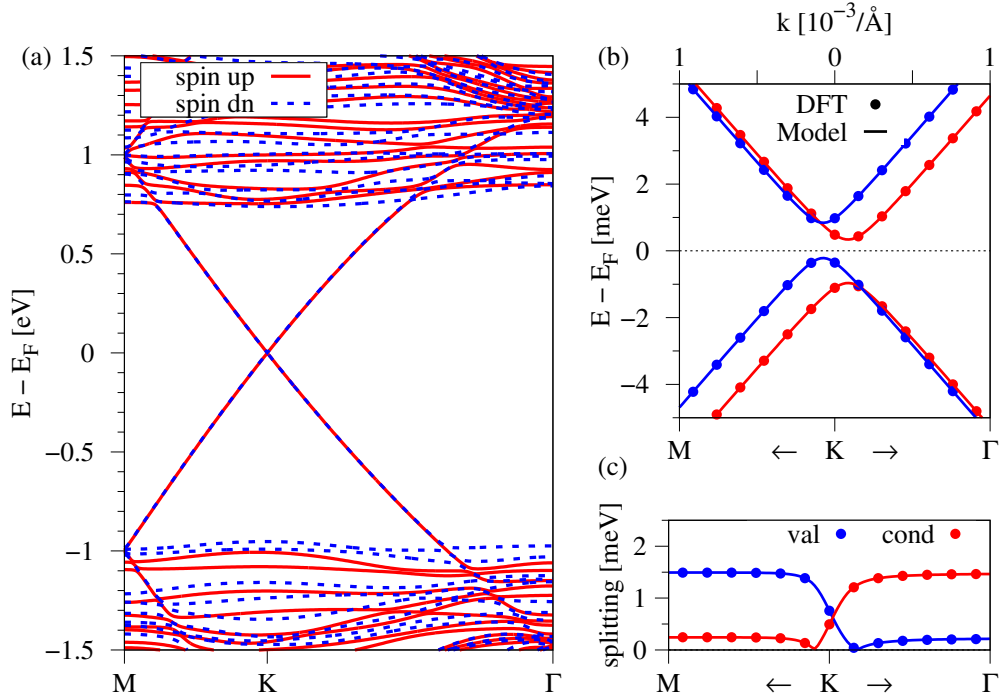


FIG. S39. (a) DFT-calculated band structure of the [graphene/FePSe₃](#) heterostructure along the high-symmetry path M-K- Γ without SOC, when the FePSe₃ is in the [antiferromagnetic zigzag phase](#). Red solid (blue dashed) lines correspond to spin up (spin down). (b) Zoom to the DFT-calculated (symbols) low energy Dirac bands near the K point with a fit to the model Hamiltonian (solid line). (c) The splitting of valence and conduction band.

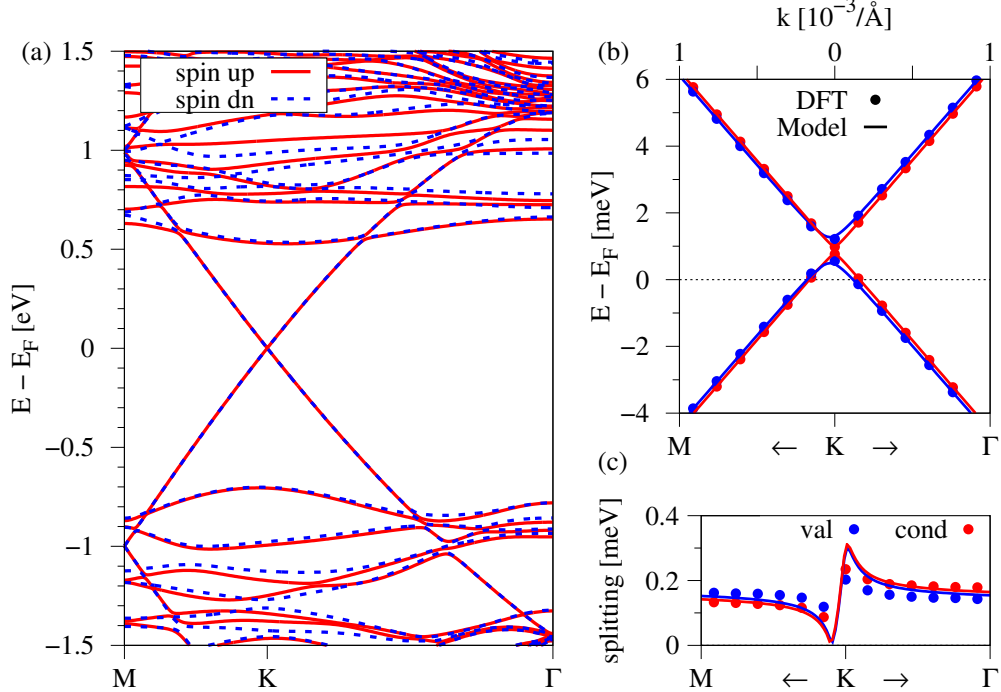


FIG. S40. (a) DFT-calculated band structure of the [graphene/FePSe₃](#) heterostructure along the high-symmetry path M-K- Γ without SOC, when the FePSe₃ is in the [antiferromagnetic stripy phase](#). Red solid (blue dashed) lines correspond to spin up (spin down). (b) Zoom to the DFT-calculated (symbols) low energy Dirac bands near the K point with a fit to the model Hamiltonian (solid line). (c) The splitting of valence and conduction band.

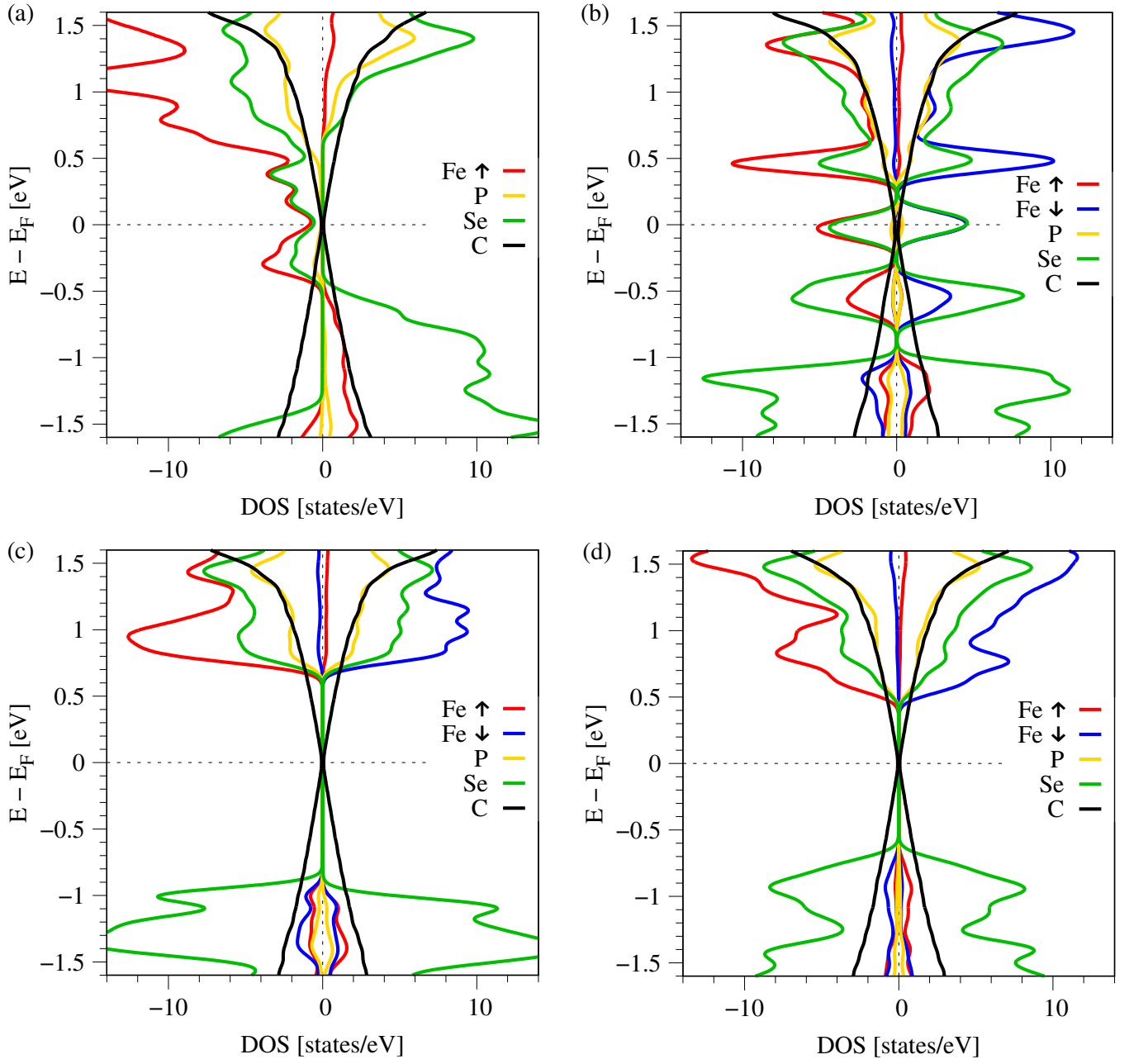


FIG. S41. Spin and atom resolved Density of States (DOS) for graphene on FePSe₃ when FePSe₃ is in the (a) ferromagnetic, (b) antiferromagnetic Néel, (c) antiferromagnetic zigzag phase, or (d) antiferromagnetic stripy phase.